Dissertation

submitted to the

Combined Faculties of the Natural Sciences and Mathematics

of the Ruperto-Carola-University of Heidelberg, Germany

for the degree of

Doctor of Natural Sciences

Put forward by

Ugo Tricoli

Born in: Modena

Oral examination: 24.7.2015

Electromagnetic scattering with the GDT-matrix method:

an application to irregular ice particles in cirrus

Sharp Calm Pink, W. Kandinsky 1924

Referees:
Prof. Dr. K. Pfeilsticker

Prof. Dr. C. Dullemond

Abstract:

Electromagnetic scattering with the GDT-matrix method: an application to irregular ice particles in cirrus

The study describes a new method to calculate electromagnetic scattering from small, arbitrary shaped particles. It is called the Green's dyadic technique for the transition operator (briefly the GDT-matrix). First, the method is introduced from the general theory of scattering (transition operator and Dyson equation) and then it is compared with existing electromagnetic scattering models. Second, the model is used to characterize small ice particles and to interpret single-particle scattering measurements made with the Small Ice Detector instrument (SID). In particular, the study is focused on small irregular particles with fractal shapes. We apply the Gaussian random sphere model in order to give an estimation of the particle roughness. The direct comparison of the forward scattered intensity as measured by SID and simulated by the GDT-matrix model leads to a retrieval of the size and shape of the scatterers. Third, the single particle results are statistically averaged to calculate many-particle optical properties in order to evaluate radiances through the radiative transfer Monte Carlo model McArtim. Further, the simulated radiances in near-infrared (NIR) are compared with measurements made during the NASA-ATTREX project on board the research unmanned aircraft Global Hawk. These comparisons lead to a remote retrieval of the thermodynamic phase of the constituent cloud particles and provide insights on the surface of the scatterers, i.e. rough or smooth.

Simulation elektromagnetischer Streuung mit Hilfe der GDT-Matrix-Methode: Eine Anwendung auf unregelmäßig geformte Eispartikel in Zirren

Die Arbeit beschreibt eine neue Methode, um die Streuung elektromagnetischer Strahlung an kleinen, unregelmäßig geformten Partikeln zu berechnen. Die Methode lässt sich am besten als "Green's dyadic" Technik nach dem Operator des Zustandsübergangs (die sog. GDT-Matrix) bezeichnen. Zuerst wird die Methode aus der allgemeinen Streutheorie hergeleitet (Operator des Zustandsübergangs und Dyson-Gleichung) und dann werden die Ergebnisse mit existierenden Modellen verglichen. Anschließend wird die Methode genutzt, um die Lichtstreuung kleiner Eispartikel zu charakterisieren und um Messungen des "Small Ice Detector"-Instruments (SID) zu interpretieren. Im Speziellen konzentriert sich die Arbeit auf die Lichtstreuung an kleinen, unregelmäßigen Partikeln mit fraktalen Formen. Um die Oberflächenrauhigkeit zu simulieren, wird ein Gaussian-random-sphere Modell verwendet. Der Vergleich der Vorwärtsstreuung aus den SID-Messungen mit Simulationen aus dem GDT-Matrix-Modell erlaubt Rückschlüsse auf die Größe und Form der Streuer. Im nächsten Schritt werden die Ergebnisse für einzelne Partikel statistisch gemittelt, um die optischen Eigenschaften eines Teilchenensembles zu berechnen. Diese werden dazu genutzt, Radianzen im nahen infraroten Spektralbereich mit dem Strahlungstransportmodell McArtim zu berechnen. Vergleiche mit während des NASA-ATTREX-Projekts an Bord einer "Global Hawk"-Drohne durchgeführten Messungen eröffnen die Möglichkeit, die thermodynamische Phase der Wolkenteilchen sowie deren Rauhigkeit mit Fernerkundungsinstrumenten zu bestimmen.

Contents

To my family

Chapter 1

Introduction

1.1 Motivation

The radiative forcing of clouds composed of ice crystals, cirrus, is among the least understood process in the Earth atmosphere. In particular, it is not clear whether cirrus clouds warm up or cool down the Earth surface [1]. Cirrus clouds can cool the atmosphere close to the surface by reflecting incoming solar radiation back to space (albedo effect), or can have a warming effect by absorbing outgoing infrared radiation emitted by the Earth (greenhouse effect). The net radiative effect is defined as the difference between the electromagnetic energy flux (both short and long wave) in presence of the cirrus and the corresponding one in absence of the cloud so, for clear sky. The net radiative forcing depends on the size distribution and optical properties of the cloud particles [2]. It is generally accepted that optically thick (optical thickness greater than 1) cirrus clouds in the upper troposphere generally produce a negative forcing due to reflection of incoming radiation, while optically thin (optical thickness lower than 0.3) cirrus clouds located at the same height bring a positive forcing since they absorb outgoing terrestrial radiation in the mid-infrared. The cirrus have also another effect of dehydration of the stratosphere due to fast ice particle nucleation at high altitude. The International Panel for Climate Change (IPCC) produced in 2007 the table that we adapt in Figure 1.1 in which it is stressed that the level of scientific understanding (LOSU) is very low for clouds in general [3].

The radiative effect of clouds is usually parametrized through microphysical properties as the effective radius of the size distribution. This can be linked directly to the optical thickness τ and the ice water content (IWC in g/cm^3). For instance following Baran [1], for big ice crystals it is possible to write the effective radius as $D_e = 3IWP/\rho\tau$ where the density of solid ice is $\rho = 0.92$ gcm^-3. The column integrated IWC is called
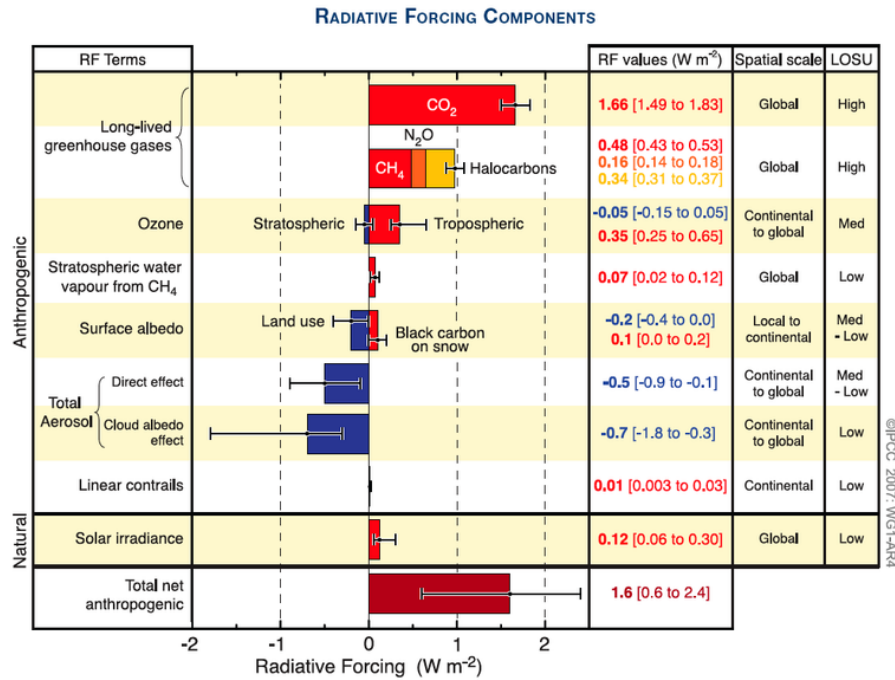
FIGURE 1.1: IPCC radiative forcing components. Adapted from [3].

the ice water path (IWP in g/cm^2) and the column integrated volume extinction is called the optical thickness. This highlights the importance of the particle dimension. Indeed, having two clouds with the same IWP, the one with the smaller effective radius has a greater optical thickness resulting in more reflected radiation. It is important to note here that the microphysical properties (as the radius) are inferred from optical measurements of the radiance (electromagnetic radiation intensity per solid angle) that are used as input for a retrieval algorithm. The corresponding modeled radiance is calculated based on optical properties of the particles averaged over the size distribution and is adjusted in the retrieval scheme in order to fit the measured radiance. Thus, once the optical properties are known, the radius can be retrieved finding the best effective radius of the size distribution that leads to the best fit of the measured radiance [1]. It is then evident that an inaccurate calculation of the optical properties (most notably the asymmetry parameter) can result in very different retrieved effective radius and consequently to a wrong estimation of the IWC that is then used in global circulation models to quantify the radiative forcing of the cloud. Thus, a detailed study of cirrus particle optical properties is required in order to retrieve the microphysical properties that in the end drive the radiative forcing of the whole cloud [4].

1.2 Outline

Different levels of investigation are necessary in order to quantify the effect of cirrus corresponding to the spatial scale of the observations. The smaller scale focus on the single-particle optical properties (taking into account irregularities and roughness), the intermediate considers the importance of statistical distributions of particles and, the large scale considers the effect of the cloud as a whole through its radiative forcing.

The thesis is dedicated to the theoretical study of the optical properties of small, irregular and rough particles through a new model here developed and called the Green's Dyadic technique for the Transition matrix (GDT-matrix). The non-spherical ice particle characterization is obtained through comparisons of the GDT-matrix results with the single-particle SID measurements (Small Ice Detector).

In chapter 2 the problems connected to the description of ice particles in cirrus clouds are introduced. Then, in chapter 3 the theory of single and multiple scattering is described. Chapter 4 is dedicated to the description of the models used. In particular, a new model for single particle scattering is developed and called the GDT-matrix which is capable of describing small scale surface irregularities (first section of chapter 4). The Mie model is used for spherical scatterers and also to do the statistical average over size of the optical properties. Considering multiple scattering, the radiative transfer equation is numerically solved with the code called McArtim (Monte Carlo Atmospheric Radiative Transfer Inversion Model). In chapter 5 the SID instrument is described and its forward scattering measurements for irregular ice particles are presented. Then, the mini-DOAS (differential optical absorption spectroscopy) instrument is characterized and examples of the radiance measurements from the research aircraft Global Hawk (GH) within the NASA-ATTREX project are shown. In chapter 6 the GDT-matrix predictions for small irregular particles are compared to the SID measurements explaining the interference speckle patterns in term of the Gaussian random sphere parameterization (first section of chapter 6). At the end, the effect of cirrus on the near-infrared spectrum is also simulated with McArtim and compared with mini-DOAS passive radiance measurements (second section of chapter 6). Hence, it is shown how this measurement is sensitive to single-particle properties and thus to surface irregularities. Then, chapter 7 concludes the study.

Chapter 2

Background

2.1 The solar radiation and the atmosphere

2.1.1 Thermal structure of the atmosphere

The physical system in which we are interested is the Earth atmosphere and especially its interaction with the solar radiation. To define the regions associated with absorption and scattering of sunlight it is convenient to introduce the vertical temperature profile for the standard atmosphere see figure 2.1. Traditionally, the vertical profile is divided into four separate layers i.e. the troposphere, stratosphere, mesosphere, and thermosphere. Every layer ends with a transition region as for example the tropopause.
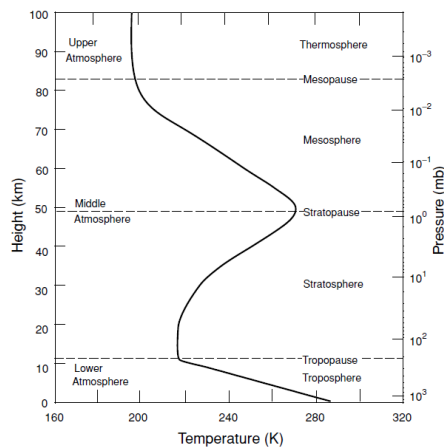

FIGURE 2.1: Temperature profile of the standard Earth atmosphere with respect to altitude. Adapted from [5].

In the troposphere the temperature decreases with respect to height from 288 K close to the surface to about 220 K at a rate of 6.5 K/km. The temperature structure there is a

consequence of the radiative balance and the convective transport of energy [5]. This is the part of the atmosphere that hosts clouds and thus water vapour. The stratosphere starts with an isothermal layer from the tropopause until about 20 km, above which the temperature gradient changes sign with a rise up to 270 K around the stratopause. The state of the stratosphere is mainly determined by the absorption of solar fluxes by ozone and emission of infrared fluxes by carbon dioxide i.e. by a delicate radiative balance. In the mesosphere the temperature decreases again as in the troposphere. Above 85 km until several hundred kilometers, the temperature varies from 500 K to 2000 K depending on the level of solar activity, consequently this atmospheric layer is called thermosphere. In addition, the outermost region of the atmosphere is called the exosphere while the lowest part below 1 km is called the planetary boundary layer.

2.1.2 Chemical composition and absorption

Mainly two groups of gases form the Earth atmosphere: one with nearly permanent concentrations and another with variable concentrations [5]. Figure 2.2 shows the chemical formulas and volume ratios for the concentrations. Nitrogen, oxygen and argon fill 99.96% of the atmosphere volume. Notably, the permanent gases have constant volume ratios up to an altitude of 60 km. It must be noted that carbon dioxide concentration has been increasing by about 0.4% per year due to fossil fuel combustion. An analogue behaviour is found for methane with an increase of $1-2\%$ per year due to larger biogenic emissions linked to a rising human population.

The Composition of the Atmosphere[a]

Permanent constituents		Variable constituents	
Constituent	% by volume	Constituent	% by volume
Nitrogen (N_2)	78.084	Water vapor (H_2O)	0–0.04
Oxygen (O_2)	20.948	Ozone (O_3)	$0-12 \times 10^{-4}$
Argon (Ar)	0.934	Sulfur dioxide (SO_2)[b]	0.001×10^{-4}
Carbon dioxide (CO_2)	0.036	Nitrogen dioxide (NO_2)[b]	0.001×10^{-4}
Neon (Ne)	18.18×10^{-4}	Ammonia (NH_3)[b]	0.004×10^{-4}
Helium (He)	5.24×10^{-4}	Nitric oxide (NO)[b]	0.0005×10^{-4}
Krypton (Kr)	1.14×10^{-4}	Hydrogen sulfide (H_2S)[b]	0.00005×10^{-4}
Xenon (Xe)	0.089×10^{-4}	Nitric acid vapor (HNO_3)	Trace
Hydrogen (H_2)	0.5×10^{-4}	Chlorofluorocarbons	Trace
Methane (CH_4)	1.7×10^{-4}	($CFCl_3$, CF_2Cl_2	
Nitrous oxide (N_2O)[b]	0.3×10^{-4}	CH_3CCl_3, CCl_4, etc.)	
Carbon monoxide (CO)[b]	0.08×10^{-4}		

[a]After the U.S. Standard Atmosphere (1976) with modifications.
[b]Concentration near the earth's surface.

FIGURE 2.2: Standard atmosphere components. Adapted from [5].

Variable gases are less present but their effect on radiation budget is relevant. Water vapour is the principal dynamic element that is strongly interacting with the solar radiation. Its concentration in the troposphere is determined by the local hydrological cycle through evaporation, condensation, precipitation and large-scale transport. In

addition, specific humidity decreases almost exponentially with pressure. Hence, the stratospheric water vapour is small being also influenced by dehydration due to cirrus formation as outflow from cumulus. The ozone concentration also varies very much with space and time but it is mainly present between 15-30 km that is called the ozone layer. Most importantly, ozone is continually created and destroyed by photochemical processes caused by ultraviolet solar radiation [5] (a process that is also fundamental for life). Considering the other variable species, NO_x are among the most important being emitted by combustion processes at the surface and by high-flying aircraft in the upper troposphere. Chlorofluorocarbons produced by industries are also important concerning the destruction of the ozone layer due to chlorine and bromine. Then, sulfuric dioxide which is reaching the stratosphere via volcanic eruptions, is believed to be the primary precursor of stratospheric aerosols. It is also important regarding the formation of acid rain when it is emitted near to the surface. Figure 2.3a displays vertical profiles of the gases mentioned above.

(A) (B)
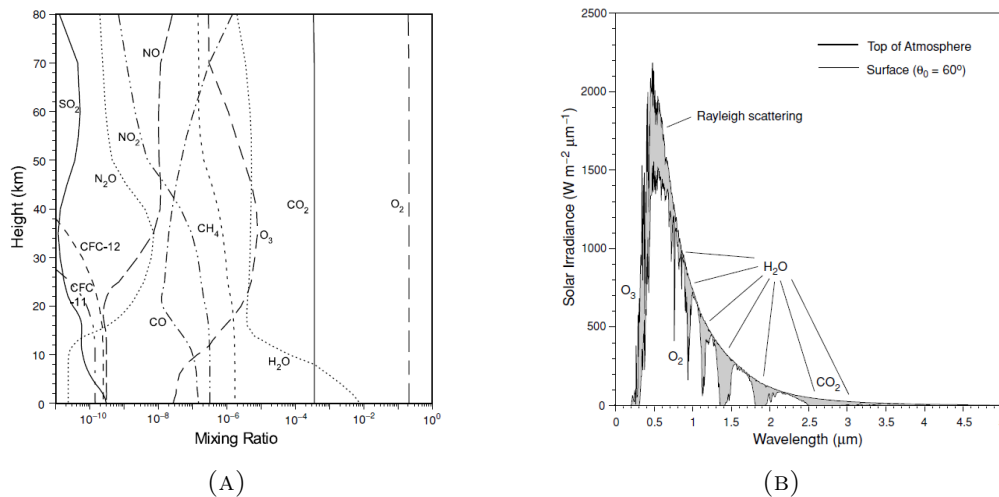
FIGURE 2.3: Gases profiles and their absorption. (A) gases profiles as mixing ratio, (B) absorption of the solar irradiance due to molecular gases as ozone, oxygen, water vapour and carbon dioxide. Adapted from [5].

The understanding of the atmospheric absorption form the various molecules requires a detailed understanding of the molecular structure. Here we just consider the main process behind absorption of light by atmospheric molecular gases. This requires the first quantization and the quantization of the Maxwell's equations defining photons. The absorption of photons is mainly linked to a transition of the molecule to a higher energy electronic state. If we consider a diatomic molecule, the electronic energy is related to the vibrational energy because both are related to the elastic valence bonds that bind the atoms together thus forming the molecule [5]. The force between the atoms depends on the nuclei distance and the electronic configuration of the atoms. The potential regulating the force between two atoms is the Lennard-Jones potential (see

Figure 2.4). At large distances the two atoms experience no significant force. Decreasing their distance they start to exert an attractive force that at the end is responsible of the ground state of the molecule in the minimum of the potential well. At smaller distance the atoms start to repel each other.
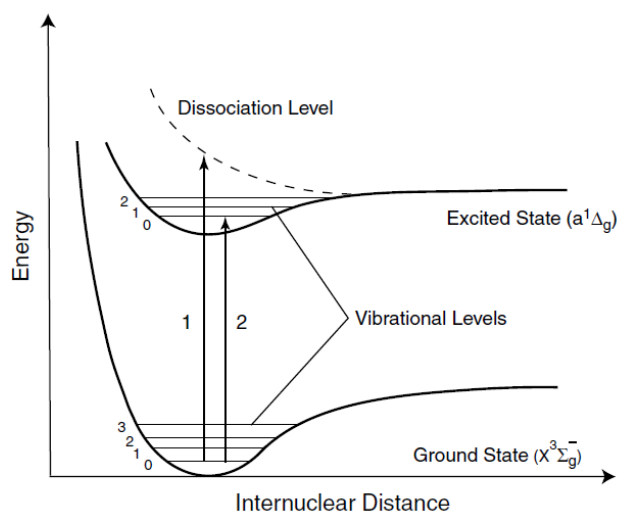

FIGURE 2.4: Lennard-Jones potential for two electronic states of a diatomic molecule.
The horizontal lines in the potential wells represent vibrational energy levels.
Adapted from [5].

When a high-energy photon is absorbed, the electron configuration changes to an excited state with a different potential energy as depicted in the upper part of Figure 2.4. The energy of the transition is given by the difference of the two minima of the potential wells. If the excited state is unstable, the molecule may decompose into its constituent atoms. At atmospheric temperatures, most of the molecules are in the ground vibrational state [5]. Two possible transitions are represented in Figure 2.4. Transition 1 brings the molecule from the ground state to a state that is not quantized thus causing dissociation linked with a continuum of wavelengths near the dissociation energy. The corresponding spectrum is made by a smooth continuum at short wavelengths above the dissociation limit. The quantized transition 2 requires absorption of a specific photon that leads the molecule to a particular vibrational level of the excited state. The associated spectrum is made of discrete wavelengths. Many transitions linked to diatomic molecules are a combination of electronic and vibrational transitions. The manifestation of absorption is shown in Figure 2.3b where a comparison is done between a spectrum recorded at the top of the atmosphere (no absorption from gases) and the same as recorded from the ground with a 60° elevation angle from the surface. In particular, in the Results chapter we show radiance simulations characterized by the absorption bands of oxygen, carbon dioxide and water vapour in the near-infrared part of the spectrum. To conclude, we mention that absorption is represented by the absorption cross section σ_{abs} in units of

cm^2 and for many particle, it is represented by the absorption coefficient $\beta_{abs} = \sigma \cdot N_0$ in units of cm^{-1} with N_0 the number density. In addition, the absorption cross sections of the gases are temperature and pressure dependent so an accurate measurement of T and P is required.

2.1.3   Particles and scattering

In addition to gases, the atmosphere contains aerosol particles with dimension $10^{-3} - 20\mu m$ of natural and human activity origin. Natural aerosols are for example volcanic dust, smoke from forest fires, particles from sea spray, dust transported by wind, and small particles produced by the chemical reactions of natural gases like sulfuric acid [5]. Aerosols produced by human activities are mainly related to combustion. The aerosol largest concentration usually occurs in urban and desert areas leaving a visibility of 20-50 km. Importantly, aerosols concentration decrease exponentially with height in the troposphere. Aerosols are also involved in the complex process of ice nuclei formation.

The remaining atmospheric component are clouds which are globally spread and they cover more than 50% of the sky. There are many different types of clouds with different microphysical composition. Typically cumulus generate precipitations. In the following we will concentrate on cirrus especially in the tropics where they are regularly present and strongly influence the radiative balance.

All the particles in the atmosphere absorb light as a continuum because they can be described by macroscopic bulk optical properties as the refractive index (thus differing substantially from molecules). However, their influence on the atmosphere is relevant since they can also scatter light unisotropically.

The scattering nature of the atmospheric particles interacting with solar radiation depends mainly on their shape and dimension. For spherical scatterers the problem can be treated analytically with Mie theory (see chapter 4). For molecules with effective radius around $10^{-4}\mu m$ the differential scattering cross section is the well-known Rayleigh cross section. Then, aerosols have a radius of around $1\mu m$ and can be treated with the statistical Mie theory considering an average over size of the differential scattering cross section. Increasing further the size, the last atmospheric spherical particles that can be treated accurately with the Mie theory are water droplets with a typical radius of around $10\mu m$. The differential scattering cross section of these three scatterers are compared in Figure 2.5.

Inside clouds, and in particular in high cirrus, the principal components are ice crystals. When they are large, they usually exhibit hexagonal symmetry like plates or columns
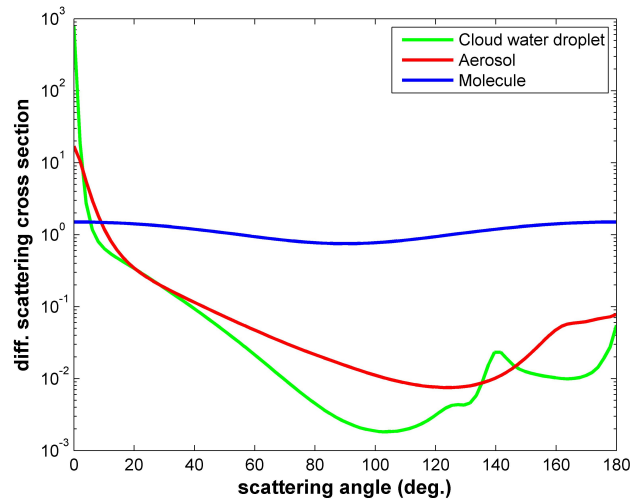
FIGURE 2.5: Comparison of the differential scattering cross section in NIR ($\lambda = 1.3\mu m$) averaged over a log normal size distribution for spherical scatterers with median radius equal to $10^{-4}\mu m$ (molecule), $1\mu m$ (aerosol) and $10\mu m$ (cloud water droplet).

causing halos. However, the majority of ice particles tend to have a very irregular shape and so their geometry should be treated carefully and especially their surface. In the next chapters we will consider in details how to treat highly non-spherical scatterers like small ice crystals [6].

2.1.4 The Tropical Tropopause Layer

The Tropical Tropopause Layer, shortly TTL (13-18 km altitude [7]), is the least understood part of the atmosphere despite its relevance being the entry point for the stratosphere [8]. In particular, in the tropics the altitude of the tropopause is lifted up to around 15 km thus opening a gate to the stratosphere for chemical substances through strong convective transport. The two major sources of uncertainties are the water vapour amount (connected to the presence of cirrus) and the chemical composition of the TTL. The temperature distribution is also unknown due to the high vertical variability connected to convective events and gravity waves. Very strong convective events can bring ozone depleting substances (as bromine) to the stratosphere through the TTL. The same happens for water vapour that is taken very fast from regions near to the surface to the TTL. This can lead to large cold and supersaturated zones respect to the water vapour, thus making possible the very fast nucleation of ice particles which remain small in contrast to slow cooling that produces big crystals. The nucleation of ice particles is responsible for dehydration of the TTL and is called freeze drying. The importance of convection is represented in Figure 2.6. In addition, all these physical processes are strongly coupled. Indeed, convection affects transport of water vapour

and chemical substances and affects also the tropical pressure waves. These waves interact with cirrus formation and also help large scale ascent. The cirrus, with their constant presence in the tropics in time and space, influence directly the energy budget of the Earth through interaction with solar radiation (radiative forcing, thin cirrus net warming is larger than the one caused by greenhouse gas increase). In addition, cirrus contribute significantly to the dehydration of the TTL by freeze drying that also affect the whole stratosphere through the Brewer-Dobson circulation. In the end, the TTL also controls the rate of stratospheric ozone depletion because it is the entrance to the stratosphere. Due to the lack of knowledge of the TTL more observations are required to fill the gap between mesoscale measurements performed with aircrafts (scale of the order of few hundreds kilometers) and macroscale observations available from satellites (several thousands kilometers). In addition, satellite measurements do not possess the capacity to resolve very variable structures as the ones encountered in the TTL.
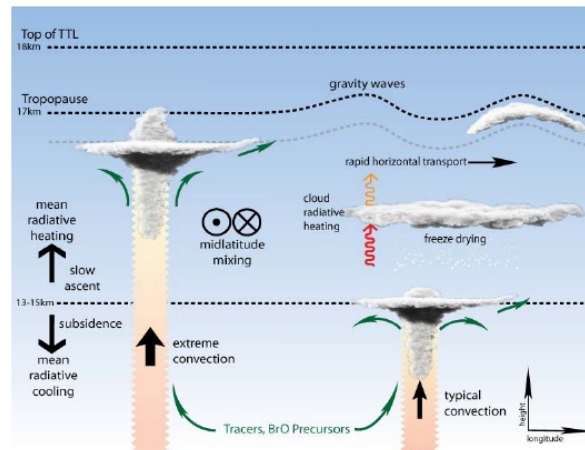
FIGURE 2.6: Processes occuring in the TTL. Adapted from [8].

2.2 Cirrus

Cirrus are clouds occurring at altitudes greater than 6 km (see Figure 2.7) and typically at temperatures lower than 230 K, thus the constituent particles are in an ice phase [1]. Normally, it is not easy to distinguish at naked eye a cirrus from the background blue sky because the number density of particles tend to be very small (0.01 particles per cubic centimeter) and so the number of scattering events of natural solar light. In Figure 2.8 this property is directly shown through two pictures of the same cirrus taken with two different angular orientations, one pointing to the zenith (the cloud is nearly invisible in part b and d) and one with a greater zenith angle in a way to increase the light-path inside the cirrus and so the scattering events (a and c).

FIGURE 2.7: Cloud Physics Lidar (CPL) backscattered intensity at 532 nm showing the location of the cloud as a function of the altitude, vertical axis, and time, horizontal axis. Adapted from [9].
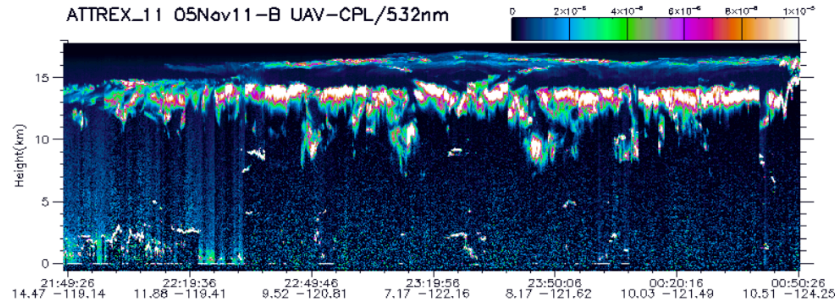
Nevertheless, the radiative effect of this kind of clouds is important both for the radiation budget and for the hydrological cycle. This is even more relevant considering that from satellite measurements appears that cirrus covers about 30% of the mid-latitudes and in the tropical zones the abundance is even higher between 60% and 80% at any time [1]. With this large spatial and temporal distributions cirrus have a significant impact on the atmosphere but their role is not well understood. As a consequence of this lack of knowledge, the results of satellite measurements present many differences (especially in the tropics) when compared to the calculated reflected short-wave flux at the top-of-atmosphere TOA in the context of climate general circulation models [1] (see Figure 2.9).

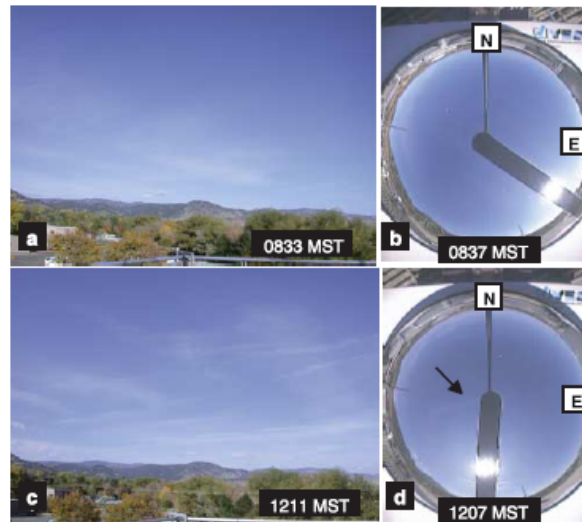FIGURE 2.8: Photographs showing the view to the northwest from the NOAA David Skaggs Research Center (DSRC) located on the western edge of Boulder, Colorado. The cirrus formed from aircraft contrails is clearly seen at low elevation angles, (a) and (c), but is largely invisible in all-sky photographs (b) and (d). The arrow in (d) indicates a tenuous contrail passing through the zenith. Adapted from [2].
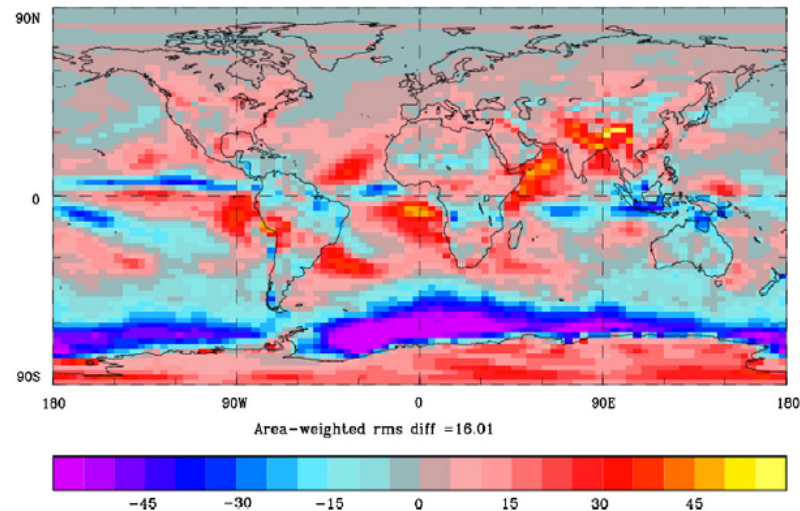
FIGURE 2.9: A ten-year mean difference plot, between a climate model and space-based measurements, of the TOA reflected short-wave flux, for the winter period (December, January, and February). In units of Wm^{-2}. Adapted from [1].

Indeed, the radiative effect of cirrus is complex due to its dependence on many parameters such as the altitude of the cloud, its optical thickness, its size and shape, the ice crystal shapes and distribution in size, and the total amount of ice mass (the ice water content, IWC). Generally speaking, the short-wave radiative effect tend to be negative (cooling effect), while the long-wave is positive (warming effect). However, cirrus in the tropics eventually exert an opposite radiative effect, as they tend to be optical thinner than at mid, or high latitudes. Thus, it is necessary to try to understand the behaviour of optically thin cirrus and their small and rough constituent ice particles in low and mid latitudes (at high latitude due to low sun the cirrus exert a positive forcing). To achieve this Ulanowski *et al.* [10] measured the scattered 2D pattern of artificial ice analogues with the Small Ice Detector (SID). They empirically proved that ice crystals with rough surface could reflect almost twice as much solar radiation back to space respect to the corresponding smooth particles (optically corresponds to a lower asymmetry parameter due to larger backscattered radiation). In particular, they proposed an explanation for the rarity of halos (as depicted in Figure 2.10). The halo features can be understood in the scattered radiation as the forward $22°$ and $46°$ peaks in the phase function (angular distribution of the radiation on the scattering plane) when the light is interacting with hexagonal plates and columns. The presence of irregularities on the surface, as rimed droplets, can destroy the halo peaks leading to a featureless phase function. This kind of smooth phase functions also agree well with satellite measurements (see next section). The corresponding 2D scattering pattern in the forward direction looks very complex with a speckle appearance (see chapter 5 for details).
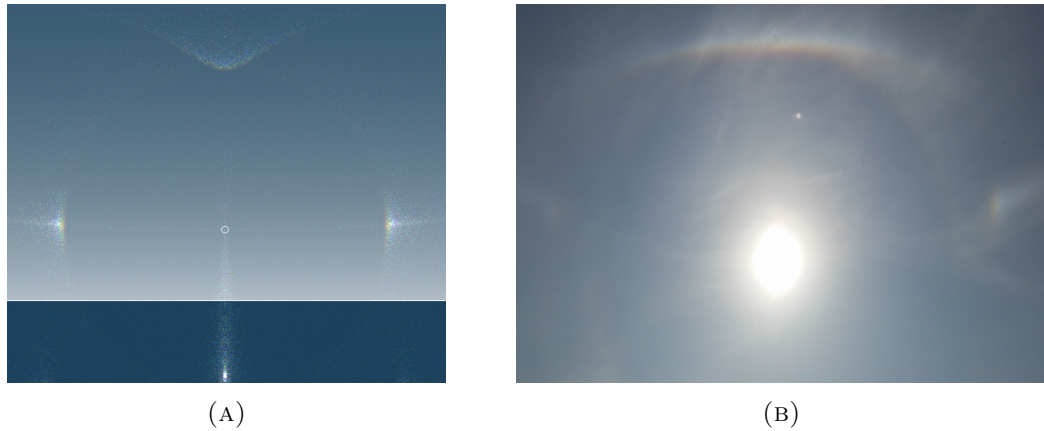
(A)   (B)

FIGURE 2.10: A simulated halo pattern with HaloSim (A) and a real one as appeared over Heidelberg on March the 13th, 2015 (B).

During field campaigns the direct probing of the constituent particles is possible through the use of research aircraft. A typical result is shown in Figure 2.12 where pictures of ice particles from the SPEC Cloud Particle Imaging (CPI) probe are presented [6]. It is immediately evident that nearly no regular shape is present and that the majority of the particles have a rough surface.

The CPI also reveals that smaller single ice crystals tend to remain at the cloud-top while bigger aggregates are taken down to the cloud-base by gravity [11]. The spatial distribution of shape and dimension of ice crystals is also related to the temperature and the relative humidity of the surrounding atmosphere as depicted in Figure 2.11.
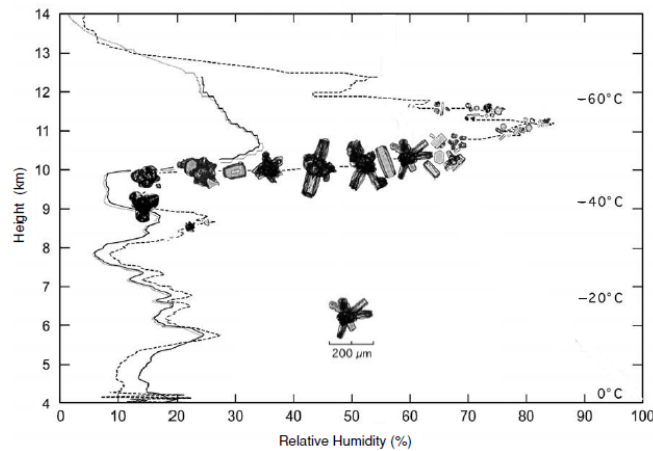
FIGURE 2.11: Size and shape distribution of ice crystals respect to altitude, temperature and relative humidity. Adapted from [5].

However, the CPI measurements turned out to be unable to provide information about very small particles due to its spatial resolution that imposes a lower limit of 35 μm for particles to be detectable. Thus, to better characterize the size and shape of small irregular ice crystals the SID instrument was built by Hirst *et al.* [12] (see chapter

for details). This device is not based on direct imaging of the particle instead it measures the forward scattered radiation of a visible light laser source at 532 nm. In that way particles between 1 μm and several hundreds microns can be studied and also the surface roughness can be measured. Recent field campaign measurements revealed that the majority of particles have rough and irregular surface thus producing speckle interference patterns in the forward scattered intensity [4].

FIGURE 2.12: Images of ice particles as recorded by the Cloud Particle Imager (CPI). Adapted from [6].

2.3 Rough particle modeling

Lower cirrus are typically composed of big ice particles with hexagonal shapes as columns or plates with the main dimension of some hundreds micrometers. These regular shapes are e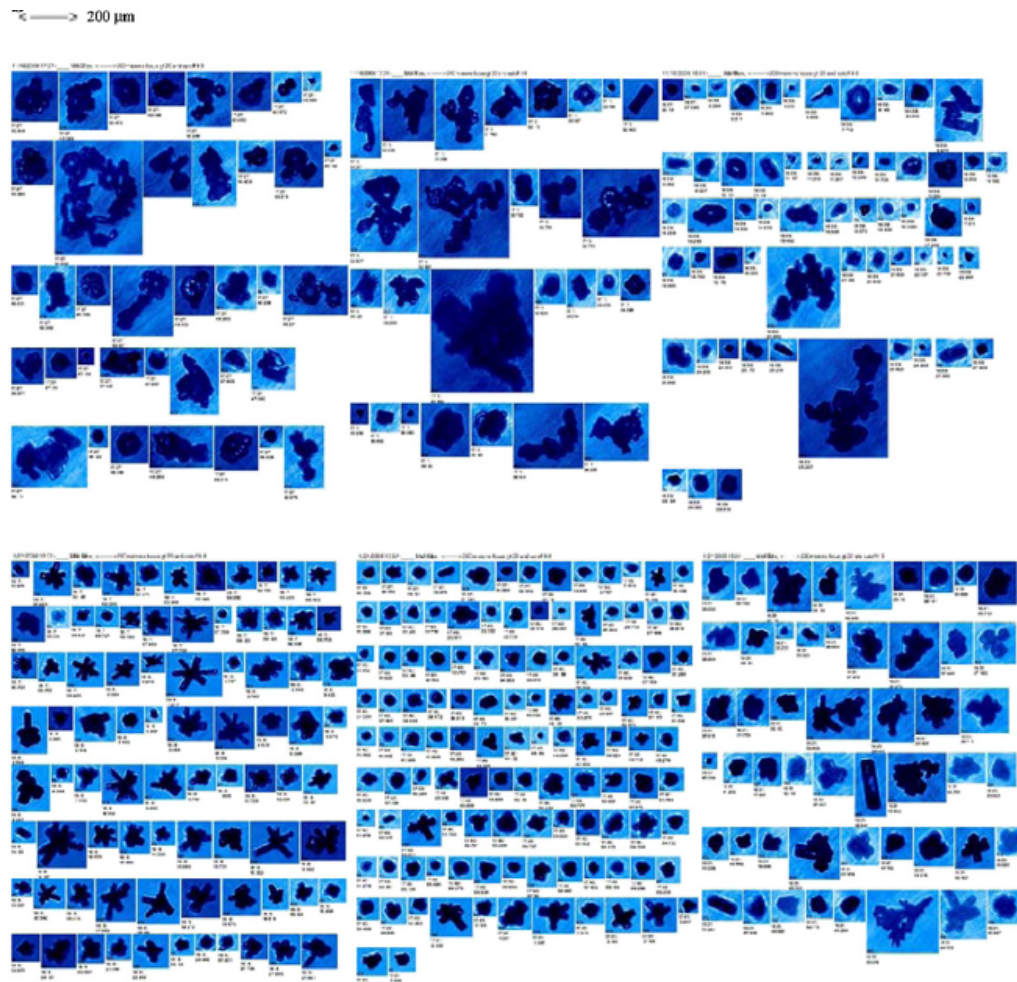xpected to give rise in the forward scattering directions to the 22° halo peak (Figure 2.10). However, the occurrence of halos is low. The rarity of halos was empirically explained by Kaye *et al.* [13] using the SID instrument. Irregularities on the surface of big hexagonal columnar particles can smooth the phase function erasing the halo peak. This behaviour is confirmed by theory. In particular Yang *et al.* [14] performed simulations with the geometric optics approximation method. They found that a rough particle surface can erase the halo peak from the phase function as in Figure 2.13.
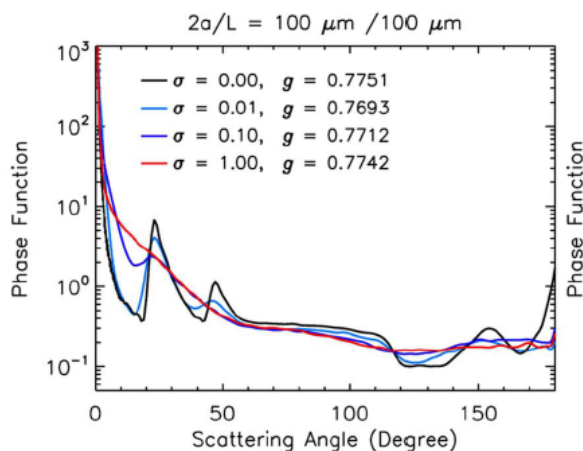
FIGURE 2.13: Phase functions of a hexagonal column averaged over orientation at $\lambda = 0.66\mu m$ for different values of the surface roughness expressed by the parameter σ. Adapted from [14].

A reduction of the asymmetry parameter g was also predicted. Further, they applied the calculation to the polarized reflectance measurements performed by the PARASOL instrument hosted on the MODIS satellite [15]. Importantly, they found that the experimental data can be reproduced only with large surface roughness for a habit of particles composed of different shapes (Figure 2.14).

All these simulations indicate the importance of the quality of the surface governing the distribution of the scattered light. However, the situation is different when smaller particles are considered. Muinonen *et al.* introduced the Gaussian random sphere model [16] and they applied it to study the optical properties of small particles [17]. They found that in general the behaviour is complex and that the reduction of the asymmetry parameter is dependent also on the bulk shape. The phase function is influenced but mostly in the backscattering part. The depolarization factor is the parameter that is mainly influenced by irregularities. Kahnert *et al.* also used different light scattering
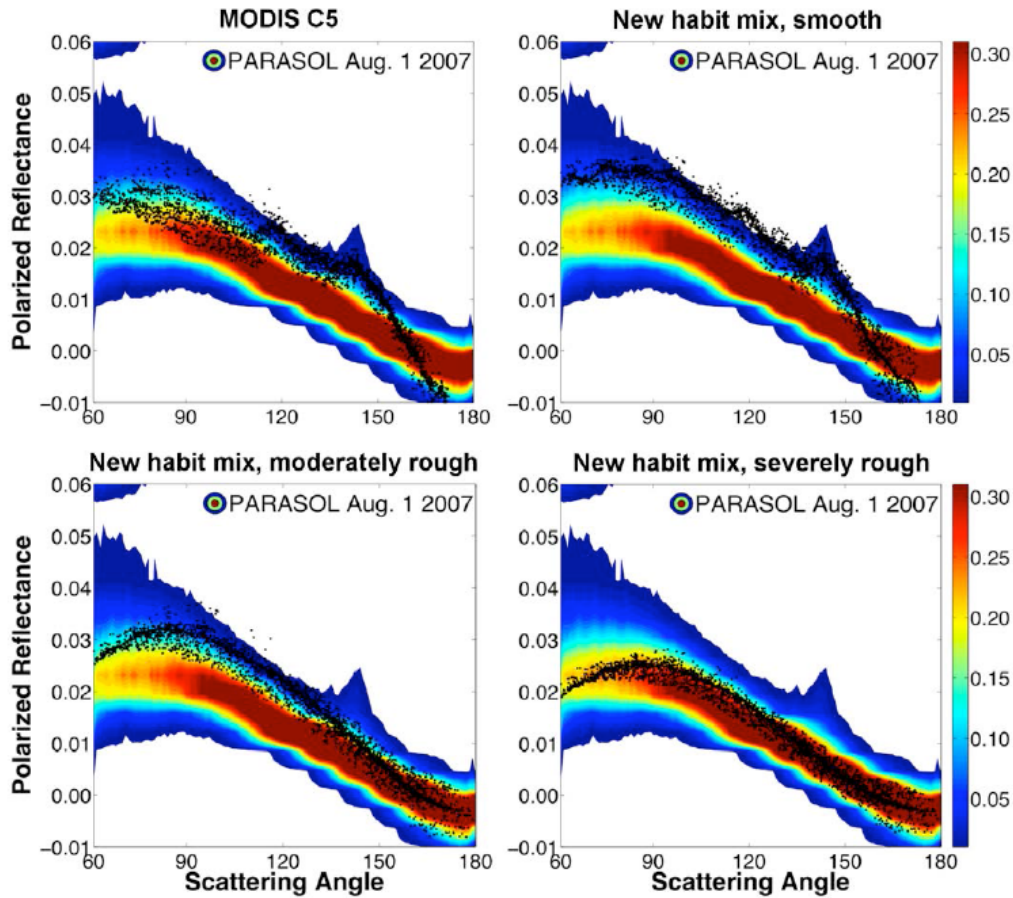
FIGURE 2.14: Normalized polarized reflectivity obtained by the PARASOL instrument (colors) and the corresponding calculation (black dots). The color contours represent the frequency of occurrence of polarized radiances for ice clouds. Adapted from [15].

methods in order to understand the effect of surface irregularities or roughness on the optical properties of small particles [18]. They conclude that the response of scattered light by small rough particles is complex and no general trend can be found as in the case of big ice crystals. Hence, more studies are necessary in order to understand the effect of roughness on small ice crystals. This need is well satisfied by the SID instrument that provide a unique tool to characterize small particles. Up to now no model was applied to simulate the scattering speckle patterns measured by the SID instrument and caused by small ice particles. The only attempts were done by Hesse *et al.* [19] but always in the large particle range using geometric optics applied to big facetted objects in order to simulate roughness. However, this method is limited to big particles where the geometric optics and diffraction theory are applicable.

To conclude, we note that in oder to reproduce in the simulation the speckle interference patterns as recorded by the SID instrument, it is necessary to make use of a model that is maintaining the wave nature of the electromagnetic field. For this reason we apply the

GDT-matrix model which turned out to be able to reproduce the interference patterns caused by small irregularities on the surface of the regular bulk of the particles (see chapter 6).

Chapter 3

Theory

3.1 Theoretical description of light

3.1.1 Maxwell's equations

The analytical description of light at mesoscale is based on classical electromagnetism (for light interacting with particles larger than 5 nm). This theory is formulated through the famous Maxwell's equations defining the electromagnetic field (that is also the first field to be relativistically invariant) as

$$\nabla \cdot \mathbf{D} = \rho \tag{3.1}$$

$$\nabla \times \mathbf{E} = -\frac{\partial \mathbf{B}}{\partial t} \tag{3.2}$$

$$\nabla \cdot \mathbf{B} = 0 \tag{3.3}$$

$$\nabla \times \mathbf{H} = \mathbf{J} + \frac{\partial \mathbf{D}}{\partial t} \tag{3.4}$$

where t is time, $\mathbf{E}$ and $\mathbf{H}$ the electric and magnetic fields, $\mathbf{B}$ the magnetic induction, $\mathbf{D}$ the electric displacement, ρ and $\mathbf{J}$ the macroscopic free charge and current densities (all the quantities are space and time dependent [20]). In particular, Eqs. 3.1 and 3.4 can be combined into the continuity equation

$$\frac{\partial \rho}{\partial t} + \nabla \cdot \mathbf{J} = 0. \tag{3.5}$$

The vector fields in the Maxwell's equations are related by the electric polarization $\mathbf{P}$ and the magnetization $\mathbf{M}$ (average electric/magnetic dipole moment per unit volume)

through

$$\mathbf{D} = \epsilon_0 \mathbf{E} + \mathbf{P} \tag{3.6}$$

$$\mathbf{H} = \frac{1}{\mu_0} \mathbf{B} - \mathbf{M} = 0 \tag{3.7}$$

with ϵ_0 and μ_0 the vacuum electric and magnetic permeability. A unique determination of the electric and magnetic fields (given charge and current distributions) is only possible considering the constitutive relations

$$\mathbf{J} = \sigma \mathbf{E} \tag{3.8}$$

$$\mathbf{B} = \mu \mathbf{H} \tag{3.9}$$

$$\mathbf{P} = \epsilon_0 \chi \mathbf{E} \tag{3.10}$$

where σ is the conductivity, μ the permeability and χ the electric susceptibility and are scalars for linear and isotropic media [20]. The Maxwell's equation are valid only in a volume where σ, μ and χ vary continuously (with discontinuities it is necessary to impose the continuity conditions for the fields at the boundary as done in Mie theory). It is assumed that all fields and sources are time-harmonic and can be represented as the real parts of the corresponding complex fields, for example

$$\mathbf{E}(\mathbf{r}, t) = Re(\mathbf{E}(\mathbf{r})e^{-i\omega t}) \tag{3.11}$$

with $\mathbf{r}$ the position vector, ω the angular frequency and i the complex unit. Then, the Maxwell's equations can be rewritten as

$$\nabla \cdot \mathbf{D}(\mathbf{r}) = \rho(\mathbf{r}) \tag{3.12}$$

$$\nabla \times \mathbf{E}(\mathbf{r}) = i\omega \mu \mathbf{H}(\mathbf{r}) \tag{3.13}$$

$$\nabla \cdot [\mu \mathbf{H}(\mathbf{r})] = 0 \tag{3.14}$$

$$\nabla \times \mathbf{H}(\mathbf{r}) = \mathbf{J}(\mathbf{r}) - i\omega \mathbf{D}(\mathbf{r}) = -i\omega \epsilon \mathbf{E}(\mathbf{r}) \tag{3.15}$$

with the complex permittivity $\epsilon = \epsilon_0(1 + \chi) + i\sigma/\omega$ resulting in a non-zero imaginary part of the refractive index i.e. causing the absorption of electromagnetic energy by converting it in heat. From the choice of the harmonic time dependence $e^{-i\omega t}$ follows also the fact that the imaginary part of the refractive index is positive defined i.e. $m = Re(m) + iIm(m)$.

3.1.2 Electromagnetic wave and polarization

The Maxwell's equations allow as a solution a plane electromagnetic wave propagating in a homogeneous medium without sources (representing the transport of electromagnetic energy of a perfect monochromatic parallel beam of light) i.e.

$$\mathbf{E}(\mathbf{r}, t) = \mathbf{E}_0 e^{i\mathbf{k}\cdot\mathbf{r} - i\omega t} \tag{3.16}$$

being $\mathbf{E}_0$ a constant complex vector describing polarization in Jones representation. The complete representation of polarization for an electromagnetic wave, in the sense that can describe also unpolarized light, is given by the Stokes vector. It is also important since it is the physical observable quantity since many instruments can not detect directly the electric (or magnetic) field, instead they measure a time average of the real part of linear combinations of products of fields with a dimension of an intensity. The electromagnetic wave in a non-absorbing medium is a transversal wave. Hence, the electric field can be expanded on a local vector base given by two directions $\hat{\mathbf{1}}$ and $\hat{\mathbf{2}}$ perpendicular to the propagation direction

$$\mathbf{E} = \mathbf{E}_{\hat{\mathbf{1}}} + \mathbf{E}_{\hat{\mathbf{2}}}. \tag{3.17}$$

Then, considering an electromagnetic plane wave, the associated Stokes vector can be defined as

$$\begin{bmatrix} I \\ Q \\ U \\ V \end{bmatrix} = \frac{1}{2}\sqrt{\frac{\epsilon}{\mu}} \begin{bmatrix} E_{0\hat{\mathbf{1}}}E_{0\hat{\mathbf{1}}}^* + E_{0\hat{\mathbf{2}}}E_{0\hat{\mathbf{2}}}^* \\ E_{0\hat{\mathbf{1}}}E_{0\hat{\mathbf{1}}}^* - E_{0\hat{\mathbf{2}}}E_{0\hat{\mathbf{2}}}^* \\ -E_{0\hat{\mathbf{1}}}E_{0\hat{\mathbf{2}}}^* - E_{0\hat{\mathbf{2}}}E_{0\hat{\mathbf{1}}}^* \\ i(E_{0\hat{\mathbf{2}}}E_{0\hat{\mathbf{1}}}^* - E_{0\hat{\mathbf{1}}}E_{0\hat{\mathbf{2}}}^*) \end{bmatrix}. \tag{3.18}$$

The first Stokes vector component, I, is the intensity while the others describe the polarization of the wave, and for a monochromatic wave are related by

$$I^2 = Q^2 + U^2 + V^2 \tag{3.19}$$

called the quadratic identity. The Stokes vector has also an ellipsometric interpretation given in Figure 3.1

3.2 Single scattering

3.2.1 The volume integral equation

An electromagnetic wave propagates in vacuum with constant intensity and polarization. However, if a particle is encountered, this can convert some of the electromagnetic
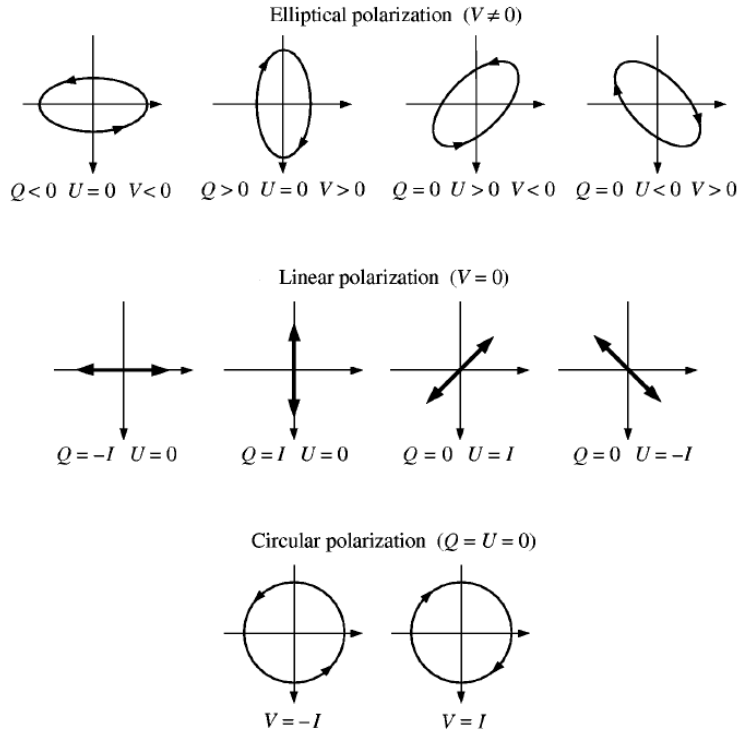
FIGURE 3.1: Different polarization realizations described by the tip of the oscillating real electric vector when the electromagnetic wave propagates towards the reader. Adapted from [20]

energy into heat, i.e. absorbing. Another portion of energy can be extracted from the incident beam by scattering. Hence, the energy of the incident wave is reduced by both absorption and scattering, the sum of which is called extinction. We consider only elastic scattering so that the frequency of the incoming wave is not changed by the scattering event in contrast to the polarization that is changed. In addition, we consider only monochromatic radiation i.e. the amplitude of the incident field fluctuates in time much more slowly than the time factor $exp(-i\omega t)$. This time factor is also not considered in a way that only stationary scattering is treated. It is assumed that the scattering system is formed by a dielectric, linear, isotropic and nonmagnetic particle, characterized by the dielectric constant ε, embedded into an infinite homogeneous background medium of dielectric constant ε_B (with $\varepsilon = \epsilon/\epsilon_0$). The bulk optical property ε, can be associated with the scatterer as soon as it is greater than 5 nm in order to exclude quantum mechanical effects. The scattering is described by the Maxwell's curl equations and for the external surrounding medium they are

$$\nabla \times \mathbf{E}(\mathbf{r}) = i\omega\mu_B\mathbf{H}(\mathbf{r}) \tag{3.20}$$

$$\nabla \times \mathbf{H}(\mathbf{r}) = -i\omega\epsilon_B\mathbf{E}(\mathbf{r})$$

while for the particle internal volume the corresponding equations are valid

$$\nabla \times \mathbf{E}(\mathbf{r}) = i\omega\mu\mathbf{H}(\mathbf{r}) \tag{3.21}$$

$$\nabla \times \mathbf{H}(\mathbf{r}) = -i\omega\epsilon\mathbf{E}(\mathbf{r})$$

where the subscript B indicates the exterior medium. Since the surrounding medium is nonmagnetic, we define $\mu = \mu_B = \mu_0$ with μ_0 the permeability of vacuum. Then, taking the curl of the curl of the first equations and solving for the electric field we get for the external volume

$$\nabla \times \nabla \times \mathbf{E}(\mathbf{r}) - k_B^2\mathbf{E}(\mathbf{r}) = 0 \tag{3.22}$$

and the equivalent for the internal volume

$$\nabla \times \nabla \times \mathbf{E}(\mathbf{r}) - k^2\mathbf{E}(\mathbf{r}) = 0 \tag{3.23}$$

with $k_0 = \omega\sqrt{\epsilon_0\mu_0}$, $k_B^2 = k_0^2\varepsilon_B$ and $k^2 = k_0^2\varepsilon$. The two homogeneous equations can be rewritten in a single inhomogeneous equation, the vector wave equation

$$\nabla \times \nabla \times \mathbf{E}(\mathbf{r}) - k_B^2\mathbf{E}(\mathbf{r}) = k_B^2[\frac{\varepsilon(\mathbf{r})}{\varepsilon_B} - 1]\mathbf{E}(\mathbf{r}) = k_0^2[\varepsilon(\mathbf{r}) - \varepsilon_B]\mathbf{E}(\mathbf{r}) \tag{3.24}$$

with the right-hand side vanishing outside the particle internal volume because $\triangle\varepsilon(\mathbf{r}) = [\varepsilon(\mathbf{r}) - \varepsilon_B] = 0$. As for any inhomogeneous linear differential equation, the solution can be found as the sum of the solution of the corresponding homogeneous equation plus a particular solution of the inhomogeneous equation. The homogeneous equation solution is the incident field and for the particular case considered here is a plane wave. Then, the physical appropriate particular solution is the scattered field [20]. Thus, the solution of the scattering problem is the total field that can be expressed through the volume integral equation (VIE) applying the Green's function technique

$$\mathbf{E}(\mathbf{r}) = \mathbf{E}^0(\mathbf{r}) + \int_V d\mathbf{r}'\mathbf{G}^B(\mathbf{r},\mathbf{r}') \cdot k_0^2\triangle\varepsilon(\mathbf{r}')\mathbf{E}(\mathbf{r}') \tag{3.25}$$

denoting with $\mathbf{E}^0$ the incoming field and considering as source term for the electric field the term $k_0^2[\varepsilon(\mathbf{r}) - \varepsilon_B]\mathbf{E}(\mathbf{r})$. Then, the Green's function for the background medium satisfies the same equation as Eq. (3.24), i.e. the vector wave equation but with a delta-like source term on the right side and is defined as

$$\begin{aligned} \mathbf{G}^B(\mathbf{r},\mathbf{r}') &= (\mathbf{1} + \frac{1}{k_B^2}\nabla \otimes \nabla)g^B(\mathbf{r},\mathbf{r}') \\ &= (\mathbf{1} + \frac{ik_BR-1}{k_B^2R^2}\mathbf{1} + \frac{3-3ik_BR-k_B^2R^2}{k_B^2R^4}\mathbf{R}\mathbf{R})\frac{e^{ik_BR}}{4\pi R} \end{aligned} \tag{3.26}$$

with $R = |\mathbf{r} - \mathbf{r}'|$ and the 3D scalar Green's function, ensuring that the solution goes to zero at infinity, is given by

$$g^B(\mathbf{r}, \mathbf{r}') = \frac{e^{ik_B|\mathbf{r}-\mathbf{r}'|}}{4\pi\,|\mathbf{r} - \mathbf{r}'|}. \tag{3.27}$$

The Lippmann-Schwinger equation Eq. (3.25) is mathematically a Fredholm integral equation with a kernel $\mathbf{G}^B$ that is singular for $\mathbf{r} = \mathbf{r}'$. In order to overcome the singularity in the volume integral equation, we have to consider the principal value of Eq. (3.25) as it is explained in the next chapter. Expanding the total field in terms of the incoming field [20–22] and applying formally the Born approximation to Eq. (3.25), one can rewrite it in a symbolic way, excluding for a moment the space-coordinates and defining the potential $v = k_0^2 \triangle\varepsilon(\mathbf{r})$

$$\big|\mathbf{E}\big\rangle = \big|\mathbf{E}_0\big\rangle + \mathbf{G}_B v\big|\mathbf{E}_0\big\rangle + \mathbf{G}_B v\mathbf{G}_B v\big|\mathbf{E}_0\big\rangle + \mathbf{G}_B v\mathbf{G}_B v\mathbf{G}_B v\big|\mathbf{E}_0\big\rangle + ... \tag{3.28}$$

Applying v on both sides of the above equation,

$$v\big|\mathbf{E}\big\rangle = v\big|\mathbf{E}_0\big\rangle + v\mathbf{G}_B v\big|\mathbf{E}_0\big\rangle + v\mathbf{G}_B v\mathbf{G}_B v\big|\mathbf{E}_0\big\rangle + ... = \mathbf{T}\big|\mathbf{E}_0\big\rangle \tag{3.29}$$

and defining the transition matrix $\mathbf{T}$ with

$$\mathbf{T} = v + v\mathbf{G}_B v + v\mathbf{G}_B v\mathbf{G}_B v + ... = \mathbf{T}_0 + v\mathbf{G}_B\mathbf{T} \tag{3.30}$$

thus the transition matrix can be interpreted as a generalized potential,

$$\big|\mathbf{E}\big\rangle = \big|\mathbf{E}_0\big\rangle + \mathbf{G}_B\mathbf{T}\big|\mathbf{E}_0\big\rangle \tag{3.31}$$

remembering that $\big|\mathbf{E}\big\rangle - \big|\mathbf{E}_0\big\rangle = \big|\mathbf{E}_{sca}\big\rangle$. Finally, projecting on the position eigenstates, the transition matrix can be introduced into the volume integral equation as

$$\mathbf{E}(\mathbf{r}) = \mathbf{E}^0(\mathbf{r}) + \int_V d\mathbf{r}'\mathbf{G}^B(\mathbf{r}, \mathbf{r}') \cdot \int_V d\mathbf{r}''\mathbf{T}(\mathbf{r}', \mathbf{r}'') \cdot \mathbf{E}^0(\mathbf{r}''). \tag{3.32}$$

The superscript 0 stays for the incoming field traveling in the background and not yet perturbed by the presence of the scatterer (i.e. the zero order in the perturbation series) while k_0 is the wave number of the electric wave in vacuum. Here the transition matrix again satisfies a Lippmann-Schwinger equation analogue to Eq. (3.25) i.e.

$$\mathbf{T}(\mathbf{r}, \mathbf{r}') = \mathbf{T}^0(\mathbf{r}, \mathbf{r}') + \int_V d\mathbf{r}''\mathbf{G}^B(\mathbf{r}, \mathbf{r}'') \cdot k_0^2\triangle\varepsilon(\mathbf{r}'') \cdot \mathbf{T}(\mathbf{r}'', \mathbf{r}') \tag{3.33}$$

with $\mathbf{T}_0(\mathbf{r}, \mathbf{r}') = k_0^2\triangle\varepsilon(\mathbf{r})\delta(\mathbf{r} - \mathbf{r}')\mathbf{1}$ in a unit volume, so that in 3D the transition matrix has the dimension of a length. Then, applying the Green's function technique as in the

quantum theory of scattering [21], a third integral equation for the Green's function dyadic (called Dyson equation) is obtained

$$\mathbf{G}(\mathbf{r}, \mathbf{r}') = \mathbf{G}^B(\mathbf{r}, \mathbf{r}') + \int_V d\mathbf{r}'' \mathbf{G}^B(\mathbf{r}, \mathbf{r}'') \cdot k_0^2 \triangle \varepsilon(\mathbf{r}'') \cdot \mathbf{G}(\mathbf{r}'', \mathbf{r}'). \qquad (3.34)$$

The dyadic $\mathbf{G}(\mathbf{r}, \mathbf{r}')$ represents the Green's tensor for the complete system with all the geometrical information of the medium in which the light propagates. We will show in the next chapter how to use Eqs. (3.33) and (3.34) in order to calculate the transition operator. Then, using Eq. (3.32) the electric field can be obtained both in near and far field.

3.2.2   The observables: The Müller matrix

All the information of an electromagnetic scattering event is encoded in the Müller matrix, which gives a complete description of light scattering for arbitrary polarized and also unpolarized light. Once the incident electric field is expressed by the Stokes vector [23], a multiplication with the Müller matrix representing the scattering process, results in the Stokes vector of the scattered outgoing field. All the optical properties of the particle can then be extracted from this matrix. According to [20] the Müller matrix can be calculated through the scattering amplitude $\mathbf{f}$. Assuming an incoming plane wave $\mathbf{E}^0(\mathbf{r}) = \mathbf{E}^0 \exp(ik_0\hat{\mathbf{n}}^0 \cdot \mathbf{r}) = \mathbf{E}^0 \left| K^0 \right\rangle$ the scattering amplitude is defined through

$$\mathbf{E}^{sca}(r\hat{\mathbf{n}}^{sca}) = \frac{e^{ik_0r}}{r}\mathbf{f}(\hat{\mathbf{n}}^{sca}, \hat{\mathbf{n}}^0) \cdot \mathbf{E}^0 \qquad (3.35)$$

where $\hat{\mathbf{n}}^{sca}$ and $\hat{\mathbf{n}}^0$ are the unit vectors along the scattered and incident field direction. To obtained the analytical expression for the scattering amplitude it is first necessary to calculate the Green's function in far-field. The expression for the far-field Green's function can be derived considering $\mathbf{r}' \in V$ and $\mathbf{r} = r\hat{\mathbf{n}}^{sca}$ with $k_0r \gg 1$ and also imposing that r is much greater than any dimension of the scattering object, i.e. $r \gg r'$. Then, we can exploit the expansion

$$\left|\mathbf{r} - \mathbf{r}'\right| = r\sqrt{1 - 2\frac{\hat{\mathbf{n}}^{sca} \cdot \mathbf{r}'}{r} + \frac{r'^2}{r^2}} \approx r - \hat{\mathbf{n}}^{sca} \cdot \mathbf{r}' + \frac{r'^2}{2r^2} \qquad (3.36)$$

and neglecting the last term of the expansion we get the approximation for the scalar Green's function for the background that for the particular case here considered is vacuum so $g^B = g^0$

$$g_{far}^0(\mathbf{r}, \mathbf{r}') = \frac{e^{ik_0r}}{4\pi r}e^{-ik_0\hat{\mathbf{n}}^{sca} \cdot \mathbf{r}'}. \qquad (3.37)$$

It follows that

$$\mathbf{G}^0_{far}(\mathbf{r}, \mathbf{r}') = (\mathbf{1} - \hat{\mathbf{n}}^{sca} \otimes \hat{\mathbf{n}}^{sca})\frac{e^{ik_0 r}}{4\pi r} e^{-ik_0 \hat{\mathbf{n}}^{sca} \cdot \mathbf{r}'}. \tag{3.38}$$

Substituting the far-field expansion of the Green's function in Eq. (3.32) and comparing with Eq. (3.35), the expression for the scattering amplitude is obtained

$$
\begin{aligned}
\mathbf{f}(\hat{\mathbf{n}}^{sca}, \hat{\mathbf{n}}^0) &= \frac{1}{4\pi}(\mathbf{1} - \hat{\mathbf{n}}^{sca} \otimes \hat{\mathbf{n}}^{sca}) \cdot \int_V d\mathbf{r}' \exp(-ik_0 \hat{\mathbf{n}}^{sca} \cdot \mathbf{r}') \cdot \\
&\quad \cdot \int_V d\mathbf{r}'' \mathbf{T}(\mathbf{r}', \mathbf{r}'') \exp(ik_0 \hat{\mathbf{n}}^0 \cdot \mathbf{r}'')
\end{aligned}
\tag{3.39}
$$

which contains the angular distribution of the scattered field. This can be also rewritten in a compact form [24] by choosing the scalar plane wave along the direction of the scattered field $|K^{sca}\rangle = \exp(ik_0 \hat{\mathbf{n}}^{sca} \cdot \mathbf{r}')$, coming from the far-field expansion of the background Green's function

$$\mathbf{f}(\hat{\mathbf{n}}^{sca}, \hat{\mathbf{n}}^0) = \frac{1}{4\pi}(\mathbf{1} - \hat{\mathbf{n}}^{sca} \otimes \hat{\mathbf{n}}^{sca})\langle K^{sca}|\mathbf{T}|K^0\rangle \tag{3.40}$$

where $\mathbf{f}$ has the dimension of a length and is independent from the incoming polarization [25]. Once $\mathbf{f}$ is known, the differential scattering cross-section for polarized light with polarization $\mathbf{E}^0$ is obtained from

$$\frac{d\sigma}{d\Omega} = |\mathbf{f} \cdot \mathbf{E}^0|^2. \tag{3.41}$$

For unpolarized light, the equivalent of the differential cross section is calculated through the scattering matrix $\mathbf{S}$. Since the incident electric field is always a transversal wave, the following condition needs to be fulfilled

$$\mathbf{f}(\hat{\mathbf{n}}^{sca}, \hat{\mathbf{n}}^0) \cdot \hat{\mathbf{n}}^0 = 0 \tag{3.42}$$

while the complementary condition for the scattered field is automatically accounted for since the far-field expansion of the wave guarantees a subtraction of any logitudinal component along the scattering direction [20]. Expanding the transversal field on the orthogonal 2D vector base already introduced, $\hat{\mathbf{1}}$ and $\hat{\mathbf{2}}$ in the plane perpendicular to the direction of propagation, it is possible to define the scattering matrix $\mathbf{S}$ through

$$\begin{bmatrix} E_1^{sca}(r\hat{\mathbf{n}}^{sca}) \\ E_2^{sca}(r\hat{\mathbf{n}}^{sca}) \end{bmatrix} = \frac{e^{ik_0 r}}{r}\mathbf{S}(\hat{\mathbf{n}}^{sca}, \hat{\mathbf{n}}^0)\begin{bmatrix} E_1^0 \\ E_2^0 \end{bmatrix} \tag{3.43}$$

with the elements of $\mathbf{S}$ given by the projections of $\mathbf{f}$ on the polarization vectors of the incoming and scattered waves

$$
\begin{aligned}
S_{11} &= \hat{\mathbf{1}}^{sca} \cdot \mathbf{f} \cdot \hat{\mathbf{1}}^0 \\
S_{12} &= \hat{\mathbf{1}}^{sca} \cdot \mathbf{f} \cdot \hat{\mathbf{2}}^0 \\
S_{21} &= \hat{\mathbf{2}}^{sca} \cdot \mathbf{f} \cdot \hat{\mathbf{1}}^0 \\
S_{22} &= \hat{\mathbf{2}}^{sca} \cdot \mathbf{f} \cdot \hat{\mathbf{2}}^0
\end{aligned}
\tag{3.44}
$$

Once the scattering matrix is obtained, the Müller matrix is calculated through linear combinations of the elements of $\mathbf{S}$ [20]. In the following, only the first element of the Müller matrix is used, i.e. the unpolarized light differential scattering cross-section

$$
Z_{11} = \frac{1}{2}(|S_{11}|^2 + |S_{12}|^2 + |S_{21}|^2 + |S_{22}|^2).
\tag{3.45}
$$

The other elements of the Müller matrix are given in [20].

Thus, from the definition of the scattering amplitude we see that once the transition matrix is calculated the scattering problem is solved because all the optical quantities descend from $\mathbf{f}$.

3.2.3 The optical properties

The optical properties are very useful when studying the scattering from multiple objects as in radiative transfer. In particular for radiative transfer applications the relevant optical properties are the extinction coefficient, the single scattering albedo and the asymmetry parameter (or all the phase function). Thus, we introduce here the definitions, while they are employed when doing radiative transfer simulations for a cloudy atmosphere in chapter 6. The determination of the electromagnetic field in the far-field zone allows to calculate the total scattering, absorption and extinction cross sections. The extinction cross section is given by [20]

$$
C_{ext} = \frac{4\pi}{k_B |\mathbf{E}^0|^2} Im[\mathbf{E}^{sca}(\hat{\mathbf{n}}^0) \cdot \mathbf{E}^{0*}]
\tag{3.46}
$$

where the expression is written on the polarization vectors. Then, the scattering total cross section is

$$
C_{sca} = \frac{1}{|\mathbf{E}^0|^2} \int_{4\pi} d\hat{\mathbf{n}}^{sca} |\mathbf{E}^{sca}(\hat{\mathbf{n}}^{sca})|^2 .
\tag{3.47}
$$

From the energy conservation we have

$$
C_{abs} = C_{ext} - C_{sca} \geq 0.
\tag{3.48}
$$

The extinction coefficient is defined for an ensemble of particles physically corresponding to the average of the extinction cross section for a distribution of particles in a physical volume. In order to obtain the extinction coefficient, it is necessary to average the single particle total extinction cross section first over all the different orientations and then, over the size distribution, giving the extinction coefficient for the bulk in units of an inverse length (this will be done in detail in chapter 4). The other relevant quantity for radiative transfer is the single scattering albedo,

$$\omega_0 = \frac{C_{sca}}{C_{ext}} \le 1. \tag{3.49}$$

This is interpreted as the probability that a photon interacting with the particle will be scattered rather than absorbed [20]. Hence, $\omega_0 = 1$ corresponds to non-absorbing particles. The last very important quantity that we consider is the so called phase function. This describes the angular distribution of the scattered radiation and is defined as

$$p(\hat{\mathbf{n}}^{sca}, \hat{\mathbf{n}}^0) = \frac{4\pi}{C_{sca}} \frac{dC_{sca}}{d\Omega}. \tag{3.50}$$

The phase function is then normalized to unity

$$\frac{1}{4\pi} \int_{4\pi} d\hat{\mathbf{n}}^{sca} p(\hat{\mathbf{n}}^{sca}, \hat{\mathbf{n}}^0) = 1. \tag{3.51}$$

The phase function is used as an angular distribution to calculate the average of the cosine of the scattering angle, called the asymmetry parameter

$$g = \langle cos(\theta) \rangle = \frac{1}{4\pi} \int_{4\pi} d\hat{\mathbf{n}}^{sca} p(\hat{\mathbf{n}}^{sca}, \hat{\mathbf{n}}^0) \hat{\mathbf{n}}^{sca} \cdot \hat{\mathbf{n}}^0. \tag{3.52}$$

Thus, the asymmetry parameter is positive when the particle scatters more light toward the forward direction, negative if the scattering is predominant in the backward direction and it vanishes if the scattering is symmetric (e.g. Rayleigh scattering).

3.3 Multiple scattering

3.3.1 Assumptions

The problem of single scattering can be solved directly from Maxwell's equations. However, often in real situations the light interacts with a system formed by a very large number of particles. Clouds of water or ice particles are the physical object in which we are interested in. Inside a cloud the particles are moving, spinning and also changing their shapes or sizes due to evaporation, condensation, sublimation and melting. Due to the fact that a measurement of light requires a finite amount of time to be performed,

the recorded signal results in a statistical average over the ensemble of states of the particles forming the total scattering object. This is related to the ergodic theorem which claims that only statistically averaged theoretical results can be compared with measured data. In particular, the light scattered in the far-field zone by a collection of moving particles produces random interference patterns that fluctuate in time and space. Although explicit measurements of the fluctuations of the speckle patterns are possible (diffusing wave spectroscopy in the contest of dynamic light scattering) we will just consider the static component of the scattering resulting from a calculation of averages [20]. Further, we consider scattering by macroscopic particles that can be characterized by a refractive index (bulk optical property independent from the electromagnetic field so nonlinearity is excluded), in a way that the multiple scattering concerns classical electromagnetic waves [26]. We concentrate on the coherent aspects of light and not on the photons properties because no quantization of energy is applied to the Maxwell's equation. Then, the scattering object can be seen as a spatial configuration of a number N of discrete finite particles (the particles are sufficiently large to ignore their atomic structure and only bulk optical properties are necessary). An electromagnetic plane wave illuminates the entire scattering object and interacts with the object as a whole with a spatial distribution of the refractive index. In addition the scattering is assumed to be elastic so that no frequency redistribution is considered as for Raman scattering or for small Doppler shift due to the movement of the particles. Moreover, all changes in the scattering object happens over a time period much longer than the period of time harmonic oscillations of the electromagnetic field. Conclusively, thermal emission is not taken into account because it can be safely neglected at temperature below or around room temperature for short wave infrared or shorter wavelengths (UV/visible light).

3.3.2 Foldy-Lax equations

The total scattered field can be calculated as a vector superposition of partial fields scattered by the individual particles forming the object [26]. Thus, the total field is

$$\mathbf{E}(\mathbf{r}) = \mathbf{E}^0(\mathbf{r}) + \sum_{n=1}^{N} \mathbf{E}_i^{sca}(\mathbf{r}) \tag{3.53}$$

with N the total number of particles and $\mathbf{E}_i^{sca}$ the ith partial scattered electric field. The partial scattered fields satisfy the vector Foldy-Lax equations that follow directly from the VIE and are exact. For the ith component

$$\mathbf{E}_i^{sca}(\mathbf{r}) = \int_{V_i} d\mathbf{r}' \mathbf{G}^B(\mathbf{r}, \mathbf{r}') \cdot \int_{V_i} d\mathbf{r}'' \mathbf{T}_i(\mathbf{r}', \mathbf{r}'') \cdot \mathbf{E}_i(\mathbf{r}'') \tag{3.54}$$

where V_i is the ith particle volume and most importantly $\mathbf{E}_i(\mathbf{r}'')$ is the electric field exciting particle i. Then, the T_i satisfies the Lippmann-Schwinger equation introduced in the previous section. Interestingly, it represents the transition operator for particle i in the absence of all the other particles. Hence, the transition operators are independent from each other while the exciting fields are interdependent and satisfy the system of N linear integral equations

$$\mathbf{E}_i(\mathbf{r}) = \mathbf{E}^0(\mathbf{r}) + \sum_{j(\neq i)=1}^{N} \int_{V_j} d\mathbf{r}' \mathbf{G}^B(\mathbf{r},\mathbf{r}') \cdot \int_{V_j} d\mathbf{r}'' \mathbf{T}_j(\mathbf{r}',\mathbf{r}'') \cdot \mathbf{E}_j(\mathbf{r}'') \tag{3.55}$$

for $\mathbf{r} \in V_i$ and $i = 1,...,N$. This connects directly to the concept of multiple scattering.

3.3.3 Diagrammatic representation of multiple scattering

It is possible to express the multiple scattering through an order-of-scattering expansion just rewriting Eq. (3.55) in a formal operator way (where two integrals over the internal volume of the particle considered, as in Eq. (3.55), are implied every time a Green's function and a transition operator are introduced). Iterating the same equation gives

$$E_i = E^0 + \sum_{j(\neq i)=1}^{N} \hat{G}\hat{T}_j E^0 + \sum_{\substack{j(\neq i)=1 \\ l(\neq j)=1}}^{N} \hat{G}\hat{T}_j\hat{G}\hat{T}_l E^0 + \sum_{\substack{j(\neq i)=1 \\ l(\neq j)=1 \\ m(\neq l)=1}}^{N} \hat{G}\hat{T}_j\hat{G}\hat{T}_l\hat{G}\hat{T}_m E^0 + ... \tag{3.56}$$

Recalling that

$$E = E^0 + \sum_{i=1}^{N} \hat{G}\hat{T}_i E_i \tag{3.57}$$

the scattered total field can be written as

$$E^{sca} = \sum_{i=1}^{N} \hat{G}\hat{T}_i E^0 + \sum_{\substack{i=1 \\ j(\neq i)=1}}^{N} \hat{G}\hat{T}_i\hat{G}\hat{T}_j E^0 + \sum_{\substack{i=1 \\ j(\neq i)=1 \\ l(\neq j)=1}}^{N} \hat{G}\hat{T}_i\hat{G}\hat{T}_j\hat{G}\hat{T}_l E^0 + ... \tag{3.58}$$

that represents the order-of-scattering expansion [26]. The term $\hat{G}\hat{T}_i E^0$ is the partial scattered field at the observation point generated by particle i in response to the incident field. Hence, the first term on the right-hand side of Eq. (3.58) is the sum of all single-scattering contributions, then the second term is the sum of all double-scattering contributions and so on. The order-of-scattering interpretation of Eq. (3.58) can be visualized as in Figure 3.2. Being the concept of multiple scattering an intuitive representation of the physical problem however, it can not be identified with a physical
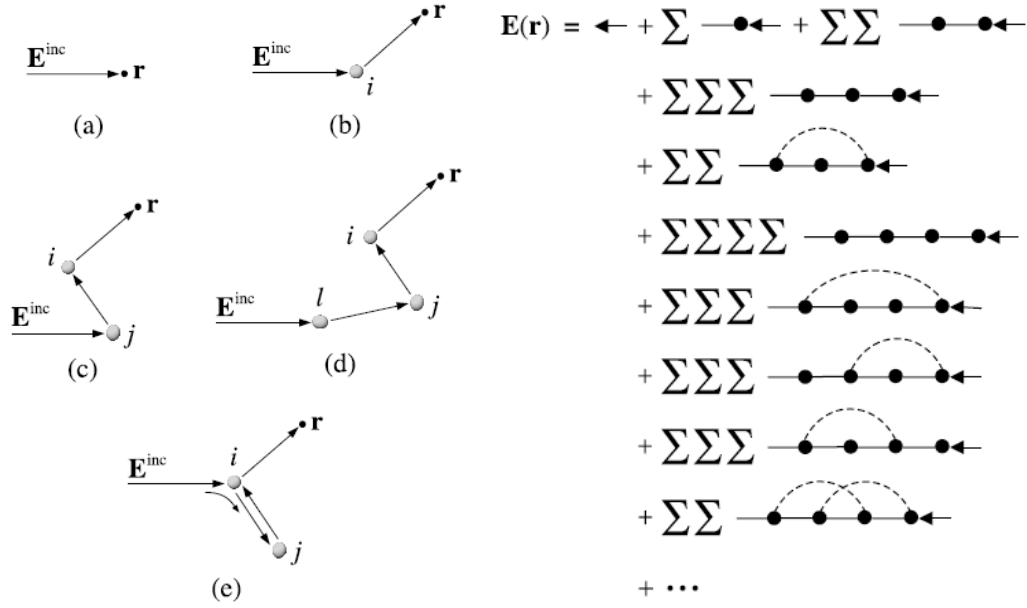
FIGURE 3.2: Left: (a) unscattered (incident) field, (b) single scattering, (c) double scattering, and (d and e) triple scattering. Right: Diagrammatic representation of Eqs. (3.57) and (3.58). Adapted from [26]

process per se (in the contest of frequency domain). Indeed, all the inter-particle interactions occur simultaneously and can not be temporally ordered. This results in the pure mathematical character of the multiple-scattering. To conclude, we introduce the diagrammatic representation of the order-of-scattering where the arrows represent the incident field, the line with the dot stays for a "multiplication" of a field by the $\hat{G}\hat{T}$ dyadic and the dashed curve indicates two scattering events involving the same particle [26].

3.3.4 The radiative transfer equation

In this subsection we go through all the logical steps involved in the analytical derivation of the radiative transfer equation (RTE) from Maxwell's equations, skipping the many mathematical theoretical details.

The main assumption under the RTE is that all the particles are in the far-field zone one respect to the other and also that the observation point is in the far-field respect to every particles. Thus, the RTE is not valid for densely packed objects composed of particles. The other fundamental assumption is called the Twersky approximation claiming that all paths going through a particle more than once can be neglected (thus the diagrams with dashed curves in Figure 3.2 are not taken into account). Besides these two major assumptions remains the ergodicity implying averaging over particle positions and states which also should be statistically independent. In addition, the

spatial distribution of the particles in the background medium should be random and statistically uniform. Considering that many instruments do not measure directly the electric field but the intensity, the relevant quantity to characterize multiple scattered radiation is the coherency dyadic

$$\mathbf{C}(\mathbf{r}) = \langle \mathbf{E}(\mathbf{r}, t) \otimes \mathbf{E}^*(\mathbf{r}, t) \rangle_t \approx \langle \mathbf{E}(\mathbf{r}, t) \otimes \mathbf{E}^*(\mathbf{r}, t) \rangle_{\mathbf{R}, \xi} \tag{3.59}$$

with $\mathbf{R}$ and ξ indicating the averaging over particle coordinates and states. After the averaging, the coherency dyadic becomes a continuous function over space (as the measured intensity). The Twersky expansion of the coherency dyadic can be depicted diagrammatically as in Figure 3.3. It is necessary to distinguish two types of diagrams
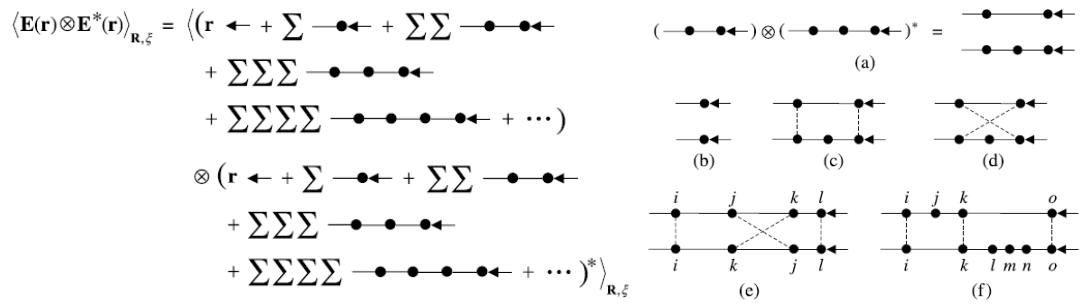
FIGURE 3.3: Left: the Twersky expansion of the coherency dyadic. Right: diagrammatic representation of the terms in the Twersky expansion. (a), (b), (c) and (f) are diagrams with no crossing connectors. (d) and (e) are diagrams with crossing connectors. Adapted from [26]

having common particles represented by the dashed lines. In particular, if the number of common particles is more than one, they can enter the upper and lower paths in the same order (Figure 3.3c) or in reversed order (Figure 3.3d). Then, due to the Twersky approximation, no particle can be the origin of more than one connector. The next assumption is key in order to arrive at the formulation of the RTE: all diagrams with crossing connectors can be neglected. This approximation is only valid when the observation point is located in the near-field of the whole object. Thus, the use of the RTE is justified only when simulating measurements in which the detector samples only a part of the object and do not perceive the object as a whole. This is exactly the situation encountered in real measurements of light scattered by a cloud and received by a detector mounted on-board a research aircraft or on satellites (RTE simulations in the presence of clouds are shown in chapter 6). The approximation can be intuitively understood as every interaction of the field with a particle is represented with Green's dyadic multiplied by the transition operator giving a fast oscillating exponential factor originating from the Green's dyadic. Upon position averaging over the positions of particles j and k in

Figure 3.3e the rapidly oscillating function vanishes. Further, considering the contribution of unconnected particles as particle j in Figure 3.3f, the only effect is to attenuate the field generated by particle k and exciting particle i. After these considerations the coherency dyadic can be represented through the ladder diagrams (Figure 3.4) where the double-lines denote the field attenuated by the unconnected particles, the Σ stays for summation over all appropriate particles and averaging over positions and states. It

FIGURE 3.4: Ladder approximation for the coherency dyadic. Adapted from [26]

is possible to expand the ladder coherency dyadic over the angular function called the ladder specific coherency dyadic $\boldsymbol{\Sigma}_L(\mathbf{r}, \hat{\mathbf{q}})$ i.e.

$$\mathbf{C}_L(\mathbf{r}) = \int_{4\pi} d\hat{\mathbf{q}} \boldsymbol{\Sigma}_L(\mathbf{r}, \hat{\mathbf{q}}) \tag{3.60}$$

where the integration is performed over all propagation directions $\hat{\mathbf{q}}$. It can be proved that the ladder specific coherency dyadic satisfies the RTE [26]. The dyadic $\boldsymbol{\Sigma}_L(\mathbf{r}, \hat{\mathbf{q}})$ can also be used to define the specific intensity column vector

$$\tilde{\mathbf{I}}(\mathbf{r}, \hat{\mathbf{q}}) = \begin{bmatrix} \tilde{I}(\mathbf{r}, \hat{\mathbf{q}}) \\ \tilde{Q}(\mathbf{r}, \hat{\mathbf{q}}) \\ \tilde{U}(\mathbf{r}, \hat{\mathbf{q}}) \\ \tilde{V}(\mathbf{r}, \hat{\mathbf{q}}) \end{bmatrix} = \frac{1}{2}\sqrt{\frac{\epsilon}{\mu}} \begin{bmatrix} \hat{\mathbf{1}} \cdot \boldsymbol{\Sigma}_L(\mathbf{r}, \hat{\mathbf{q}}) \cdot \hat{\mathbf{1}} + \hat{\mathbf{2}} \cdot \boldsymbol{\Sigma}_L(\mathbf{r}, \hat{\mathbf{q}}) \cdot \hat{\mathbf{2}} \\ \hat{\mathbf{1}} \cdot \boldsymbol{\Sigma}_L(\mathbf{r}, \hat{\mathbf{q}}) \cdot \hat{\mathbf{1}} - \hat{\mathbf{2}} \cdot \boldsymbol{\Sigma}_L(\mathbf{r}, \hat{\mathbf{q}}) \cdot \hat{\mathbf{2}} \\ -\hat{\mathbf{1}} \cdot \boldsymbol{\Sigma}_L(\mathbf{r}, \hat{\mathbf{q}}) \cdot \hat{\mathbf{2}} - \hat{\mathbf{2}} \cdot \boldsymbol{\Sigma}_L(\mathbf{r}, \hat{\mathbf{q}}) \cdot \hat{\mathbf{1}} \\ i\left[\hat{\mathbf{2}} \cdot \boldsymbol{\Sigma}_L(\mathbf{r}, \hat{\mathbf{q}}) \cdot \hat{\mathbf{1}} + \hat{\mathbf{1}} \cdot \boldsymbol{\Sigma}_L(\mathbf{r}, \hat{\mathbf{q}}) \cdot \hat{\mathbf{2}}\right] \end{bmatrix}, \tag{3.61}$$

which satisfies the RTE being just projections of the ladder specific coherency dyadic. The specific intensity satisfies the RTE in the integro-differential form

$$\hat{\mathbf{q}} \cdot \nabla \tilde{\mathbf{I}}(\mathbf{r}, \hat{\mathbf{q}}) = -n_0 \left\langle \mathbf{K}(\hat{\mathbf{q}}) \right\rangle_\xi \tilde{\mathbf{I}}(\mathbf{r}, \hat{\mathbf{q}}) + n_0 \int_{4\pi} d\hat{\mathbf{q}}' \left\langle \mathbf{Z}(\hat{\mathbf{q}}, \hat{\mathbf{q}}') \right\rangle_\xi \tilde{\mathbf{I}}(\mathbf{r}, \hat{\mathbf{q}}') \tag{3.62}$$

where $\left\langle \mathbf{K}(\hat{\mathbf{q}}) \right\rangle_\xi$ and $\left\langle \mathbf{Z}(\hat{\mathbf{q}}, \hat{\mathbf{q}}') \right\rangle_\xi$ are the extinction and the Müller matrix, averaged over particle states and $n_0 = N/V$, the particle number density. Firstly, it must be noted that the RTE satisfies the energy conservation law. Then it is interesting to note that the specific intensity differs from the Stokes vector because the first has the dimension of a radiance ($Wm^{-2}sr^{-1}$) while the second has the dimension of energy flux (Wm^{-2}). This

is a consequence of the coherency dyadic definition, its angular decomposition and the definition of the specific intensity. In addition, each particle with its individual extinction matrix and Müller matrix is effectively replaced with an average particle having the optical properties of the average of all particle states. It is also very interesting that the RTE has the mathematical structure of a Boltzmann's kinetic equation describing particle transport but it follows directly from the electromagnetic wave theory with no need to introduce photons [26]. If we then consider only the second order expansion on the position vector **r**, the equation reduces to the time-independent diffusion equation.

Conclusively, we recall the RTE for a plane-parallel, macroscopically isotropic and mirror-symmetric scattering medium that constitutes a good approximation for light propagating in the Earth atmosphere:

$$u\frac{d\tilde{\mathbf{I}}(\tau, \hat{\mathbf{q}})}{d\tau} = -\tilde{\mathbf{I}}(\tau, \hat{\mathbf{q}}) + \frac{1}{\langle C_{ext}\rangle_\xi} \int_{4\pi} d\hat{\mathbf{q}}' \left\langle \mathbf{Z}(\hat{\mathbf{q}}, \hat{\mathbf{q}}')\right\rangle_\xi \tilde{\mathbf{I}}(\tau, \hat{\mathbf{q}}') \tag{3.63}$$

where $\tau = n_0 \langle C_{ext}\rangle_\xi$ is the differential element of the optical thickness and $u = -cos(\theta)$ is the direction cosine.

3.3.5   Coherent backscattering

In deriving the RTE we noticed that it is possible to neglect the contribution of the crossed diagrams in near-field. This is no more valid if the observation point lies in the far-field zone of the object and within the "back shadow". The crossed diagrams cause what is known as weak localization that manifests itself in an increased backscattered intensity (coherent backscattering). Then, the total coherency dyadic can be rewritten as

$$\mathbf{C} = \mathbf{C}_L + \mathbf{C}_C \tag{3.64}$$

where the second term on right side is the cyclical coherency dyadic which can be calculated from the crossed diagrams. However, for very low density objects like the droplets concentration within clouds, the effect of the coherent backscattering is extremely small and can not be detected with passive instruments because the transport mean free path is order of magnitudes greater than the wavelength (in case of densely packed objects this is no more valid). Nevertheless, for active instruments like lidars or radars the coherent backscattering affects importantly the cloud measurements.

Chapter 4

Models

4.1 Single scattering

In this section we present first the model we developed to simulate small and very irregular particles, i.e. the Green's Dyadic technique for the Transition operator (the GDT-matrix model). The validation of the GDT-matrix against experimental single scattering measurements is presented in chapter 6. Secondly, we introduce the Mie theory for a single spherical scatterer that is used for numerical validation of the GDT-matrix. Then, we describe the Mie theory for a statistical size distribution of spherical particles the results of which are used in chapter 6 in order to perform radiative transfer simulations of a cloudy atmosphere.

4.1.1 The GDT-matrix model

Small ice particles have often low symmetry as anticipated by the studies mentioned in the introduction and as it is further exposed in chapter 5. This prevents the well known extended boundary condition method (EBCM) to be applicable for T-matrix calculations [20] in order to calculate optical properties of non-spherical particles. The lack of symmetry is naturally taken into account in techniques like the discrete (or coupled) dipole approximation (DDA or CDA), where the scatterer volume is discretized [27]. Thus the explicit consideration of boundary conditions for non-symmetric particles is not necessary. Due to the necessity of describing small scale surface irregularities, we adopt a DDA-like discretization of the general volume integral equation (VIE) for the electromagnetic field. There are three possibilities to write the volume integral equation. The first consists in writing it directly on the total field inside the integral, as

it is traditionally done in DDA models [28].

$$\mathbf{E}(\mathbf{r}) = \mathbf{E}^0(\mathbf{r}) + \int_V d\mathbf{r}' \mathbf{G}^B(\mathbf{r}, \mathbf{r}') \cdot k_0^2 \triangle \varepsilon(\mathbf{r}') \mathbf{E}(\mathbf{r}'). \tag{4.1}$$

Following this approach one evaluates the inverse of the interaction matrix and from this, the total field inside the particle is obtained. The second approach, called the Green's dyadic tensor method (GDT), consists in writing the volume integral equation on the incoming field and the total propagator $\mathbf{G}$

$$\mathbf{E}(\mathbf{r}) = \mathbf{E}^0(\mathbf{r}) + \int_V d\mathbf{r}' \mathbf{G}(\mathbf{r}, \mathbf{r}') \cdot k_0^2 \triangle \varepsilon(\mathbf{r}') \mathbf{E}^0(\mathbf{r}'). \tag{4.2}$$

and to solve for the propagator using Eq. (3.34) [29], i.e. solving the Dyson equation. In the last case, the volume integral equation looks as

$$\mathbf{E}(\mathbf{r}) = \mathbf{E}^0(\mathbf{r}) + \int_V d\mathbf{r}' \mathbf{G}^B(\mathbf{r}, \mathbf{r}') \cdot \int_V d\mathbf{r}'' \mathbf{T}(\mathbf{r}', \mathbf{r}'') \cdot \mathbf{E}^0(\mathbf{r}'') \tag{4.3}$$

i.e. rewritten on the incoming field and the transition matrix. The latter can be solved calculating the transition matrix with the corresponding integral equation i.e. Eq. (3.33). The last method is the one we implement here, named the Green's dyadic technique for transition matrix or the GDT-matrix. The transition operator as defined by its volume-integral should not be confused with the standard (in light-scattering community) T-matrix term connected to EBCM that exploits the ansatz of expanding the incident and scattered field in vector spherical harmonics. The transition operator connects the incoming field to the total internal field while the EBCM T-matrix connects the incoming field to the scattered field (theoretically the EBCM T-matrix is a particular representation of the transition operator based on spherical symmetry).

The GDT-matrix method relies on the Green's function technique, so the Dyson equation Eq. (3.34) is used to obtain the Green's propagator $\mathbf{G}$ inside the particle. This is calculated following a procedure first introduced by O. Martin *et al.* [30]. Then, this approach is expanded in an iterative way to the corresponding Lippmann-Schwinger equation for the transition matrix Eq. (3.33). This procedure constitutes a different direct method as compared to those reviewed by Yurkin and Hoekstra [28] regarding DDA models. In particular, the transition matrix can be identified as the inverse of the interaction matrix when reminding the definition of the scattering amplitude as introduced in DDA methods. The core of the GDT-matrix algorithm lies instead in the use of perturbation theory, so that the scatterer is seen as a local perturbation embedded into the surrounding optical medium [24]. Hence, the scatterer is discretized into voxels physically behaving as dipoles. Every single dipole (voxel) and its resulting perturbation to the incoming electric field is considered at each step in the perturbation series. So

dipole by dipole, every piece of the perturbation is added up, and at every iteration step the two Lippmann-Schwinger equations (one for $\mathbf{G}$ and one for $\mathbf{T}$) are reduced to algebraic equations to a form that only 3 by 3 matrices need to be multiplied and inverted (making the code easily computable in parallel). In addition, all the GDT-matrix scheme is set up in real space with no expansion of the field on vector spherical harmonics, giving a direct calculation of the transition matrix from its definition with no need to assume symmetries, except those inherent to the Maxwell's equations. The resulting algorithm is extremely simple, short, intuitive and thus easily changeable.

4.1.1.1 Green's function singularity and discretization

The main problem is that both Eqs. (3.33) and (3.34) have a singular kernel so before showing the details of the numerical technique we consider a practical strategy to circumvent the singularity of the Green's dyadic with same extremes. From the analytical expression of $\mathbf{G}^B(\mathbf{r}, \mathbf{r}')$, it is clear that its singularity at $\mathbf{r}' = \mathbf{r}$ causes a divergence of the volume integral equation and consequently of all the related Lippmann-Schwinger equations. This problem can be overcome considering the principal value of the integral in Eq. (3.33) (the same for Eq. (3.34)), introducing the depolarization dyadic $\mathbf{L}$

$$\mathbf{T}(\mathbf{r}, \mathbf{r}') = \mathbf{T}^0(\mathbf{r}, \mathbf{r}') + \lim_{\delta V \to 0} \int_{V - \delta V} d\mathbf{r}'' \mathbf{G}^B(\mathbf{r}, \mathbf{r}'') \cdot k_0^2 \triangle\varepsilon(\mathbf{r}'') \cdot \mathbf{T}(\mathbf{r}'', \mathbf{r}') - \mathbf{L} \cdot \frac{\triangle\varepsilon(\mathbf{r})}{\varepsilon_B} \mathbf{T}(\mathbf{r}, \mathbf{r}')$$

$$(4.4)$$

and excluding the singularity around $\mathbf{r}$, with $\mathbf{r}, \mathbf{r}' \in V$. The depolarization dyadic $\mathbf{L}$ depends on the shape of the exclusion volume δV. For a cubic mesh as the one here used it was given by Yaghjian [31]. Accordingly $\mathbf{L}$ is defined by $\mathbf{L} = \frac{1}{3}\mathbf{1}$ which acts as an extra source for the scattering potential, that takes into account the residual polarization of the mesh. We note here that $\mathbf{T}$ has no singularity in contrast to $\mathbf{T}(\mathbf{r}, \mathbf{r}) = k_0^2 \triangle\varepsilon(\mathbf{r}) \cdot \mathbf{1}$.

Now we deal with the singularity as considered in a finite discretization scheme, and specifically for a cubic mesh (all the three dimensions behave the same, giving a diagonal matrix). The iterative method applied to Eqs. (3.33) and (3.34) is not based on the Born approximation, instead it considers at each step the variation of the field due to one single perturbation ($\triangle\varepsilon(\mathbf{r})$). Thus a discretization of the scatterer is required. A convenient feature of a DDA model is that only the scatterer must be discretized. For that purpose, a 3D grid is defined with each mesh consisting of the elementary volume V_i at position $\mathbf{r}_i$ with $i = [1, N]$ where N is the total number of discretization volumes. For the discretization of the particle in cubic voxels, the Matlab tool "3D voxelizer" [32] is convenient since one only needs to provide a wavefront .obj file. Further, a sparse-octree algorithm is applied to refine the mesh at the surface. This proved to be important to accurately calculate the differential cross-section in the back-scattering part. Hence, the

Green's tensor in Eq. (3.34) is discretized on the mesh [29], as well as the transition matrix in Eq. (3.33) and the incoming field $\mathbf{E}_i^0$. In this way the discrete equivalent of Eq. (4.4) becomes a system of linear equations with $i, j = 1, ..., N$

$$\mathbf{T}_{i,j} = \mathbf{T}_{i,j}^0 + \sum_{n=1,n\neq i}^{N} \mathbf{G}_{i,n}^B k_0^2 \triangle\varepsilon_n V_n \mathbf{T}_{n,j} + \mathbf{M}_i k_0^2 \triangle\varepsilon_i \mathbf{T}_{i,j} - \mathbf{L} \cdot \frac{\triangle\varepsilon_i}{\varepsilon_B} \mathbf{T}_{i,j}. \tag{4.5}$$

The related discretized Dyson equation reads as

$$\mathbf{G}_{i,j} = \mathbf{G}_{i,j}^B + \sum_{n=1,n\neq i}^{N} \mathbf{G}_{i,n}^B k_0^2 \triangle\varepsilon_n V_n \mathbf{G}_{n,j} + \mathbf{M}_i k_0^2 \triangle\varepsilon_i \mathbf{G}_{i,j} - \mathbf{L} \cdot \frac{\triangle\varepsilon_i}{\varepsilon_B} \mathbf{G}_{i,j} \tag{4.6}$$

where the self-term $\mathbf{M}_i$ arises from the fact that the local source term is no more point-like but extended over the volume of the single voxel. Choosing cubic voxels, $\mathbf{M}_i$ is calculated as the principal value of $\mathbf{G}^B(\mathbf{r}_i, \mathbf{r}')$ over the single cell

$$\mathbf{M}_i = \lim_{\delta V \to 0} \int_{V_i - \delta V} d\mathbf{r}' \mathbf{G}^B(\mathbf{r}_i, \mathbf{r}'). \tag{4.7}$$

Properly choosing $\mathbf{M}$ is really important to increase the accuracy of the solution. In the computational scheme, this term acts as a correction due to the finite size of the mesh. It can be analytically obtained just approximating the shape of the cubic mesh with an equivalent spherical mesh of effective radius [33]

$$R_i^{eff} = (\frac{3}{4\pi} V_i)^{1/3} \tag{4.8}$$

and spherical volume δV. Following [33, 34], in 3D problems $\mathbf{M}$ reads as

$$\mathbf{M}_i = \frac{2}{3k_B^2} \left[(1 - ik_B R_i^{eff}) \exp(ik_B R_i^{eff}) - 1 \right] \mathbf{1}. \tag{4.9}$$

On the other hand, the transition matrix requires no renormalization and, in the discrete scheme at zero order it reads as $\mathbf{T}_{i,i}^0 = k_0^2 \triangle\varepsilon_i V_i$, with the dimension of a length (as required by the scattering amplitude definition).

4.1.1.2   The algorithm

In order to demonstrate how the algorithm works we focus on solving the equation for the transition matrix at the iteration step n

$$\mathbf{T}_{i,j}^n = \mathbf{T}_{i,j}^{n-1} + \mathbf{G}_{i,n}^{n-1} k_0^2 \triangle\varepsilon_n V_n \mathbf{T}_{n,j}^n \tag{4.10}$$

and the corresponding equation for the Green's function

$$\mathbf{G}_{i,j}^n = \mathbf{G}_{i,j}^{n-1} + \mathbf{G}_{i,n}^{n-1} k_0^2 \triangle \varepsilon_n V_n \mathbf{G}_{n,j}^n. \tag{4.11}$$

Again, we recall that the singularity of the Green's tensor must be treated through $\mathbf{M}$ and $\mathbf{L}$. The upper index refers to the perturbation order n, i.e. the number of $\triangle \varepsilon$ considered in the iteration. For a starting point assume $i = n$, Eq. (4.10) becomes algebraic and it can be easily solved for $\mathbf{T}_{n,j}$. Once the solution for $\mathbf{T}_{n,j}$ is obtained, its value is propagated by $\mathbf{G}_{i,n}^{n-1}$ to the other points inside the particle with $i = 1, ..., N$ through Eq. (4.11). For a more detailed description of the Green's dyadic technique see the papers by O. Martin *et al.* [29, 30]. For $i = j = n$ a modification of the algorithm is required to calculate the transition matrix, notably

$$\mathbf{T}_{n,n}^n = k_0^2 \triangle \varepsilon_n V_n \cdot \mathbf{1} \cdot (\mathbf{1} - \mathbf{G}_{n,n}^{n-1} k_0^2 \triangle \varepsilon_n V_n)^{-1}. \tag{4.12}$$

Once $\mathbf{T}_{i,j}^N$ is calculated, it represents the scattering contribution from the entire scatterer. The internal field can be calculated from

$$\mathbf{E}_i = \frac{1}{k_0^2 \triangle \varepsilon_i} \sum_{n=1}^{N} \mathbf{T}_{i,n}^N \cdot \mathbf{E}_n^0 \tag{4.13}$$

with $\mathbf{r} \in V$. Then, the field outside the particle is evaluated through Eq. (4.3). In order to get the far-field solution it is only necessary to make use of the corresponding far-field approximation of the background medium Green's tensor. To summarize, at step n the transition matrix is computed for the n perturbations and, in the next step $n + 1$, $\mathbf{T}_{i,j}^n$ is then reused in an iterative way; likewise for the Green's tensor. In particular, the transition matrix is processed at each step n, with the Green's tensor calculated at the previous step $n-1$. Then, the system of equations (e.g. Eq. (4.10)) is decomposed in nine sub-equations, one for each component of the transition matrix. For every component of the field, the scalar Helmoltz wave equation is solved. The same problem can be written as a linear system of $3N$ equations on the field components with complex coefficients and can be solved by the standard direct methods.

4.1.1.3   Validation

Further, the new scheme is first validated against known results in lower dimensions, such as a 1D dielectric barrier, or a 2D pad, and further against 3D results from Mie theory for a sphere and results from ADDA for scattering by a cube.

The first test is run for a scalar field hitting a dielectric 1D barrier, which can be regarded as a surrogate for a semi-transparent mirror. In the simulations, three different values for

the height of the barrier (the dielectric constant) are chosen in order to make the results comparable to the calculations of O. Martin *et al.* [30], i.e. $\varepsilon = 4, \varepsilon = 4+i, \varepsilon = 4+4i$. A plane wave with $\lambda = 0.8\mu m$ propagating in vacuum along the x axis hits the barrier from the left. Figure 4.1 shows the amplitude of the total field normalized to the amplitude of the incoming wave. The calculation is performed for a mesh size of $d = 0.01\mu m$ as in
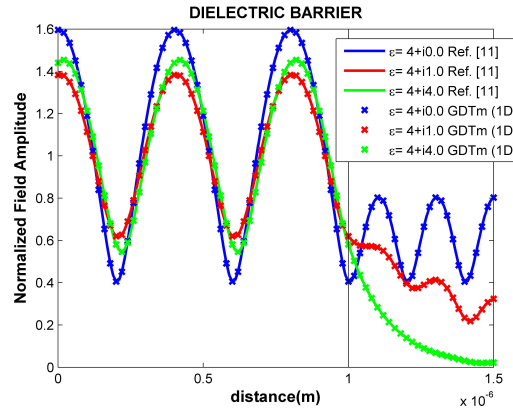

FIGURE 4.1: Dielectric barrier in 1D, a comparison between the GDT-matrix model and the results from O. Martin *et al.* [30]. A plane wave propagates from the left in vacuum ($\lambda = 0.8\mu m$) onto a dielectric barrier (in the right part of the plot) with the dielectric constants given in the legend. The amplitude of the normalized total field is shown. Adapted from [24].

O. Martin *et al.* [30] and a similar behaviour is observed regarding the accuracy of the model for a decreasing d and for a changing ε. We note that the boundary conditions are automatically satisfied at the interface between the two media. As the medium becomes more and more absorbent, the presence of an evanescent wave penetrating into the barrier is observed (the analogue of a tunneling behaviour of an electron in quantum mechanics).

Another example Figure 4.2 addresses the scattering of a 2D pad ($\varepsilon = 2$) by electromagnetic radiation discretized with a mesh size $d = 0.05\mu m$. A plane wave with $\lambda = 1\mu m$, linearly polarized perpendicularly to the pad plane is considered (scalar field solution). The field is penetrating through the pad (no absorption), and the normal modes develop in the same manner as in the study of O. Martin *et al.* [30]. Very good agreement is found again between the two studies. Here we note the ability of the GDT-matrix model to reproduce the high intensity forward peak, known in nano-optics as photonic jet. Simulations of a metallic pad are also performed (not shown) but convergence is only found for $d < 0.05\mu m$. This result indicates that our scheme may also be suitable to simulate problems in plasmonics.

Next, the scattering of a dielectric sphere with $\varepsilon = 1.1535 + i0.392$ and $x = 3.15$ is studied.
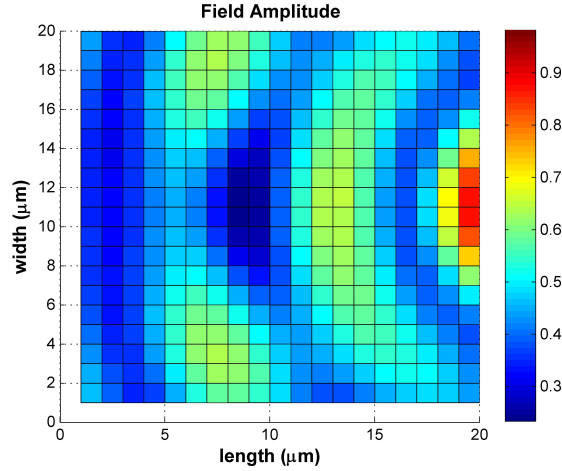
FIGURE 4.2: Dielectric barrier in 2D. A linear polarized plane wave is incident from the left on a square dielectric pad with $\varepsilon = 2$ and a side of $20\mu m$. The amplitude of the normalized total field is shown (color coded) inside the pad. Adapted from [24].

The simulations are performed in a manner to make the results comparable to the study [35]. Hence the differential scattering cross section for parallel and perpendicular polarization and for unpolarized light are compared with analytical exact results from Mie theory (we used our own code based on [36], see next subsection for details). We note that very good agreement is found for small size parameters $x < 7$ (Figure 4.3a). Then, increasing the size, a good agreement is found with Mie theory in parallel polarization for $x = 10$ and $N = 7326$ voxels (Figure 4.3b). When increasing the dielectric constant to $\varepsilon = 2.25$, the model starts to show some discrepancies for $x > 3$ with a maximum relative error of 35% in the back-scattering part of the diagram (Figure 4.3c). This is expected due to the sparse-octree discretization employed with $N = 7326$ voxels that has a bulk size of $d = 0.1\mu m$ which is not enough to model the oscillations of the field inside a single cell for that dielectric constant. However, this is the best result we can get with the available RAM in a reasonable computing time because a finer discretization of the bulk would require $N > 10^4$ voxels and thus, a much longer calculation time (see below for an extended discussion on the computation time). Finally, the scattering of a ice sphere with $\varepsilon = 1.72$ and $N = 7326$ voxels is discussed. The convergence for that discretization is poor in the back-scattering part but it is good in the forward-scattering half where the measurements are performed (Figure 4.3d). In Figure 4.4 a last comparison is done with the publicly-available DDA code ADDA [37] for a cube with $\varepsilon = 1.77$ and equivalent volume size-parameter $x = 3.22$ for a plane wave with a perpendicular incidence direction respect to the cube face. In order to use the results from ADDA as a reference, we run it for a cube with 128 dipoles per side ($N = 1,601,613$ dipoles). Instead, the discretization of the cubic particle for the GDT-matrix has $N = 1331$ (in unit of dipole size d). Then, we impose in the GDT-matrix code the rule of thumb that mandates $d = \lambda/10|m|$
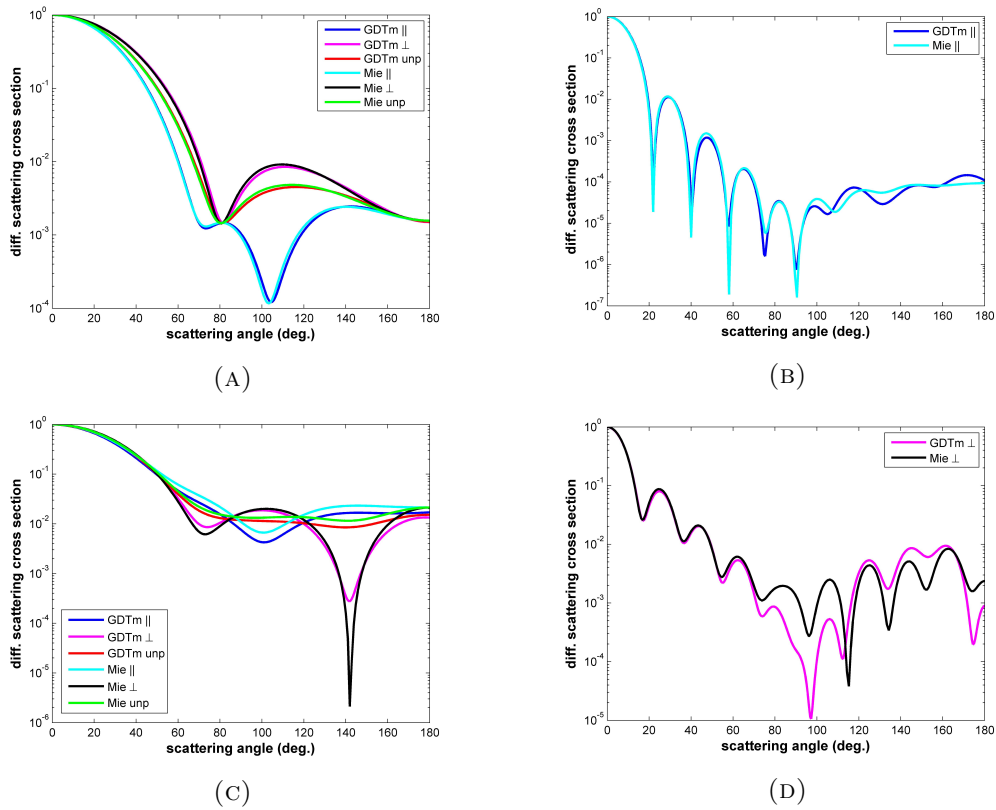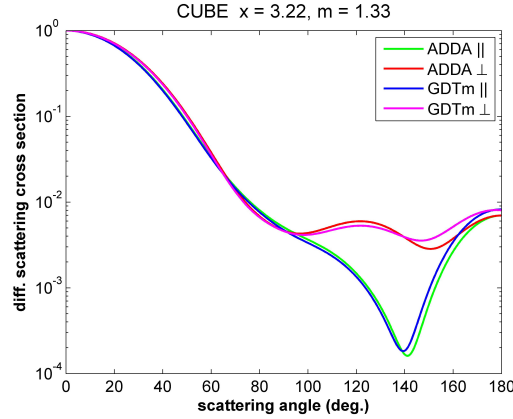
FIGURE 4.3: Differential scattering cross section as a function of the scattering angle (normalized to the maximum) simulated with the GDT-matrix and compared to the Mie theory for a dielectric sphere with (a) $\varepsilon = 1.1535 + i0.392$, $x = 3.15$ and $N = 2940$ voxels for unpolarized and parallel and perpendicular polarized light (b) $\varepsilon = 1.1535 + i0.392$, $x = 10$ and $N = 7326$ voxels for parallel polarized light (c) $\varepsilon = 2.25$, $x = 3.15$ and $N = 7326$ voxels for unpolarized and parallel and perpendicular polarized light (d) $\varepsilon = 1.72$, $x = 10$ and $N = 7326$ voxels for perpendicular polarized light. Adapted from [24].

for the size of the single dipole (fixing $\lambda = 2\pi$ as default in ADDA and with m the refractive index). With this change in the GDT-matrix code, we emphasize that the general behaviour of the differential scattering cross section is well reproduced in our calculation. However, some discrepancies arise in the backscattering directions and tend to grow when the dielectric constant and the size parameter are increased. In particular, when the size-parameter is increased (at fixed $\varepsilon < 2.25$), it is possible to reduce the error in the backscattering part taking a greater number of dipoles. In contrast, increasing the number of dipoles does not help when $\varepsilon > 2.25$ also for small size-parameters.

4.1.1.4 Performance

By exploiting the physical interpretation of the Green's tensor for the electromagnetic wave equation, it is possible to estimate the accuracy of the discretization process as exposed in [27]. Indeed, each column of $\mathbf{G}^B(\mathbf{r}, \mathbf{r}')$ represents the three components of

FIGURE 4.4: Differential scattering cross section as a function of the scattering angle (normalized to the maximum) for perpendicular and parallel polarizations of a cube with $\varepsilon = 1.77$ (refractive index $m = 1.33$) and $x = 3.22$. The plot displays the comparison between the ADDA code and the GDT-matrix code. The input for ADDA is a cube with number of dipoles $N = 1601613$ while for the GDT-matrix the cube has $N = 1331$. Adapted from [24].

the electric field radiated at location $\mathbf{r}$ by a unit dipole located at $\mathbf{r}'$. In order to improve the accuracy of the simulation, the distance d between the discretization volumes should be small as compared to any structural lengths of the scatterer and also compared to the wavelength inside the medium (a common feature of all DDA methods). Evidently the first requirement is best full-filled by employing enough voxels for a good approximation of the surface of the particle. In our study this task is reached through a sparse-octree discretizer. Sensitivity studies for curved surface particles indicate that the refinements near the edge of the scatterer lead to a better description of the cross section for back-scattering. The sparse-octree voxelization is justified since every potential interaction, i.e. $\triangle \varepsilon$, is weighted in the perturbation series with the volume of the corresponding cell. The use of sparse-octrees permits also to decrease the number of dipoles and accordingly the necessary calculation time. Then, the second requirement mandates that

$$\left| \sqrt{\varepsilon} \right| k_0 d < 1 \tag{4.14}$$

a condition that should always be checked for voxels in the bulk of the particle when the sparse-octrees are employed. Considering the size parameter $x = \frac{2\pi R^{eff}}{\lambda}$ (where R^{eff} is the same as in Eq. (4.8) but taking the entire volume of the particle) and substituting the wavelength in vacuum λ in Eq. (4.14), the maximum achievable size parameter can be estimated as a function of the mesh size d, the dielectric constant ε and the effective radius R_{eff}

$$x \leq \frac{R_{eff}}{d \left| \sqrt{\varepsilon} \right|}. \tag{4.15}$$

Further by defining the effective wavelength inside the particle as $\lambda_{eff} = \lambda/|\sqrt{\varepsilon}|$, which mandates $\lambda_{eff}/d > 2\pi$, at least six voxels per effective wavelength are required. With this restriction and the limitation on the number of dipoles N given by the computing time and the available RAM, our analysis is presently restricted to $\varepsilon \leq 2.25$, for which the maximum size parameter is $x_{max} = 10$ (considering $R_{eff} \cong 1\mu m$ and $d > 0.065\mu m$).

Introducing a higher order calculation of the **M** matrix, as it was proposed in [34], does not affect the result primarily because only one singularity per iteration step is considered. Moreover, the GDT-matrix scheme is stable with respect to the reduction of the voxel size. This is rooted in the use of the VIE. It is related to boundedness of the spectrum of the transition operator, that could be identified with the inverse of the interaction matrix (this is known from DDA models see [28]). In addition, better accuracy is achieved by increasing the number of dipoles N, a process that is yet limited by the available RAM and the computational time. Thus, the computational complexity remains of the order of $O(n_c^3)$ (with $n_c = 3N$). We tested the code on a 3.4 GHz quad-core machine with 32 GB of RAM for which in practice the calculations are restricted to $N < 10^4$ voxels. Figure 4.5 shows the performance plot as time versus the number of employed dipoles.
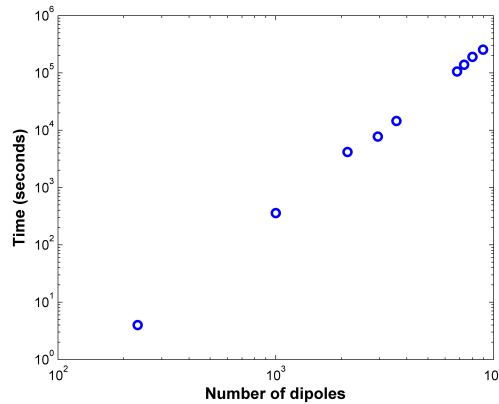
FIGURE 4.5: Log-log plot of the computation time versus the number of dipoles for a transition matrix calculation with the GDT-matrix model. Adapted from [24].

Since the GDT-matrix scheme belongs to the class of direct methods, it can be compared to other direct models. Conceptually all the three direct models [38–40] are equivalent to the GDT-matrix formulation taking into account all the multiple interactions between the dipoles. However, the GDT-matrix is computationally different in the sense that it iteratively solves two Lippmann-Schwinger equations, one for the propagator and one for the transition operator (or matrix through its representation on some basis). This leaves the same computational complexity of $O(n_c^3)$ as the models cited above and the same upper limit for the volume equivalent size-parameter i.e. $x \leq 10$.

Compared to iterative DDA methods [28], the GDT-matrix as a direct scheme is slower and more memory consuming. Indeed, the iterative methods have a computational complexity of $O(n_c)$. In particular, in the previous section we compared the GDT-matrix with the Amsterdam DDA model, ADDA [37]. We see that the two models agree well except in the backscattering part of the scattering cross section. The result was obtained in around one second using ADDA while it took around six minutes with the GDT-matrix on the same machine. This is due to the fact that ADDA is highly optimized (exploiting the symmetries of the interaction matrix and also implementing a FFT procedure). On the other hand, the GDT-matrix code is not optimized at all (up to now) and serves here as a proof-of-concept (no FFT and no exploitation of the symmetry of the transition operator). The GDT-matrix performance as a direct model can be also compared with the iterative DDA method implemented by Loke *et al.* [41]. We see that considering only a single calculation of the transition matrix (the inverse of the interaction matrix in [41]) the GDT-matrix is more than one hundred times slower than the iterative method. This is expected considering the difference between direct and iterative methods. Once the GDT-matrix code will be optimized, a more valuable comparison can be done.

However, the GDT-matrix retains a peculiarity in the sense that the calculation can be interrupted at any time resulting in a truncation of the perturbation series. If we combine this feature with a sparse-octree voxelization of the scatterer, the transition matrix for the bulk of the particle can be precalculated. Then, the contribution of the surface can be added to the solution using a refined discretization. This is possible because the index n, in the perturbation series can be truncated, while the other two indices i and j describe the dipole over which the perturbation is propagated. This allows to do a single calculation for the dipoles in the bulk and to study the effect of surface roughness or deformations repeating the run only for the dipoles on the surface. This approach results in a great saving of computing time and better accuracy due to the improved geometrical description of the surface.

4.1.2 Irregular shape generator: The Gaussian random sphere

In order to geometrically describe and parametrize the shape of irregular spherical particles we use the Gaussian random sphere model proposed by Muinonen *et al.* [16]. The model is based on random Gaussian deformations of the radial coordinate of a spherical particle described with spherical harmonics. Thus, assuming that N random variables $\mathbf{s} = (s_1, ..., s_N)$ given in spherical coordinates $\Omega = (\theta_1, \varphi_1; ...; \theta_N, \varphi_N)$ obey multivariate

normal statistics n_N with zero means and covariance matrix $\mathbf{\Sigma_s}$:

$$n_N(\mathbf{s}, \Sigma_s) = \frac{1}{(\sqrt{2\pi})^N \sqrt{det\mathbf{\Sigma}_s}} \exp\left(-\frac{1}{2}\mathbf{s}^T\mathbf{\Sigma}_s^{-1}\mathbf{s}\right). \tag{4.16}$$

The elements of the covariance matrix $\mathbf{\Sigma}_s$ are

$$\Sigma_{s,ij} = \beta^2 C_s(\gamma_{ij}), \qquad i,j = 1,...,N \tag{4.17}$$

with β^2 the variance, C_s the autocorrelation function and γ_{ij} the angular distance between the directions i and j. It is required for $\mathbf{\Sigma_s}$ to be positive definite, $C_s(0) = 1, C_s'(0) = 0$ and also the boundary condition $C_s(\gamma) = C_s(\gamma + 2\pi)$. Then, it is possible to introduce the random radius $\mathbf{r} = \mathbf{r}(\theta, \varphi)$ using the random variable called logradius $s = s(\theta, \varphi)$ as

$$\mathbf{r}(\theta, \varphi) = \frac{a}{\sqrt{1 + \sigma^2}} \exp\left[s(\theta, \varphi)\right]\mathbf{e}_r \tag{4.18}$$

where a is the mean radius, σ the relative standard deviation of the radius vector, and $\mathbf{e}_r$ a unit vector pointing outward in the radial direction . From this definition follows that the random variables $\mathbf{r} = (r_1, ..., r_N)$ obey the multivariate lognormal statistics l_N with equal means a, variance $a^2\sigma^2$ and covariance matrix $\mathbf{\Sigma}_r$. i.e.

$$l_N(\mathbf{r}, a, \mathbf{\Sigma}_r) = \frac{1}{(\sqrt{2\pi})^N r_1...r_N \sqrt{det\mathbf{\Sigma}}} \exp\left(-\frac{1}{2}\mathbf{s}^T\mathbf{\Sigma}_s^{-1}\mathbf{s}\right). \tag{4.19}$$

The covariance matrices, the corresponding autocorrelation functions and the variance are related by

$$\begin{aligned}
\Sigma_{r,ij} &= a^2[\exp(\Sigma_{s,ij}) - 1], \qquad i,j = 1,...,N \\
\sigma^2 C_r &= \exp(\beta^2 C_s) - 1, \\
\sigma^2 &= \exp(\beta^2) - 1,
\end{aligned} \tag{4.20}$$

which describe completely the statistics of the random shape [16]. Hence, the Gaussian random shapes can be generated exploiting a spherical harmonics expansion for the logradius and a Legendre expansion for the elements of the covariance matrices

$$\begin{aligned}
s(\theta, \varphi) &= \sum_{l=0}^{\infty} \sum_{m=-l}^{l} s_{lm} Y_{lm}(\theta, \varphi) \\
\Sigma_r(\gamma) &= \exp\left[\ln(\sigma^2 + 1)\sum_{l=0}^{\infty} c_l P_l(\cos(\gamma))\right] - 1,
\end{aligned} \tag{4.21}$$

being the P_l's the Legendre polynomials with weights c_l [17]. In practice, Gaussian random spheres are generated randomizing the harmonics weight coefficients s_{lm} which

have zero means and equal variances given by

$$\beta_{lm}^2 = (2 - \delta_{m0})\frac{(l-m)!}{(l+m)!}c_l\beta^2. \tag{4.22}$$

The last choice to be made regards the Legendre polynomials weights c_l. Following Nousiainen *et al.* [17] a good choice to generate realistic atmospheric particle shapes can be made with a power law relation

$$c_l \propto l^{-\nu}. \tag{4.23}$$

In addition, the l index should be truncated with proper extremes. We fix $l_{min} = 2$ and $l_{max} = 10$ as the first two orders give negligible contributions (increasing l_{min} gives particles with spikes [17]). In chapter 6 we show results obtained with a fixed power law with $\nu = 3$ as a function of different amplitudes of the distortion, parametrized with σ.

4.1.3 The Mie model for spheres

4.1.3.1 Mie theory for a single spherical particle: Introduction

A spherical scatterer can be treated analytically through the benchmark Mie theory [42]. The main idea consists in exploiting the spherical symmetry of the problem in a way that the electric internal, scattered and incident fields can be expanded on vector spherical harmonics [23]. Then, imposing the boundary conditions at the interface

$$(\mathbf{E}_0 + \mathbf{E}_{sca} - \mathbf{E}_{int}) \times \hat{\mathbf{e}}_r = (\mathbf{H}_0 + \mathbf{H}_{sca} - \mathbf{H}_{int}) \times \hat{\mathbf{e}}_r = 0 \tag{4.24}$$

where $\mathbf{E}_0$ is the incident field, $\mathbf{E}_{sca}$ the scattered field and $\mathbf{E}_{int}$ the internal field, the continuity of the field is ensured. From this continuity equation follow the expressions for the scattered field expansion coefficients which form the basis of the computational approach:

$$a_n = \frac{\psi_n(x)\psi_n'(mx) - m\psi_n'(x)\psi_n(mx)}{\zeta_n^{(1)}(x)\psi_n'(mx) - m\zeta_n^{(1)\prime}(x)\psi_n(mx)}, \tag{4.25}$$

$$b_n = \frac{\psi_n'(x)\psi_n(mx) - m\psi_n(x)\psi_n'(mx)}{\zeta_n^{(1)\prime}(x)\psi_n(mx) - m\zeta_n^{(1)}(x)\psi_n'(mx)}, \tag{4.26}$$

with m the refractive index, x the size parameter, a_n the nth electric partial wave amplitude and b_n for the magnetic partial wave amplitude (the prime indicates a derivative with respect to the argument of the function [36]). The functions $\psi_n(z)$ and $\zeta_n^{(1)}(z)$ are the Riccati-Bessel functions defined in terms of the spherical Bessel function of the first

kind, $j_n(z)$, and the spherical Hankel functions of the first kind, $h_n^{(1)}(z)$:

$$\psi_n(z) \equiv z j_n(z), \tag{4.27}$$

$$\zeta_n^{(1)}(z) \equiv z h_n^{(1)}(z). \tag{4.28}$$

The spherical Hankel functions of the first kind are used to describe the outgoing spherical waves in the scattered field amplitude. As already described in chapter 3, in the far field the electric field is a transversal wave thus having only two non-zero components. Hence, the scattered field can be described by the scattering matrix that reduces to a diagonal matrix with non-vanishing elements

$$S_{11}(x, m, \theta) = \sum_{n=1}^{\infty} \frac{2n+1}{n(n+1)} [a_n \pi_n(\cos\theta) + b_n \tau_n(\cos\theta)], \tag{4.29}$$

$$S_{22}(x, m, \theta) = \sum_{n=1}^{\infty} \frac{2n+1}{n(n+1)} [a_n \tau_n(\cos\theta) + b_n \pi_n(\cos\theta)], \tag{4.30}$$

with θ being the angle between the incident and scattered directions. The angular functions are written in terms of the Legendre polynomials as

$$\pi_n(\cos\theta) = \frac{1}{\sin\theta} P_n^1(\cos\theta)], \tag{4.31}$$

$$\tau_n(\cos\theta) = \frac{d}{d\theta} P_n^1(\cos\theta)]. \tag{4.32}$$

The sums are convergent for large n because the amplitude of the partial waves decreases with increasing order. In practice the sums are truncated according to Wiscombe [43] to the x dependent value

$$n_{max} = x + 4x^{1/3} + 2. \tag{4.33}$$

The scattering matrix elements are proportional to the scattering amplitude thus taking the square modulus of S_{11} and S_{22} gives the differential scattering cross section for perpendicular and parallel polarization respectively (with respect to the scattering plane). The unpolarized light differential scattering cross section i.e., the first element of the Müller matrix can be calculated taking the sum of the square modulus of the two scattering matrix elements

$$Z_{11} = 2 \cdot [(|S_{11}(x, m, \theta)|^2 + |S_{22}(x, m, \theta)|^2)/x^2] \cdot \frac{1}{4\pi Q_{sca}} \tag{4.34}$$

with Q_{sca} the scattering efficiency that is dimensionless being defined as the ratio of the corresponding cross section and the geometric cross section πr^2 (r is the radius of the

spherical particle). The efficiencies are given by

$$Q^{ext} = \frac{2}{x^2} \sum_{n=1}^{\infty} (2n+1)Re(a_n + b_n), \tag{4.35}$$

$$Q^{sca} = \frac{2}{x^2} \sum_{n=1}^{\infty} (2n+1)(|a_n|^2 + |b_n|^2). \tag{4.36}$$

The asymmetry parameter looks

$$\langle \cos\theta \rangle = \frac{\pi}{k_0^2 C_{sca}} \int_{-1}^{1} (|S_{11}(x,m,\theta)|^2 + |S_{22}(x,m,\theta)|^2) \cos\theta d(\cos\theta), \tag{4.37}$$

Then, the single scattering albedo is just the ratio of scattering and extinction efficiencies.

4.1.3.2   Mie theory: Numerical implementation

We developed our own code based on the numerical prescriptions described in [36]. Accordingly the scattered wave amplitude coefficients can be rewritten as

$$a_n = \frac{[\frac{A_n(y)}{m} + \frac{n}{x}]\psi_n(x) - \psi_{n-1}(x)}{[\frac{A_n(y)}{m} + \frac{n}{x}]\zeta_n^{(1)}(x) - \zeta_{n-1}^{(x)}(x)}, \tag{4.38}$$

$$b_n = \frac{\psi_{n-1}(x) - [mA_n(y) + \frac{n}{x}]\psi_n(x)}{\zeta_{n-1}^{(1)}(x) - [mA_n(y) + \frac{n}{x}]\zeta_n^{(1)}(x)}, \tag{4.39}$$

with $y = mx$ and the logarithmic derivative $A_n(y) = \psi_n'(y)/\psi_n(y)$. The Riccati-Bessel functions are generated in a stable way through the upward recurrence relation

$$\psi_n(x) = \frac{2n-1}{x}\psi_{n-1}(x) - \psi_{n-2}(x), \tag{4.40}$$

and similarly for $\zeta_n^{(1)}(x)$ with starting conditions $\psi_{-1}(x) = \cos x$, $\psi_0(x) = \sin x$ and $\zeta_{-1}^{(1)}(x) = \cos x + i\sin x$, $\zeta_0^{(1)}(x) = \sin x - i\cos x$. Moreover, the recurrence relation for the derivative

$$\psi_n'(x) = \psi_{n-1}(x) - \frac{n}{x}\psi_n(x), \tag{4.41}$$

and the one concerning the logarithmic derivative

$$A_n(y) = \frac{n+1}{y} - \frac{1}{A_{n+1}(y) + \frac{n+1}{y}}. \tag{4.42}$$

4.1.3.3 Single spherical particle: Water droplet

The use of Mie theory is justified for particles that do not deviate too much from a spherical shape. A typical example is a water droplet, small enough that the action of gravity is not sufficient to perturb significantly the spherical geometry. In Figure 4.6 we
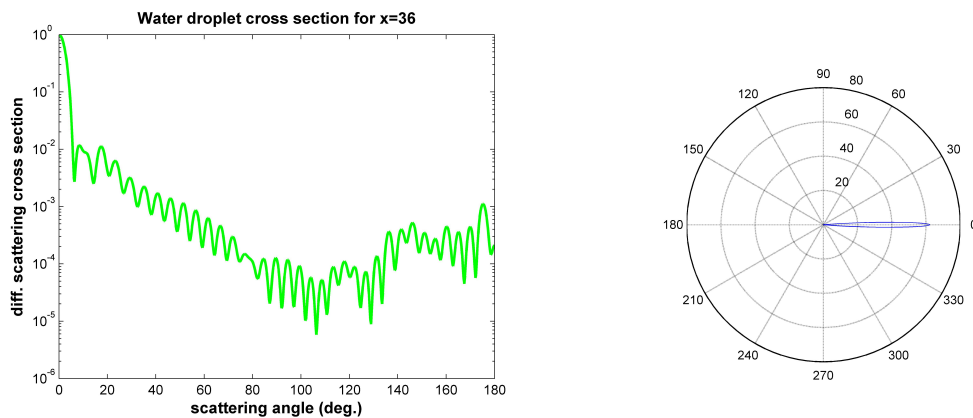
FIGURE 4.6: Single water droplet differential scattering cross section for unpolarized light. Left: linear plot. Right: polar plot.

show the differential scattering cross section for $x = 36$. The important characteristic is that the angular distribution of the differential scattering cross section shows some structures due to interference of the incident and scattered fields. The position of the maxima and minima can be used to retrieve the size of the spherical particle. The polar plot shows the shape of the angular distribution where the interference structures have very small amplitudes and thus are not visible.

Further, in Figure 4.7 we present the efficiency as a function of the size parameter for a water droplet $m = 1.33$ and a carbon soot particle $m = 1.78 + i0.92$. Increasing the imaginary part of the refractive index leads to an increased absorption as expected. The surprising fact is that the absorption efficiency can easily exceed unity in the resonance region of the size parameters [20]. This means that a particles can absorb significantly more power than the value of the incident intensity multiplied by the area of the particle geometrical cross section. Hence, the perturbation of the spherical particle on the electromagnetic field is far beyond its physical boundaries indicating the main limit of the geometrical optics approximation. The efficiencies are also characterized by low-frequency maxima and minima with superimposed high-frequency ripples. The interference structures are due to the interference of the diffracted and transmitted light through the particle (the phase shift is proportional to the real part of the refractive index). While the ripples are cause by resonances of the Mie coefficients a_n and b_n. Larger n, narrower become the ripples that can be identified with individual resonances of the corresponding partial waves. Also for ripples there is a physical interpretation.

When rays propagate around the inside surface of a spherical particle it is confined by an almost total internal reflection. Then, after total reflection the rays return to their entrance points exactly in phase and then follow the same path again and again without being attenuated by destructive interference. In this way very large energy density can be accumulated inside the particle near the surface. Since this accumulated energy is removed from the incident beam, the result of resonance is a larger extinction efficiency. The longer the path of the rays, the narrower the resonance. It should also be noted that an increased absorption erase the interference structures and also the ripples. Conclusively, we mention that the resonances are physical and can be measured providing a very accurate tool to characterize particles [20].
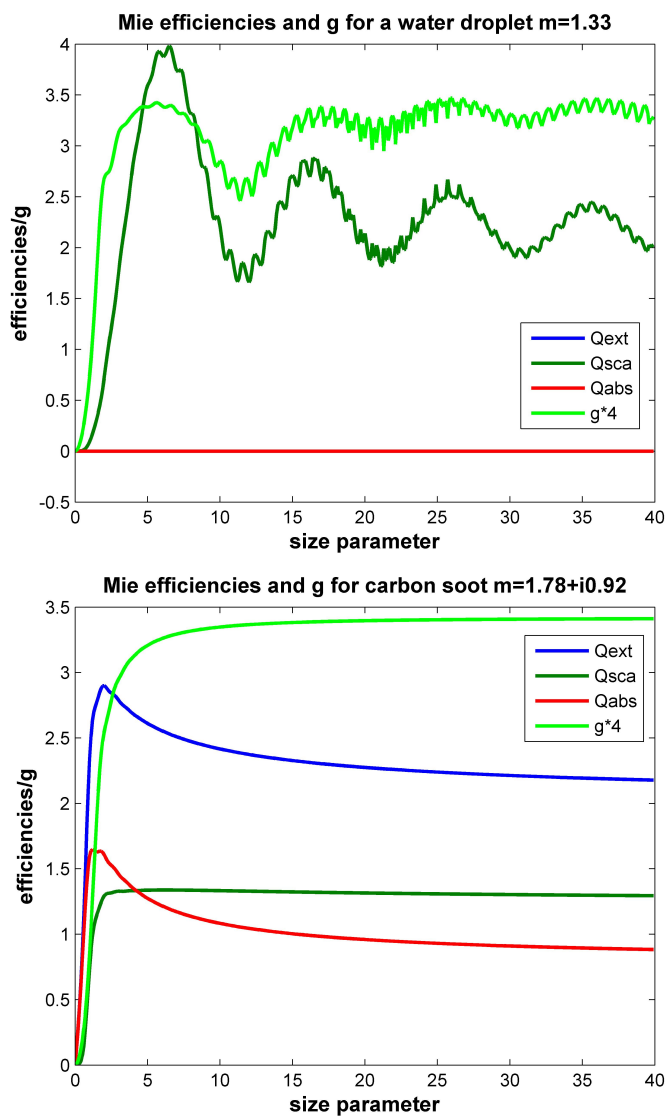
FIGURE 4.7: Efficiencies and asymmetry parameter *g* as a function of the size parameter. Upper plot: water droplet. Lower plot: carbon soot.

4.1.3.4 Statistical Mie theory for a distribution of particles: Bulk optical properties

Many instruments collect the intensity of light after multiple scattering by an ensemble of particles. In order to simulate the measurement process with the radiative transfer equation, an average over the particle states needs to be applied to the optical properties. Here we consider an ensemble of spherical water droplets with fixed spherical shape and refractive index. Thus, the statistical state on which it is required to perform the average is just the size of the particles. The size distribution can be defined as

$$N_0 = \int_0^\infty n(r)dr, \tag{4.43}$$

with N_0 the total number of particles per cubic centimeter and $n(r)$ the number density of the particles in the infinitesimal radius interval $[r, r + dr]$. Hence, the bulk optical properties (or averaged optical properties) can be calculated integrating the single particle properties over this distribution [36]. Consequently, the volume extinction coefficient can be calculated as

$$\beta^{ext} = \int_0^\infty \sigma^{ext}(r)n(r)dr, \tag{4.44}$$

having the dimension of an inverse length. A useful distribution to describe light scattering by atmospheric particles is the log normal distribution

$$n(r) = \frac{N_0}{\sqrt{2\pi}} \frac{1}{\ln S} \frac{1}{r} \exp\left[-\frac{(\ln r - \ln r_m)^2}{2\ln^2 S}\right], \tag{4.45}$$

where r_m is the median radius and $\ln S$ is the standard deviation of $\ln r$.

We can now calculate the extinction coefficient for a log normal distribution remembering that $\sigma^{ext} = \pi r^2 Q^{ext}$ and substituting in Eq. (4.44) reads

$$\beta^{ext} = \frac{N_0}{\ln S} \sqrt{\frac{\pi}{2}} \int_0^\infty rQ^{ext} \exp\left[-\frac{(\ln r - \ln r_m)^2}{2\ln^2 S}\right] dr. \tag{4.46}$$

All the optical properties can be averaged in this way and also the differential scattering cross section. In particular we are interested in the asymmetry parameter, the single scattering albedo and the extinction coefficient.

4.1.3.5 Statistical Mie theory for a distribution of particles: Water droplets

We present here the results for a log-normal size distribution of spherical water droplets with median radius $r_m = 7.5\mu m$, $N_0 = 100/cm^3$ and standard deviation $\ln S$ with $S = 2$ see Figure 4.8. First, we show in Figure 4.9 the differential scattering cross section aver-
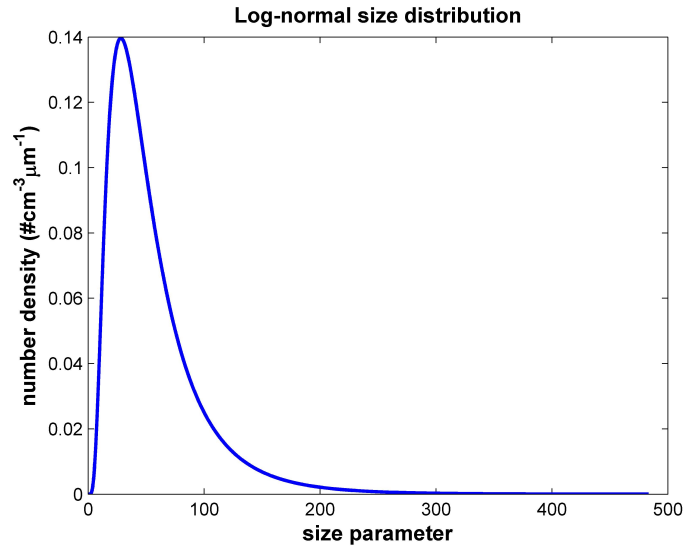
FIGURE 4.8: Log-normal size distribution as a function of the size parameter.

aged over that size distribution which can be compared with the one for a single particle of Figure 4.6. It is important to notice that the interference structures are smoothed out by the averaging procedure. Thus, making this distribution reproducible with good accuracy using the geometrical optics approximation where the ray approximation is applied in combination with diffraction, refraction and reflection (the Snell's law).
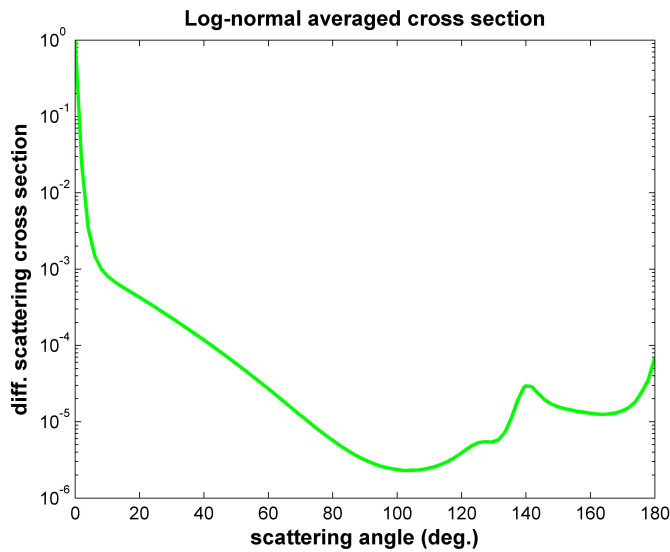
FIGURE 4.9: Bulk differential scattering cross section for water droplets with the log normal size distribution depicted in Figure 4.8.

To conclude, we show in Figure 4.10 the bulk optical properties as a function of the wavelength. It is important to remember also that the radiative transfer equation needs averages in order to be valid. Then, the bulk optical properties form the input for the

radiative transfer solver in order to simulate the radiance in a realistic atmosphere in the presence of cirrus, see chapter 6.
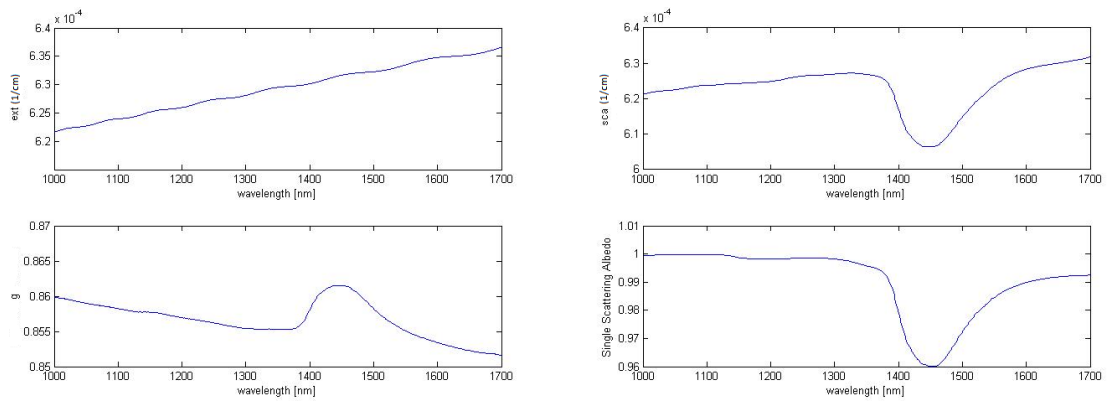
FIGURE 4.10: Bulk water droplet optical properties calculated with the size distribution of Figure 4.8 as a function of wavelength. Top left: the extinction coefficient. Top right: the scattering coefficient. Bottom left: the asymmetry parameter g. Bottom right: the single scattering albedo.

4.2 Multiple scattering

4.2.1 The radiative transfer model McArtim

4.2.1.1 The RTE formal solution

In the attempt to simulate and interpret spectral radiances measured by passive remote sensing instruments (as the mini-DOAS instrument, see chapter 5) we make use of the radiative transfer model called McArtim [44]. Here we provide a description of its principles while its outcomes are presented in chapter 6. We consider the scalar approximation of the RTE i.e. considering only the first component of the specific intensity vector that is the radiance. Then, we recall that only elastic scattering is considered. Both these approximations are accurate enough to describe the propagation of radiation from the Sun through the Earth atmosphere also in the presence of clouds.

The radiative transfer equation then writes

$$\hat{\mathbf{q}}\nabla\tilde{I}(\mathbf{r},\hat{\mathbf{q}}) = -\beta_{ext}(\mathbf{r})\tilde{I}(\mathbf{r},\hat{\mathbf{q}}) + \frac{\beta_{sca}(\mathbf{r})}{4\pi}\int_{4\pi}\tilde{I}(\mathbf{r},\hat{\mathbf{q}}')Z_{11}(\mathbf{r},\hat{\mathbf{q}}\cdot\hat{\mathbf{q}}')d\hat{\mathbf{q}}' + S(\mathbf{r}) \qquad (4.47)$$

which is the scalar RTE deduced from Eq. (3.62) introduced in chapter 3. The first term on the right hand side is the attenuation due to extinction, the second term represents scattering and the last is the source term. Disregarding the thermal emission of the atmospheric particles or molecules and the Earth thermal emission, the source density reduces to

$$S(\mathbf{r}) = P_0(\lambda)\Theta_{Sun}(\mathbf{r})\frac{1}{V_{Sun}} \qquad (4.48)$$

where P_0 is the spectral power of the Sun, V_{Sun} the volume of the Sun and Θ_{Sun} is the Heaviside step function describing the Sun location. It is convenient to rewrite the integro-differential equation (4.47) as an integral equation only making use of the Green's function technique. Rewriting Eq. (4.47) as

$$\left[1 + \frac{1}{\beta(\mathbf{r})}\hat{\mathbf{q}}\nabla\right]\tilde{I}(\mathbf{r},\hat{\mathbf{q}}) = \frac{\omega_0(\mathbf{r})}{4\pi}\int_{4\pi}\tilde{I}(\mathbf{r},\hat{\mathbf{q}}')Z_{11}(\mathbf{r},\hat{\mathbf{q}}\cdot\hat{\mathbf{q}}')d\hat{\mathbf{q}}' + \frac{1}{\beta(\mathbf{r})}S(\mathbf{r}) \qquad (4.49)$$

with ω_0 the single scattering albedo, it is possible to recognize on the left side into the square brackets a differential operator. The corresponding Green's function is

$$G_{\hat{\mathbf{q}}}(\mathbf{r},\mathbf{r}') = \frac{\beta(\mathbf{r}')\exp\left[-\tau(\mathbf{r},\mathbf{r}')\right]}{|\mathbf{r}-\mathbf{r}'|^2}\delta\left(\hat{\mathbf{q}} - \frac{\mathbf{r}-\mathbf{r}'}{|\mathbf{r}-\mathbf{r}'|}\right) \qquad (4.50)$$

where the δ distribution selects only points $\mathbf{r}$ on the line $\mathbf{r}' + t\hat{\mathbf{q}}$ with $t > 0$. The optical thickness can be defined as

$$\tau(\mathbf{r}, \mathbf{r}') = \int_0^{|\mathbf{r}-\mathbf{r}'|} \beta_{ext}(\mathbf{r}' + t\hat{\mathbf{q}})dt. \tag{4.51}$$

The last step consists in defining the collision density as $f = \tilde{I}\beta_{ext}$. Then, the integral RTE can be written as

$$f(\mathbf{r}, \hat{\mathbf{q}}) = \int_M \int_{4\pi} \delta\left(\hat{\mathbf{q}} - \frac{\mathbf{r} - \mathbf{r}'}{|\mathbf{r} - \mathbf{r}'|}\right) \frac{k_p[(\mathbf{r}', \hat{\mathbf{q}}') \to (\mathbf{r}, \hat{\mathbf{q}})]}{|\mathbf{r} - \mathbf{r}'|^2} f(\mathbf{r}', \hat{\mathbf{q}}')d\hat{\mathbf{q}}'d\mathbf{r}' + \Psi(\mathbf{r}, \hat{\mathbf{q}}). \tag{4.52}$$

Here the transition density is given by

$$k_p[(\mathbf{r}', \hat{\mathbf{q}}') \to (\mathbf{r}, \hat{\mathbf{q}})] = \omega_0(\mathbf{r}')\frac{Z_{11}(\mathbf{r}, \hat{\mathbf{q}} \cdot \hat{\mathbf{q}}')}{4\pi}\beta_{ext}\exp\left[-\tau(\mathbf{r}, \mathbf{r}')\right] \tag{4.53}$$

and the initial collision density is

$$\Psi(\mathbf{r}, \hat{\mathbf{q}}) = \beta_{ext}\int_M \delta\left(\hat{\mathbf{q}} - \frac{\mathbf{r} - \mathbf{r}'}{|\mathbf{r} - \mathbf{r}'|}\right) S(\mathbf{r}')\frac{\exp\left[-\tau(\mathbf{r}, \mathbf{r}')\right]}{|\mathbf{r} - \mathbf{r}'|^2}d\mathbf{r}' \tag{4.54}$$

where the spatial integrations are carried out over the spatial domain M including the Earth and the Sun.

The numerical solution can be found through the formal solution of the IRTE that can be rewritten shortly as

$$f = Kf + \Psi. \tag{4.55}$$

Applying the Born approximation, i.e. taking as the initial guess for the collision density inside the integral the initial collision density and iterating gives the solution as

$$\tilde{f} = \sum_{n=0}^{\infty} K^n \Psi \tag{4.56}$$

known as Neumann series that converges if $||K|| < 1$. Thus, once the solution is found, from the collision density one can easily get the radiance dividing by the extinction coefficient at the observation point. In order to get the measured signal also an integration of the radiance over the field of view of the instrument is required. To optimize this procedure the light rays are traced back i.e. starting from the detector and reaching the Sun (see Figure 4.11).
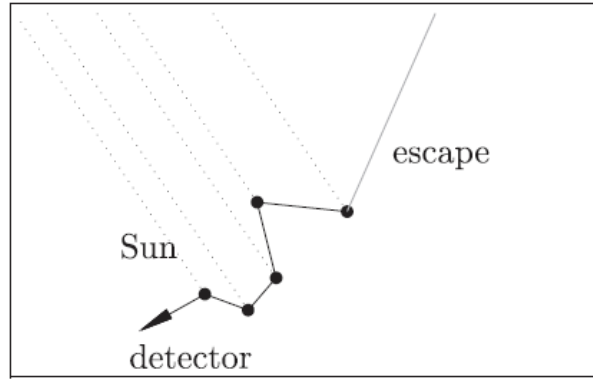
FIGURE 4.11: A ray of light trajectory (random walk) as simulated by McArtim when the ray is started at the detector and propagated backward. Adapted from [44].

4.2.1.2 The numerical solution through Monte Carlo sampling

As the Neumann series is a high dimensional integration problem it can be handled with a Monte Carlo method. Random numbers are used to draw samples from the probability density function associated to the respective integration kernel.

First of all McArtim initializes a grid (also with spherical symmetry) and on the grid points all the atmospheric properties are stored as temperature and pressure then the air density is calculated according to the ideal gas law. In addition, for the wavelength considered a second data structure is initialized on the same grid but containing the optical properties of the scatterers i.e. the extinction coefficient, the single scattering albedo and the asymmetry parameter that characterize Z_{11}. The optical properties for gases are taken from the HITRAN database [45] that provides the absorption cross section as a function of temperature and pressure.

Then, the most important part of the program is a ray tracing algorithm. The ray tracing procedure gives an estimation of the integral RTE by drawing samples from the integrals in the Neumann series using random numbers. The scheme results in a Markov chain where only the solution at the previous step is necessary to estimated the following step. Hence, the estimation can be separated in three steps: the sampling of the single scattering albedo, the sampling of the scattering angle and the sampling of the free path length. First, a random number α_1 is generated and if it is greater than the single scattering albedo, the ray of light is absorbed. Otherwise scattering occurs. If this is the case then the scattering angle needs to be estimated. This is done with the so called Henyey-Greenstein phase function (the element Z_{11}) that is the probability distribution for the cosine of the scattering angle $\mu = \cos(\theta)$:

$$Z_{11}^{HG}(\mu) = \frac{1}{2} \frac{1 - g^2}{[1 - g(2\mu - g)]^{\frac{3}{2}}}. \tag{4.57}$$

where g is the asymmetry parameter. Then, the cumulative distribution function (CDF) is

$$
\begin{aligned}
CDF(\mu) &= \frac{1-g^2}{2} \int_{-1}^{\mu} (1 - 2g\mu' + g^2)^{-\frac{3}{2}} d\mu' \\
&= \frac{1-g^2}{2g} \left[(1 - 2g\mu' + g^2)^{-\frac{1}{2}} \right]_{-1}^{\mu}
\end{aligned}
\tag{4.58}
$$

The scattering angle can be sampled generating a second random number α_2 and using the inverse CDF

$$
\mu = CDF^{-1}(\alpha) = \frac{1}{2g} \left[1 + g^2 - \left(\frac{1-g^2}{1 + 2\alpha_2 g - g} \right)^2 \right].
\tag{4.59}
$$

The Henyey-Greenstein phase function is a good approximation for spherical particles thus for Rayleigh scatterers, aerosols and water droplets while for highly non-spherical ice particles an expansion of the phase function on the Legendre polynomials is required in order to describe the many interference structures. In the following we consider only non-spherical particles with a spherical bulk and with deformations on the surface so that the Henyey-Greenstein approximation is valid. The sampling of the free path length of the ray of light is performed in a similar way calculating the probability distribution function as

$$
PDF(j) = \beta_{ext} \exp{(-\beta_{ext} l)}
\tag{4.60}
$$

and the associated CDF

$$
CDF(l_1 < l < l_2) = \int_{l_1}^{l_2} \beta_{ext} \exp{(-\beta_{ext} l)} = [- \exp{(-\beta_{ext} l)}]_{l_1}^{l_2}.
\tag{4.61}
$$

Hence, the free path length can be sampled from a third random number α_3

$$
l(\alpha_3) = -\frac{1}{\beta_{ext}} \ln(\alpha_3).
\tag{4.62}
$$

All the sampling procedure is summarized in Figure 4.12.

In chapter 6, McArtim is used in combination with the Mie code in order to simulate the effect of cirrus on the near-infrared spectrum.
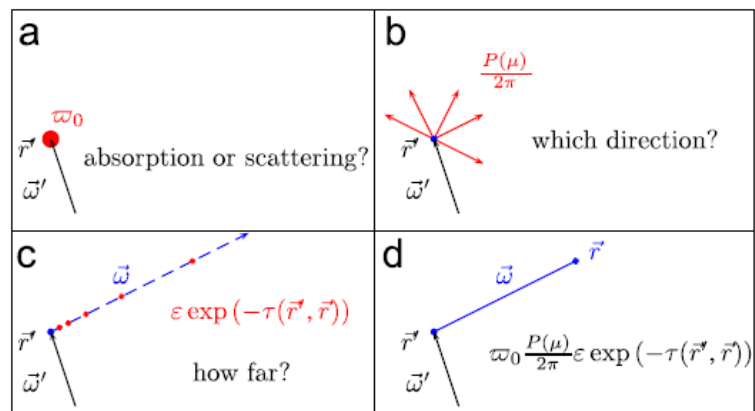
FIGURE 4.12: Sampling procedure through random numbers. Adapted from [44].

Chapter 5

Measurements

In this chapter we describe first the SID instrument and its output measurements i.e., forward scattering intensity patterns. Then, the mini-DOAS instrument is characterized as well as its output measurements in which we are interested i.e., the radiance in NIR. Later in chapter 6, the GDT-matrix simulations are compared with the SID measurements while, the radiance simulated with McArtim is compared with the radiance as collected by the mini-DOAS instrument.

5.1 Single scattering: SID 2D forward scattering patterns

5.1.1 Limitations of the CPI instrument

The evidence of the abundance of small ice crystals in cirrus calls for an instrument capable of resolving particles smaller than 20 μm [13]. The traditional *in situ* instrument called the Cloud Particle Imager (CPI) [46] can produce, under a pulsed laser illumination, real images of cloud particles on a CCD camera [13]. This instrument is really important in providing information about scatterers larger than approximately 25 μm, although below that limit diffraction and optical aberrations render it impossible to resolve the details of the particle shape (see Figure 5.1). To achieve a lower size limit, the Small Ice Detector (SID) was built, making possible to resolve particles with main dimension down to 1 μm just collecting the laser light scattered forward with an azimuthal distribution [12].
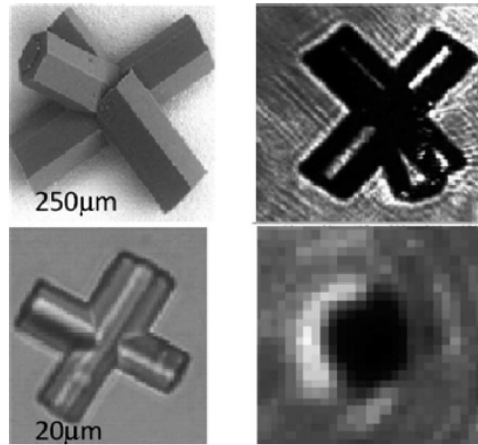
FIGURE 5.1: Images of two crystals obtained by conventional microscopy (left) and the CPI (right). Adapted from [13]

5.1.2 The SID instrument

The SID instrument allows to study the shape, the size, the composition and also the orientation of the particle with respect to the illumination direction. In particular, it is possible to detect the contribution of the particle surface to the scattering pattern [13] making this instrument unique in the attempt to classify the degree of roughness. The SID instrument is designed to detect particles in the range 1-100 μm and it can be mounted on research aircrafts in order to sample real cloud particles. It can measure at a rate of several thousands particles per second making possible to get information about the particle size distribution and also the concentration [12]. The optical technical configuration of the SID is represented in Figure 5.2.

The SID is formed by a 30 mm diameter sampling tube co-axial with the probe centre-line that allows an airflow to enter the instrument. Perpendicular to the tube a circularly polarized 10 mW laser beam is shined at 532 nm wavelength interacting with the particles entering the tube thus scattering the light in all directions [12]. Around the tube there is an assembly of eight optical detectors which receive light scattered from the particles which cross the beam in the vicinity of the tube axis. Each optical detector assembly is composed by lenses, a 532 nm interference filter (to minimize the contribution from ambient daylight), an iris and a miniature photomultiplier detector. Six of the detector assemblies (labeled 1-6) are arranged radially about the axis of the beam and are used in the assessment of particle shape (through interpretation of the scattering pattern). The seventh detector is centered on the beam axis and is used in the evaluation of particle size. The eighth detector is used as a trigger and is really essential because it ensures that only one particle is present in the scattering volume at one time. The scattering
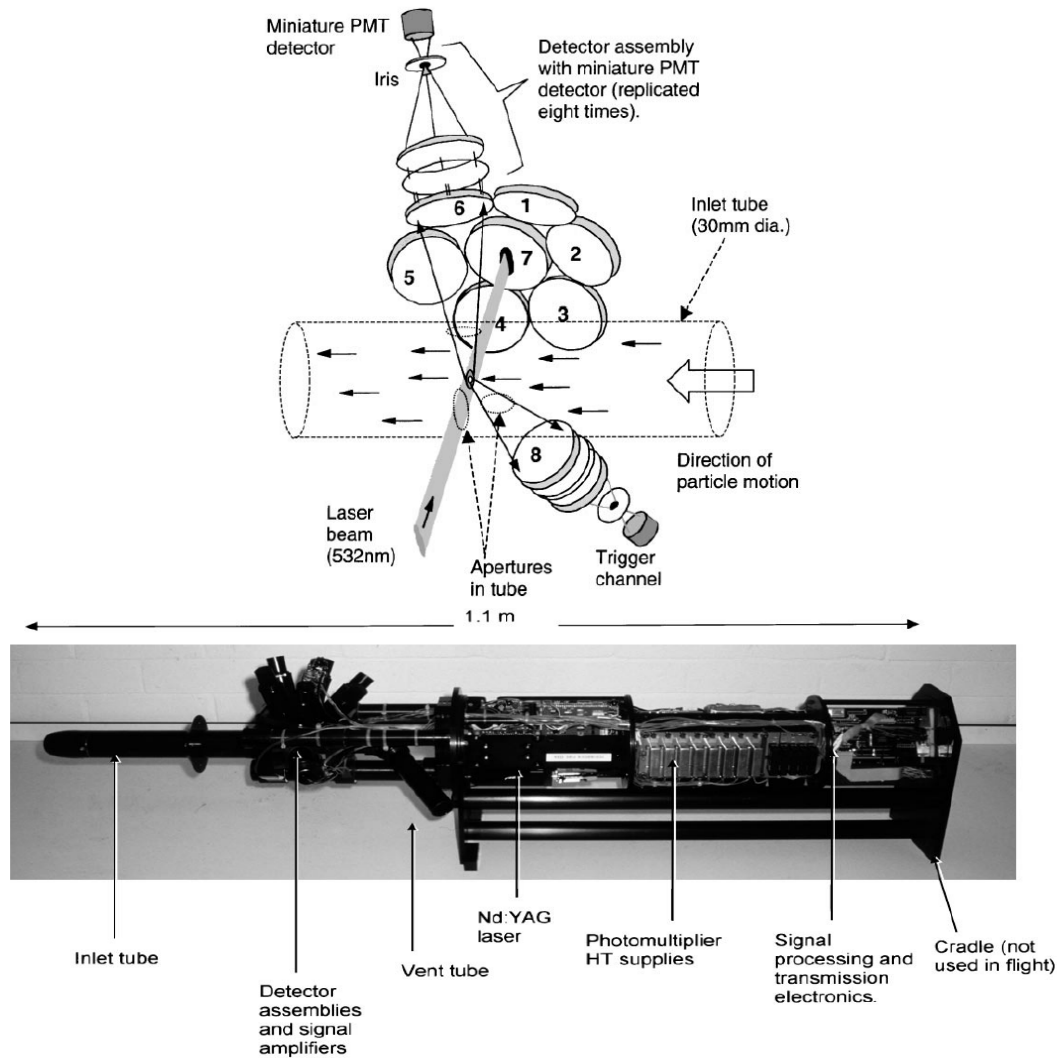
FIGURE 5.2: Upper panel: scheme of the technical arrangement of the optical components in SID. The circular pads 1-7 are detectors used in characterization of the particle size and shape. Detectors 8 and 2 are used in the particle detection and data acquisition triggering processes. Lower panel: a picture of the SID instrument. Adapted from [12]

volume is thus crucial and is defined by the properties of the laser beam and the field-of-view of the detectors. The laser beam at the center of the airflow tube has a width of approximately 4 mm, a depth of 200 μm and a Gaussian intensity profile both parallel and perpendicular to the particle trajectory. Then, detector 8 for triggering, has been optically designed such that its field-of-view form a small elliptical area of 0.35 mm × 0.7 mm that covers the central part of the beam at the axis of the inlet airflow tube. On the other hand, the six azimuthal detector assemblies are designed so that their field-of-view are centered on the same area but are larger, approximately 0.8 mm × 1.6 mm (these detectors are tilted 30° with respect to the beam axis so that the field-of-view in the beam plane are conic sections overlapping completely with that of detector 8). Hence, a particle entering the tube is considered "valid" if it passes through the field-of-view of

the trigger channel (detector 8). Once the trigger is on, the laser is turned on and the scattered light is recorded by the azimuthal detectors. Consequently, a particle passing only through the field-of-view of the azimuthal detectors but outside that of detector 8, will not be recognized as valid. In this way, the probe scattering volume corresponds to an elliptical section of the beam 0.35 mm × 0.7 mm in size and approximately 200 μm depth. Considering an airspeed of 100 ms^{-1}, the air volume flow rate through the scattering volume is approximately 19 mls^{-1}. At a particle concentration of 500 ml^{-1} the particle entering rate is approximately 9500 s^{-1} and the probability of having more than one particle in the scattering volume is 0.47 %. Thus, the probability of wrong data recording is sufficiently small. In Figure 5.3 it is shown how the data are collected on the detectors allowing a mapping of the 2D scattering patterns with particles of different shapes.

Droplet   **Column**   **Complex crystal**
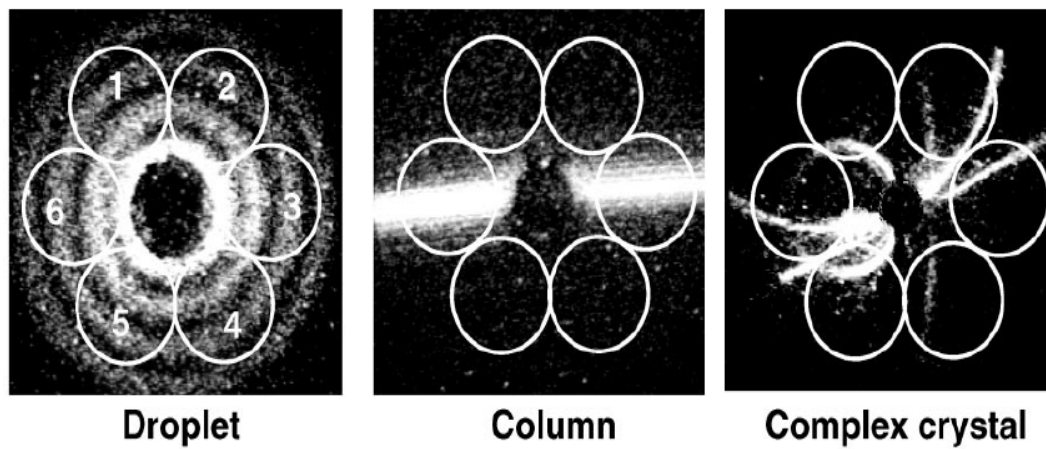
FIGURE 5.3: Diagram illustrating how the scattered intensity from different shaped particles can be measured on the azimuthal detectors giving as output the 2D forward scattering pattern with a zenith angle respect to the incidence direction between 5°-26°. Adapted from [12]

The 2D forward scattering patterns show the intensity of the scattered radiation with a zenith angle with respect to the incident direction in the range of 5°-26°. This is enough to detect the bright halo peak at 22°. We note that for spherical particles such as small droplets, the intensity is equally distributed among the six azimuthal detectors and produces rings. From the number of rings it is possible to retrieve the size of the particle just applying Mie theory. Also for non-spherical particles the angular distribution reflects the main symmetry of the particle as in the columnar case but a direct retrieval of the particle size is not possible. For more complex shapes the interpretation requires detailed calculation in order to retrieve the size and shape of the scatterer (see next chapter).
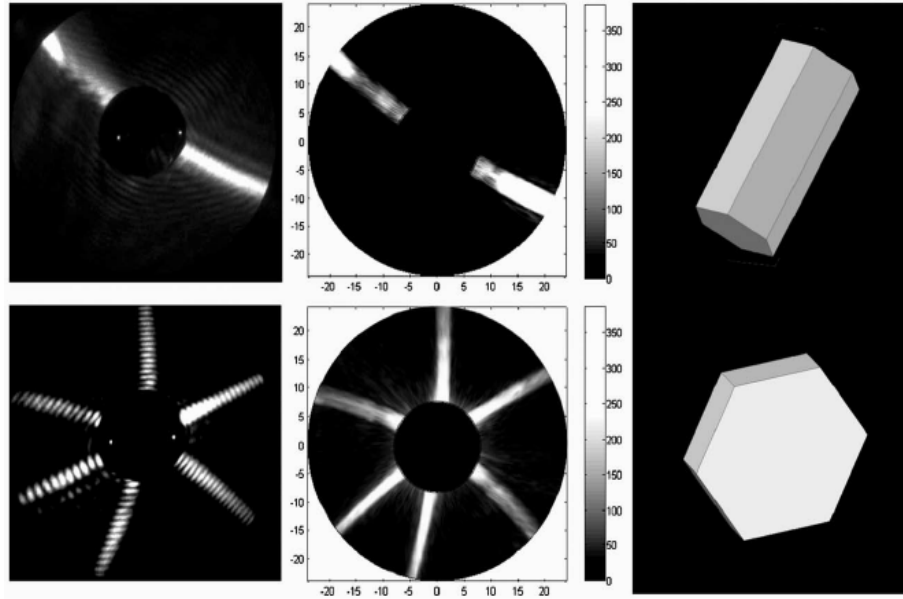
FIGURE 5.4: First column: experimental scattering pattern. Second column: theoretical predictions with RTDF. Last column: the particles used for the simulations. Adapted from [13]

5.1.3 Ice particle SID measurements from the AIDA chamber

Here some results are presented which were recorded with the laboratory version of the SID instrument (PPD-2K), operated by Dr. M. Schnaiter at the Institute for Meteorology and Climate Research, Atmospheric Aerosol Research division (IMK-AAF), of the Karlsruhe Institute of Technology (KIT). The measurements were carried out at the AIDA cloud chamber facility under well-defined laboratory conditions regarding temperature and relative humidity [47]. During a typical cloud chamber experiment around 10000 scattering patterns are recorded by the instrument in the angular range $[7.4°; 25.6°]$. In Figure 5.5 four different particles are shown. First in 5.5a a big hexagonal plate with very smooth faces on the surface is shown where the 6-fold symmetry of the particle is clearly seen. Then, in Figure 5.5c a smaller hexagonal plate but with some rough structures on the surface is presented. In Figure 5.5b an ice column pattern is recognizable with some irregularities on the surface causing some speckle spots in the scattering pattern. As a last example, a droplet is shown where the scattering rings are visible even if they are slightly distorted due to some small deformations of the particle resulting in a departure from a perfect spherical shape.

Patterns of this kind, i.e. with evident regular structures characterizing the symmetry of the bulk of the particle, can be interpreted through theoretical models as the ray tracing and diffraction on facets theory (RTDF [48]). An example is reproduced in Figure 5.4 where the 2D patterns of a columnar particle and of a hexagonal plate are

(A)

(B)

(C)

(D)

(E)

(F)
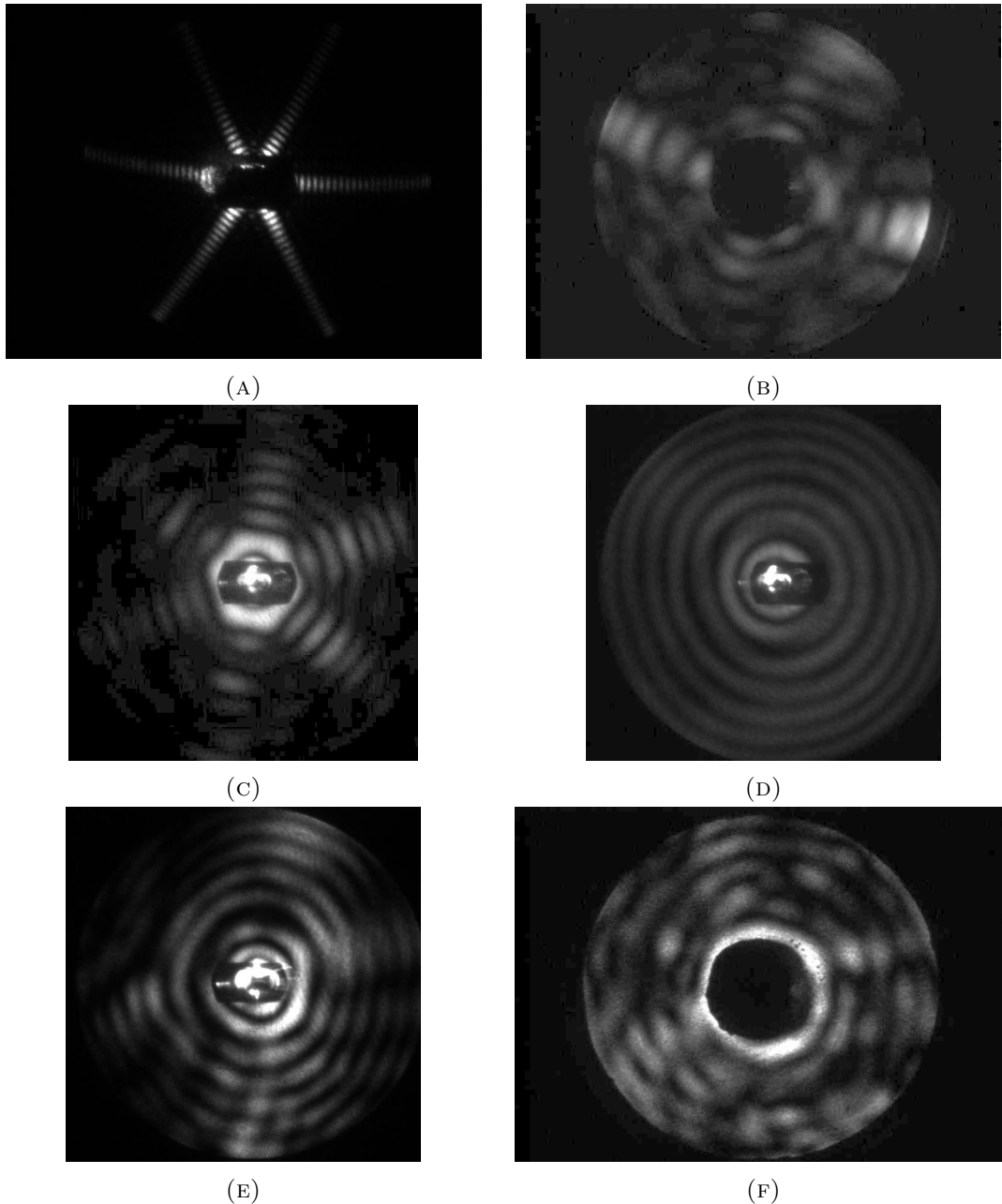
FIGURE 5.5: SID measurements of 2D forward scattering intensity patterns for: (A) a big hexagonal plate (B) a columnar particle (C) a small hexagonal plate (D) a droplet (E) a very irregular ice hexagonal plate (F) an irregular small ice particle.

shown. The same experiment but for a perfect spherical particle results in a 2D pattern with regular rings. However, the RTDF theory can be applied only for very big particles (size parameter of the order of a hundred) where the diffraction theory is justified. In addition, in the context of ray-tracing models, it is impossible to model small scale surface roughness due to the necessity of considering the wave nature of light. This shortcoming really limits the interpretation of measured 2D scattering patterns since the majority of the particles detected during field campaigns are small, rough and very irregular (as reported recently by Ulanowski *et al.* [4] which consider the absence of

the halo intense spot in the 2D patterns for hexagonal columns, that indicates rough surface). Typical patterns for these small and irregular particles are presented in Figure 5.5e and 5.5f.

5.1.4 Ice particle analogues for roughness studies

In the absence of a good model to study big and irregularly shaped particles, Ulanowski *et al.* [10] developed a very interesting strategy in order to interpret the 2D scattering patterns. They produced in the lab ice particle analogues for which they can characterize precisely the state of the particle surface through optical microscopy or SEM. Then, they recorded the scattering patterns and they demonstrated empirically that very irregular speckle patterns are due to small scale roughness on the particle surface. They also measured the phase function and observed the suppression of the 22° halo peak for hexagonal particles and a reduction of the asymmetry parameter in the presence of surface irregularities. These measurements are summarized in Figure 5.6 from [4].
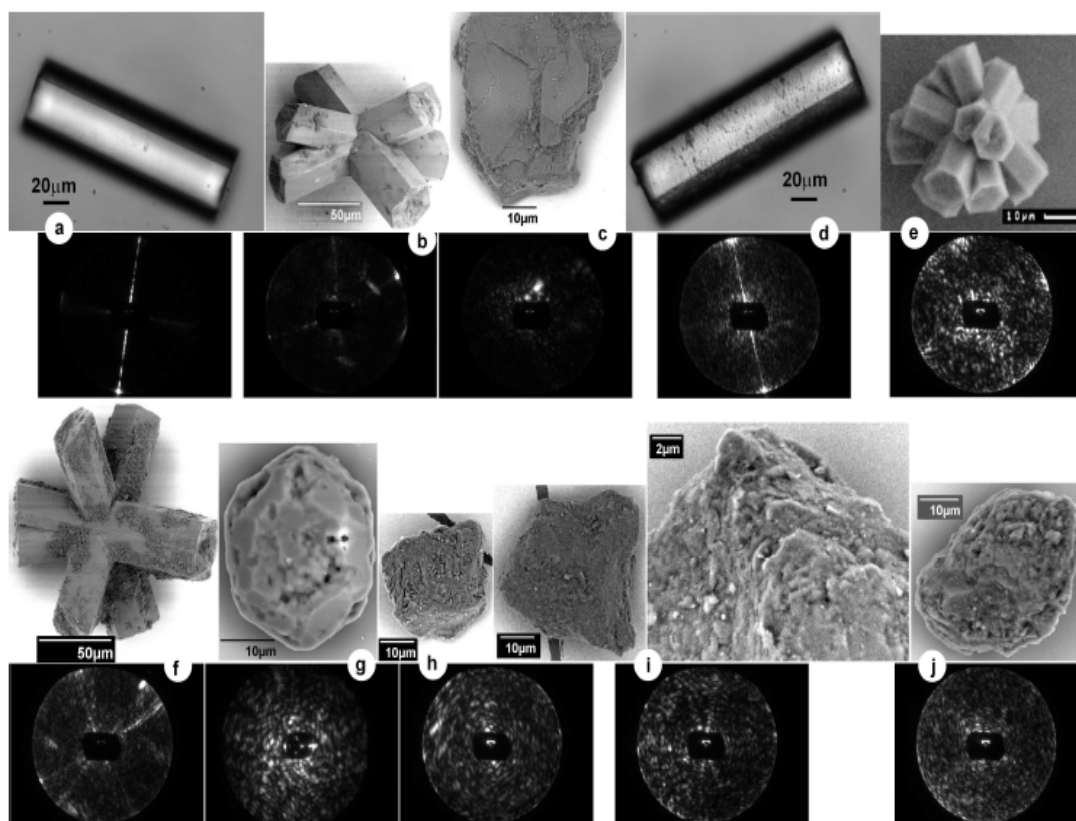
FIGURE 5.6: Upper rows: images of ice particle analogues from optical microscopy and SEM. Lower rows: SID 2D scattering intensity patterns of the particles in the upper rows. Adapted from [4]

It is evident from Figure 5.6 that the surface of the particle plays so important role that can lead to a complete randomization of the scattering pattern erasing also the information about the main symmetry of the scatterer bulk.

In the next chapter we will show how it is possible to use the GDT-matrix method to model small and rough particles. A characterization of particle irregularities is also given in term of a Gaussian random sphere parametrization of the deformations.

5.2 Multiple scattering: Radiance measurements during the NASA-ATTREX mission

5.2.1 The Global Hawk

To fill the gap between mesoscale measurements performed with aircrafts (scale of the order of few hundreds kilometers) and macroscale observations available from satellites (several thousands kilometers) the Global Hawk (GH) unmanned aircraft is used in the frame of the NASA-ATTREX project (Airborne Tropical TRopopause EXperiment [8]). This is a unique aircraft that can fly at high altitudes as 20 km for a maximum of 24 hours making very fast descent and ascent in oder to sample directly *in situ* the cirrus just flying through them. The aircraft has an operative base at the Dryden Flight Research Center in California. The GH has payload compartments where the research instruments can be located (see Figure 5.8).

FIGURE 5.7: The Global Hawk during landing in Dryden. Adapted from [9].

The ensemble of all these instruments provide a unique complete source of information in order to initialize the atmospheric models with the right physical parameters. In the next chapter wel use data from these instruments in order to model and characterize the effect of cirrus on the NIR spectra. In particular, the Cloud Physics Lidar (CPL) and the Hawkeye provide very useful informations required for cirrus simulations. The CPL measures the backscatter signal of three lasers at 355, 532 and 1064 nm. Thus, it can locate the altitude of the cloud and its optical thickness. In addition, it can provide the depolarization at 1064 nm, a measure proportional to the asphericity of the scatterers. The Hawkeye measures the size distribution of the particles within the clouds and combining three existing SPEC optical cloud particle probes can span a size range

between $1\mu m$ and several centimeters. These measurements provide the complete set of information required to simulated the effect of cirrus on NIR radiance. The other instruments provide all the information about the gases, temperature and pressure thus giving a full description of the atmosphere. In the next chapter we show simulations of the radiance in the NIR as measured by the mini-DOAS instrument.
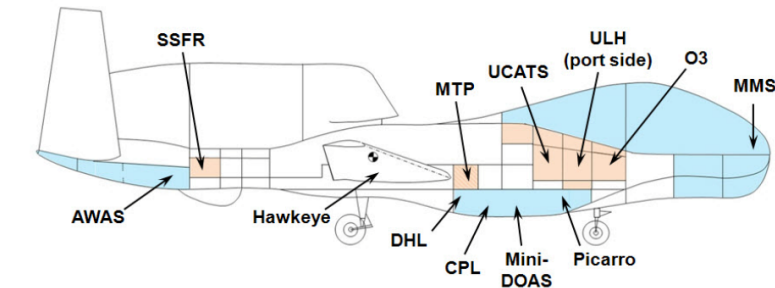
Acronym	Weight (lb)	Power (W)	Measurement	Sampling Rate	Precision	Accuracy
CPL	366		Aerosol/Cloud Backscatter	1 Hz	10-15% backscatter	15-25% extinction
O₃	40	200	O₃	2 Hz	1.5 x 10¹⁰ molecules cm⁻³	5% + precision
AWAS	200	300	~60 tracers with lifetimes of 1 week to years	80 samples per flight	Various, typically 1-10%	Various, typically 2-20%
UCATS	60	250 (450)ᵃ	O₃	10 s	> 1 ppb or 2%	> 2 ppb or 3%
			H₂O	1 s	2-3%	3-5%
			CH₄	140 s	0.4-0.8%	1%
			N₂O	70 s	0.2-0.5%	1%
			CO	140 s	2-5%	1%
			H₂	140 s	2-3%	1%
			CFC-11*	70 s	0.3-0.6%	1%
			CFC-12*	70 s	0.3-0.6%	1%
			Halon-1211*	70 s	0.5-0.8%	1%
			SF₆	70 s	0.2-0.5%	1%
PCRS	45	370	CO₂	5 s	200 ppbv	150 ppbv
			CO	5 min	3 ppbv	15 ppbv
			CH₄	5 s	2 ppbv	1 ppbv
ULH	24	260	H₂O vapor	1-40 Hz	> 0.05 ppmv or 1%	10%
DLH	50	280	H₂O vapor	100 Hz	1% or 50 ppbv	10%
Hawkeye	135	3200	Ice crystal size distributions, habits	1 Hz	20%	50%
SSFR	40		Radiative Fluxes	20 Hz	0.1%	3%
MMS	65	135	Temperature	20 Hz	0.01 K	0.3 K
			Pressure	20 Hz	0.1 mbar	0.3 mbar
			Horizontal wind	20 Hz	0.01 m/s	1 m/s
			Vertical wind	20 Hz	0.01 m/s	0.1 m/s
MTP	24	51	Temperature Profile	1 prof/15 s	<1 K	<0.05 K
Mini-DOAS	33	28	BrO	50 s	0.9 pptv	8%
			O₃		80 ppbv	2%
			NO₂		20 pptv	5%
			OCIO		4.5 pptv	12%
			IO		0.4 pptv	25%
			OIO		0.4 pptv	55%

FIGURE 5.8: Upper part: the Global Hawk payload compartments. Lower part: the instruments onboard the Global Hawk during ATTREX. Adapted from [8].

5.2.2 The mini-DOAS instrument

The mini-DOAS instrument deployed onboard the GH collects the scattered skylight through three movable telescopes oriented 2° off the GH heading. It has been operated by our research group in a collaboration with UCLA (group Prof. Dr. J. Stutz) during the NASA-ATTREX missions from 2011 until 2014. A stable scanning is achieved by automated angle control of the telescopes which compensates for any pitch/roll movement of the GH aircraft. A rectangularly shaped field of view (FOV) of the telescopes (0.19° in the UV and NIR, 0.24° in the visible wavelength range) ensures a good height resolution of the scattering events (see Figure 5.9).
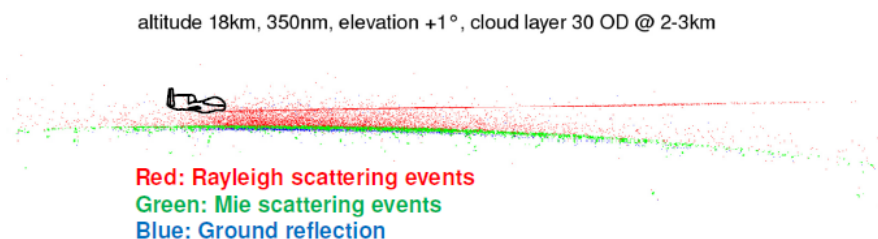
FIGURE 5.9: Simulations of the different types of scattering events contributing to the DOAS-limb measurement in a Rayleigh atmosphere with a 30 optical thickness cloud at an altitude between 2-3 km if the aircraft is flying at 18 km altitude and the telescope is pointing at +1° elevation angle. Adapted from [49].

From the telescopes, the light is collected into three fiber bundles each connected to the corresponding UV/vis/NIR spectrometer. The spectrometers are fixed in an evacuated and water-ice thermo-stated vessel (see Figure 5.10), necessary to obtain a stable optical imaging. This is done to guarantee a low detection sensitivity for the targeted scatterers. A single board computer commands the instrument, handles and stores the data and provides the communication from the ground to the GH.
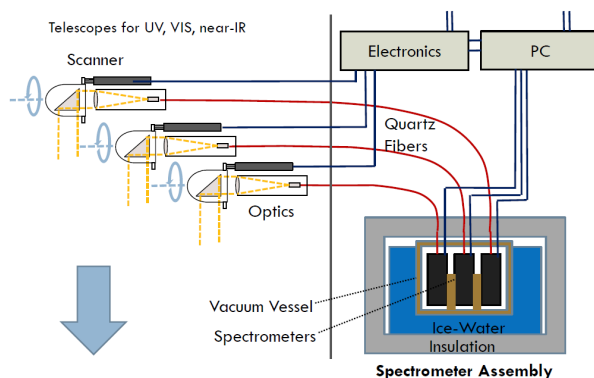
FIGURE 5.10: The mini-DOAS instrument technical scheme.

Thus, it is possible to measure optical spectra (intensity versus wavelength) of the scattered skylight in UV (300-380 nm, FWHM=0.8 nm), visible (410-530 nm, FWHM=0.9 nm) and NIR (900-1700 nm, FWHM=20 nm) wavelengths at different telescope elevation angles $[1°, -15°]$. Differentiating these measurements respect to the clear sky reference, it is possible to retrieve vertical profiles of gaseous species after some radiative transfer modeling within a least-square inversion algorithm [50] (in the limit of weakly absorbing gases). In NIR the atmosphere becomes optically thick (especially in the presence of clouds) and the problem becomes non-linear. Thus, the DOAS approach can not be applied directly because the scattering is dominating over absorption and also due to the broad-band feature of the water (liquid or solid) absorption that is macroscopically described by the imaginary part of the refractive index. More research is required to understand the modifications to be applied to the traditional DOAS scheme. Nevertheless, the measured radiance can be used to qualitatively determine the nature of the particles forming the cloud (see next chapter).
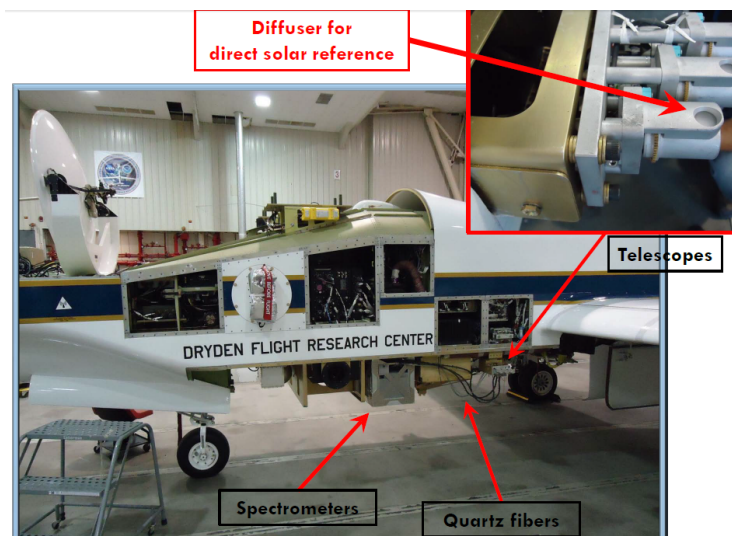
FIGURE 5.11: The mini-DOAS instrument mounted on the GH.

Typical outcomes are summarized in Figure 5.12 where the influence of clouds on the DOAS-measurements is highlighted when the GH is flying above a cirrus cloud (see the CPL map in the same Figure 5.12). In particular, the main outputs of the DOAS-measurement (except from the radiance) are the Slant Column Density (SCD), i.e. the concentration integrated over the line of sight for various gases. The differential SCD or dSCD are the difference between the SCD at some elevation angle and the reference SCD pointing to the sun; this is done in order to remove solar spectral features. We stress here that the presence of clouds shortens the line of sight thus giving an apparent lower concentration for trace gases located below the cloud (as depicted in Figure 5.12 considering the decrease of the O_4 dSCD at the time where the cloud comes in). Thus,

it is important to consider the effect of clouds on the DOAS retrieval procedure. To conclude, we note that the effect of clouds is also evident on the radiance i.e. a peak is present when the telescope points down indicating reflection from the cloud top.
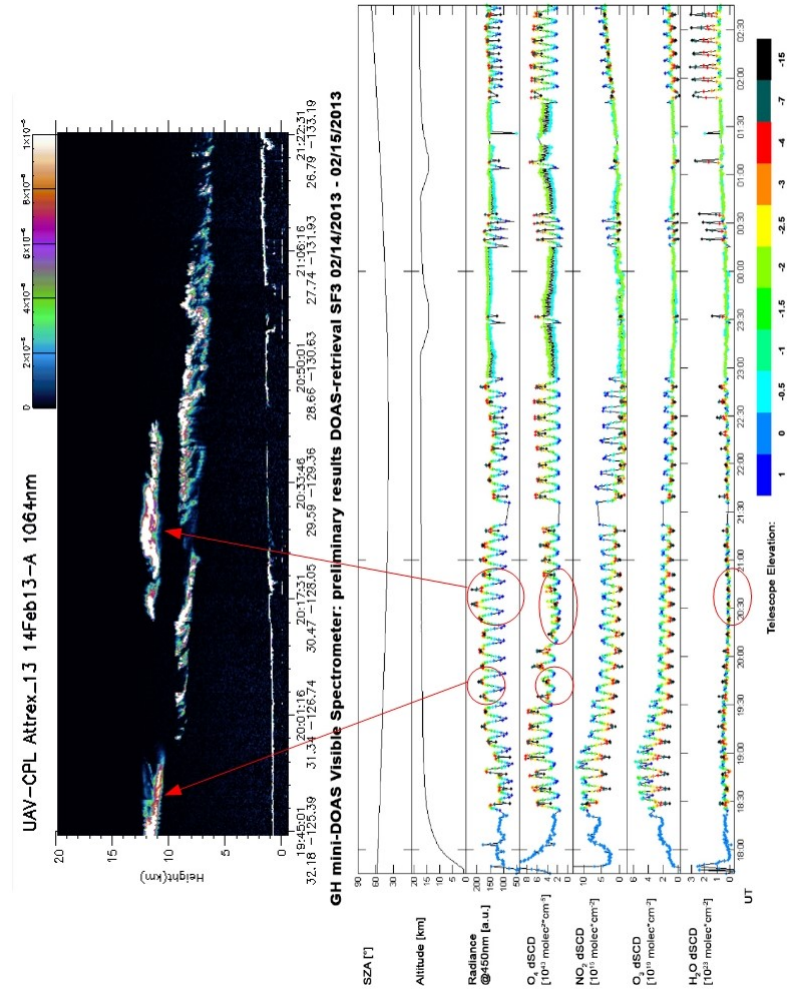
FIGURE 5.12: Upper part: the CPL backscattered intensity at wavelength 1064 nm. Adapted from [51]. Lower part: the solar zenith angle (SZA), the flight altitude, the radiance (at 450 nm) and the DOAS dSCDs for O_4, NO_2, O_3 and water vapour plotted against universal time (UT) measured from the GH in the visible part of the spectrum during science flight 3 (SF3) on 14/02/2013. Adapted from [52]. The color code corresponds to different elevation angless.

5.2.3 NIR mini-DOAS radiance measurements
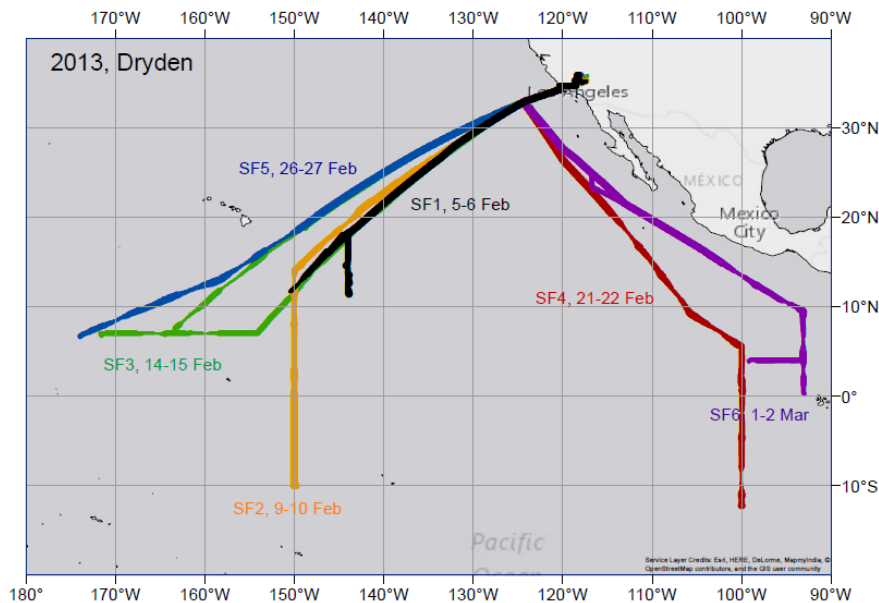
FIGURE 5.13: Flight tracks of the six flights conducted during 2013 leaving from the Dryden Flight Research Center located north from Los Angeles (the thickness of the lines is proportional to the altitude). Adapted from [49].

In this section we consider the NIR radiance measurements conducted with the mini-DOAS instrument onboard the GH during science flight 2 and 3 (SF2 and SF3) based in Dryden at the beginning of 2013. I was participating in the last two flights of the campaign i.e. SF5 between 26-27 of February and the last SF6 between 1-2 of March . Figure 5.13 shows a summary of all the flight tracks that were done in 2013.

A typical spectra in the NIR is shown in Figure 5.14 (upper panel) where a cloudless atmosphere is probed (this can be stated by checking the CPL map at the corresponding time). It is clear from Figure 5.13 that all the flight was above the pacific ocean so great absorption from water vapour is expected. The plot shows the reflectance i.e., the measured radiance normalized to the incoming solar radiation (that was measured directly with a diffuser mounted on each telescope). Part of the spectra has radiances greater than unity just because the measurement is not normalized to the total irradiance penetrating the part of the atmosphere considered, so contribution from scattering e.g. from the ocean surface can lead to values greater than one. Then starting from left, the first two absorption bands and the fourth are due to water vapour, the third is due to O_2 while the last two smaller bands are due to CO_2. We observe that for elevation angles pointing down the contribution of all the absorbers is strong while for the elevations $0°$ and $-1°$ the depth of the absorption profile decrease significantly due to the smaller number of interactions with the absorbing molecules along the light path.
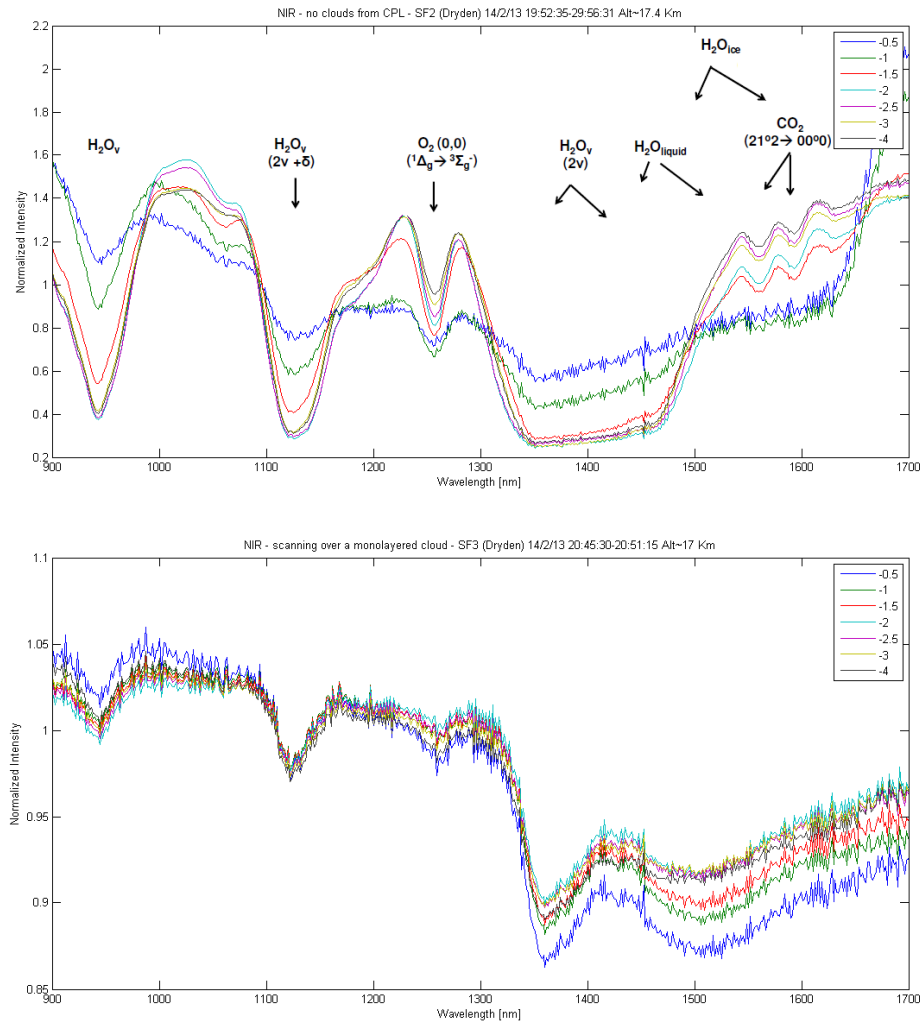
FIGURE 5.14: Measured NIR normalized radiance (intensity) of a cloudless part of SF2 for different elevation angles (upper panel) and of a part of SF3 (lower panel) with a cirrus located between 7-9 km (the physical situation corresponds to Figure 5.12 at the time 20:50:01).

However, this cloud-free situation is very rare in the TTL while most of the flight time is characterized by the presence of different layers of ice clouds (cirrus) and low level marine stratocumulus clouds as shown in the CPL map of Figure 5.12. Basically for all the flights and for all the time there is a cumulus cloud at around 1 km altitude. Then, at higher altitudes between 7-9 km, a first layer of cirrus is encountered. Often, also a second cirrus layer is found at an altitude of approximately 12 km. When a single layer of cirrus is present, the spectra in Figure 5.14 (lower panel) is recorded. Notably, a peak of reflected radiation is found inside the water vapour absorption band between 1300-1500 nm. The high cirrus situation was mostly found during all the 2013 flights. A discussion of these data is presented in chapter 6 where comparisons with modeled radiances are shown and an interpretation of the measurements is proposed.

The complexity of the atmospheric condition is reproduced in Figure 5.15 where a picture of a cirrus as taken by a high definition webcam mounted under the GH is presented.
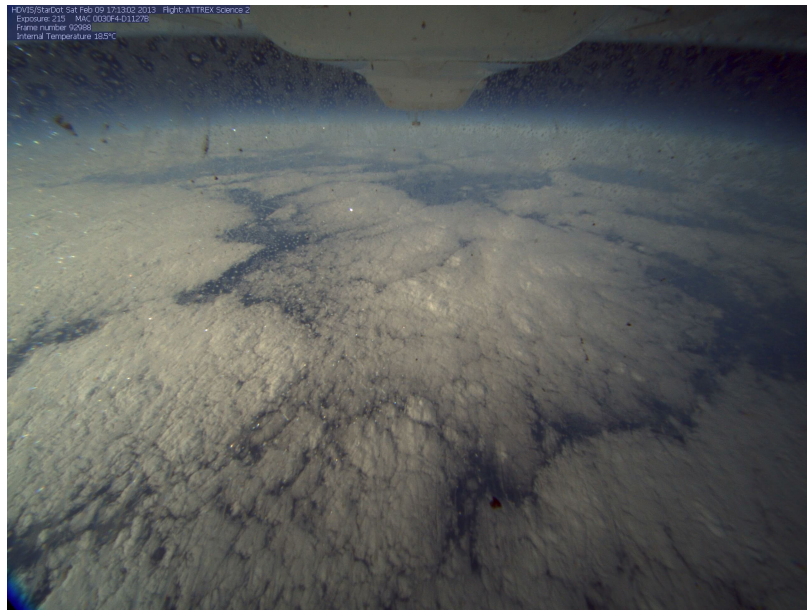
FIGURE 5.15: A webcam picture of a cirrus around 8 km altitude taken from the GH during SF2 at a flight altitude of 17 km.

Chapter 6

Results and discussion

6.1 Single scattering: Simulation of the SID measurements with the GDT-matrix model

We present here some results obtained with the GDT-matrix technique described in chapter 4 in order to give a micro-physical interpretation of the SID 2D forward scattering intensity measurements (more details in Tricoli *et al.* [24]). Here the GDT-matrix is used to calculate the intensity of the scattered radiation in the forward direction for all the azimuthal directions and for zenith angles in the range $[5°, 26°]$ (from the forward direction i.e. the center of the 2D scattering plot). A plane wave is considered as the incident field which is well justified since the scatterer in the SID instrument is located far enough from the laser source. Therefore, in the scattering volume the incoming field can be well described by a plane wave. The direction of incidence is by default the x-axis direction, the wavelength is 532 nm and the incoming plane wave has a circular polarization (in order to minimize the effects connected to the features of the incident field). All particles are assumed to be made of ice [53] for which the dielectric constant at the considered wavelength is $\varepsilon = 1.72 + i2.62 * 10^{-9}$ (only the spherical droplet is assumed to be made of water with $\varepsilon = 1.79 + i4.71 * 10^{-9}$). When we need to calculate the optical properties (e.g. the asymmetry parameter) we set the size limit for simulated particles to x=10 because, for bigger particles the model error exceeds 50%. Instead, when only a qualitative comparison with the SID measurements is necessary we can reach up to a size parameter x=25 (at the price that much more dipoles are needed in order to describe the particle correctly also only in the forward directions). This is possible because in the forward directions the convergence of the GDT-matrix model is good while, in the backward directions it is not good enough. Thus, no calculations of the optical properties is meaningful for size parameters greater than x=10.

6.1.1 GDT-matrix validation with the SID measurements

Some simple, smooth and regular shapes can be used to validate the GDT-matrix model experimentally. We select standard smooth geometries i.e. a cube, a prolate, a sphere and also a slightly irregular sphere to stress the ability of the model to take track of small shape changes [24].
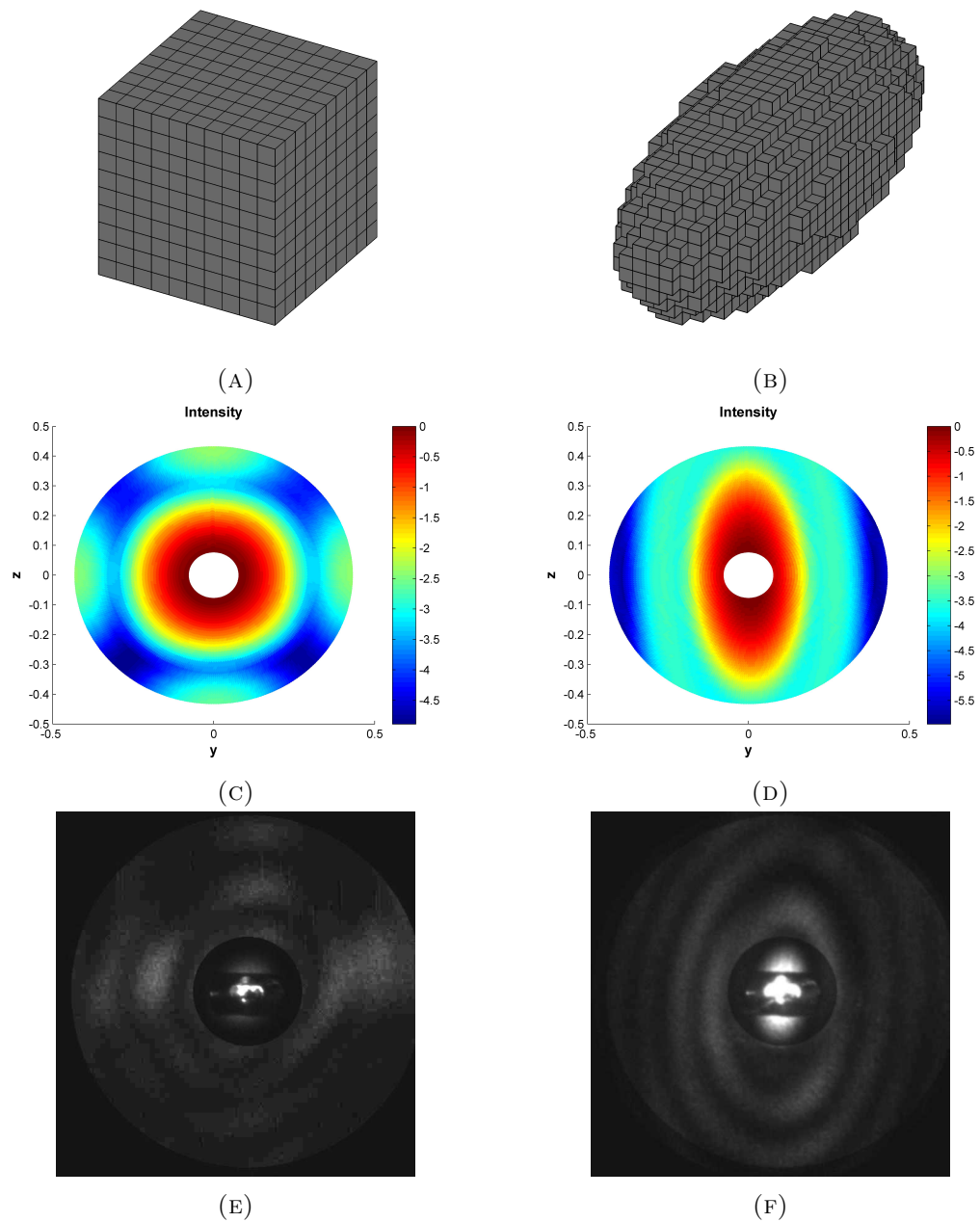
FIGURE 6.1: First row: particle voxelizations. Second row: GDT-matrix simulations of the 2D forward scattering intensity patterns (logarithmic scale normalized to the maximum). The axes indicate Cartesian coordinates on the z-y plane assuming a plane wave traveling along the x-axis. Third row: SID measurements of 2D forward scattering intensity patterns. Adapted from [24].
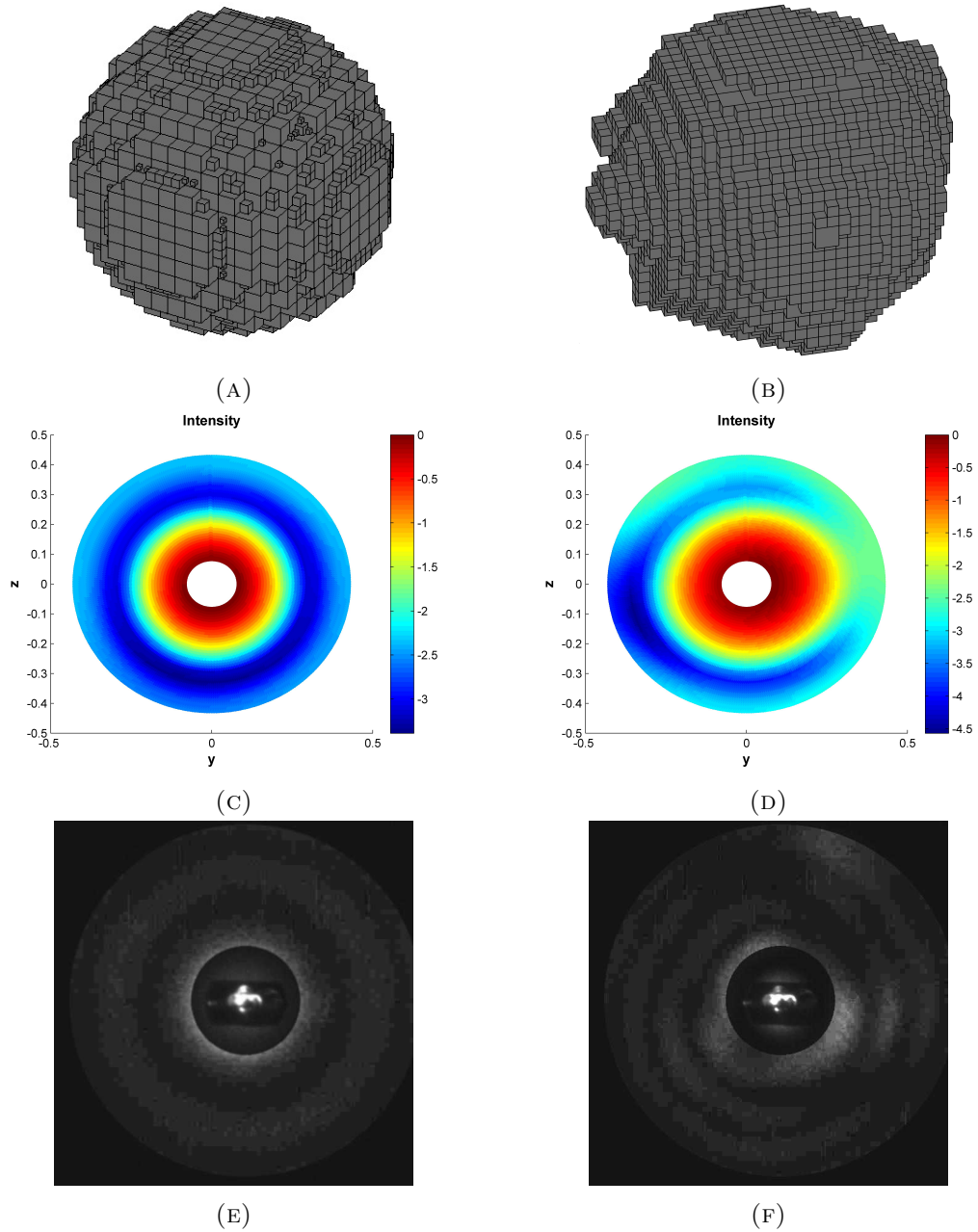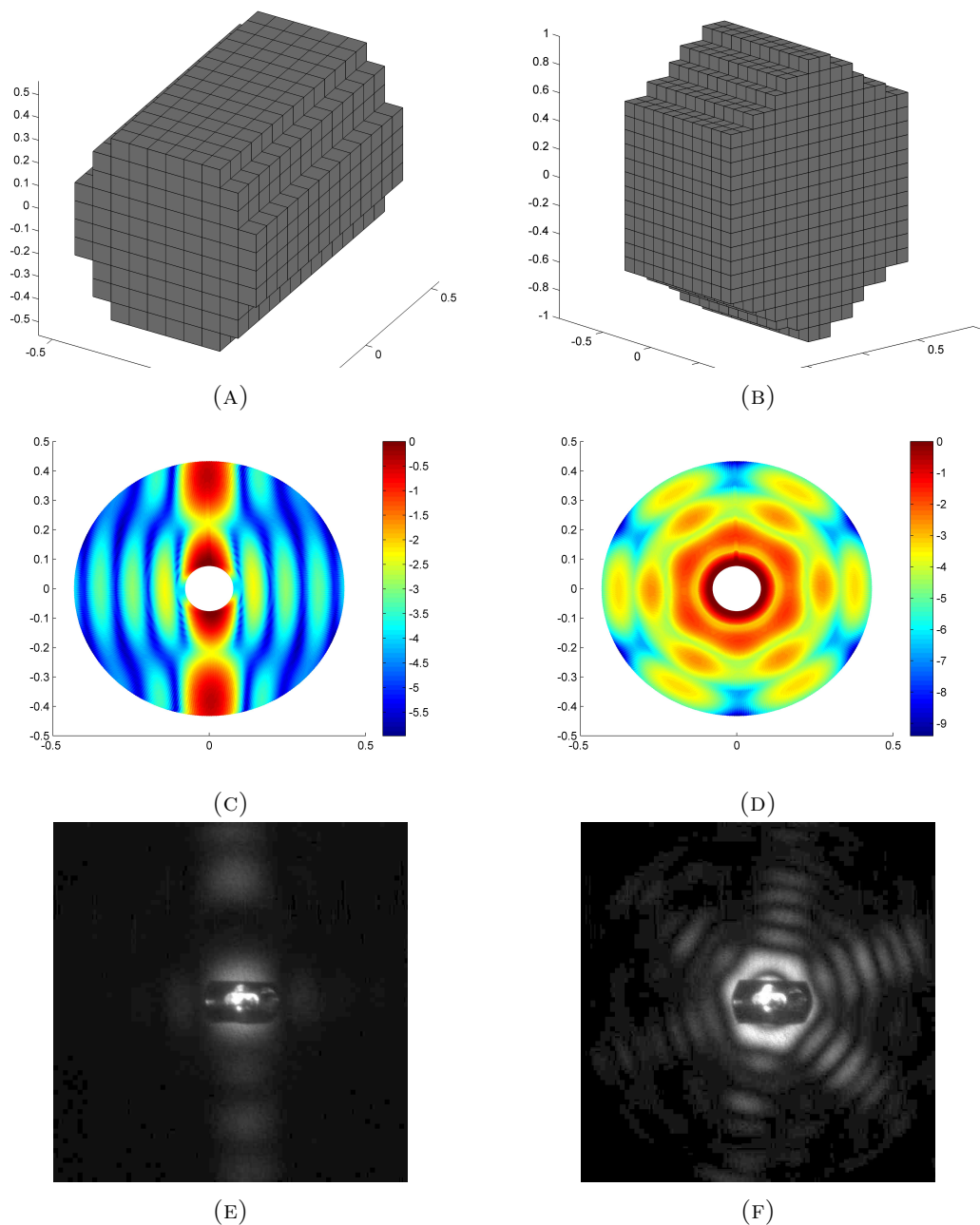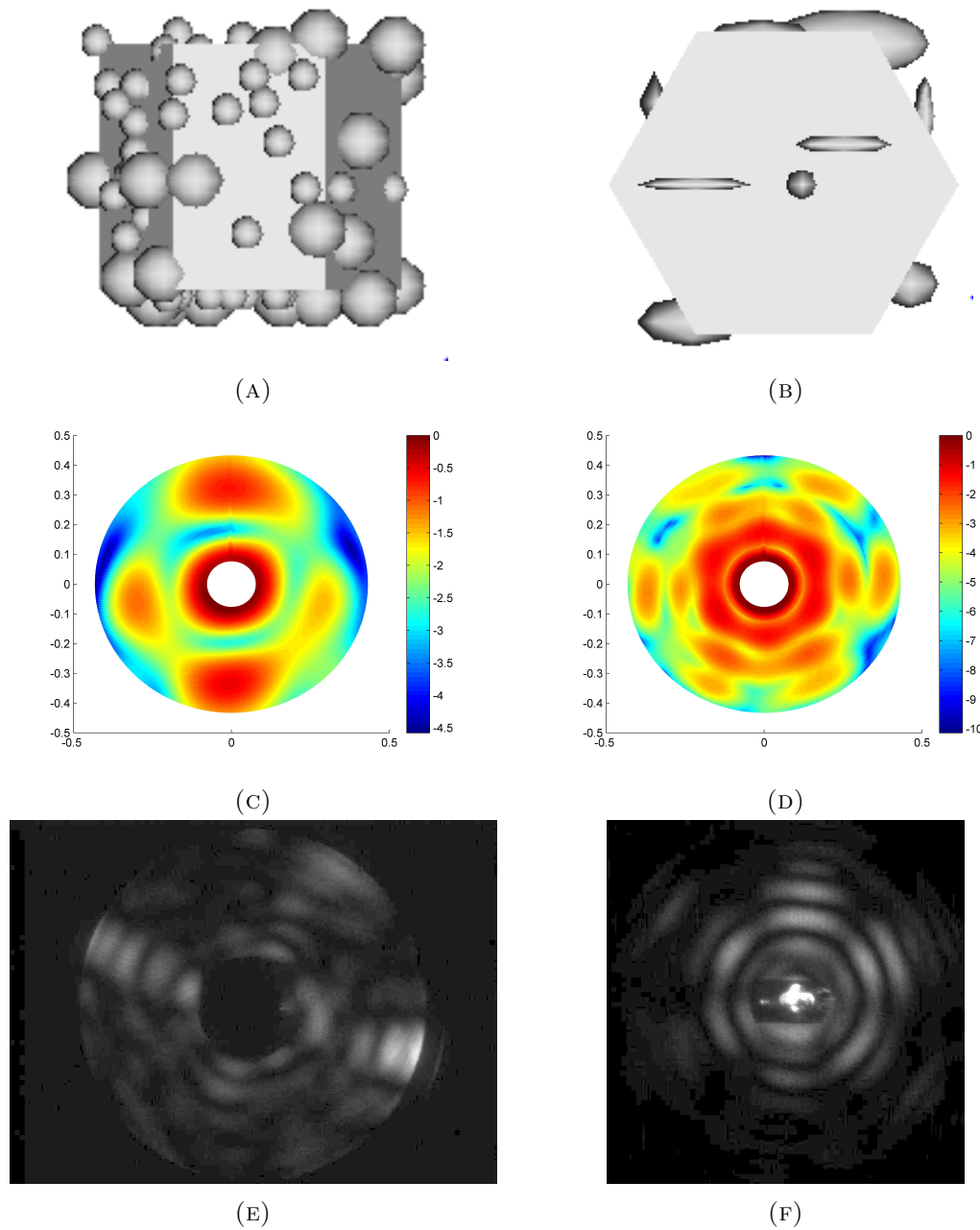
FIGURE 6.2: First row: particle voxelizations. Second row: GDT-matrix simulations of the 2D forward scattering intensity patterns (logarithmic scale normalized to the maximum). The axes indicate Cartesian coordinates on the z-y plane assuming a plane wave traveling along the x-axis. Third row: SID measurements of 2D forward scattering intensity patterns. Adapted from [24].

We note from Figure 6.1 and 6.2 that the GDT-matrix model reproduces well the experimental intensity patterns but with a difference concerning the sizes of the simulated and measured particles. The simulated particles have a size parameter x=10 corresponding to an effective radius (the radius of the equivalent volume sphere) of approximately 1.7 μm. On the other hand the measured effective radius (retrieved by the SID instrument from the intensity of the radiation scattered in the forward direction) is around 4 μm.

Thus, the agreement is only qualitative. However, a larger particle is just producing more intensity maxima as compared to a smaller scatterer. Nevertheless, the overall symmetry of the pattern remains unchanged still allowing a retrieval of the particle shape. In line with this comment, the cubic particle is well simulated by the GDT-matrix model reproducing a clear 4-fold symmetric intensity pattern (the incidence direction is perpendicular to the cube face). Also the scattering pattern of a prolate particle is well calculated with the simulation showing clear elliptical structures around the center. The scattering intensity pattern of a spherical liquid particle is well reproduced in accordance also with Mie theory. Indeed, clearly defined scattering rings appear in the pattern. In addition, for a slightly deformed sphere the model and the measurement indicate broken-up rings due to changes respect to the spherical boundaries. These shape irregularities may occur when a liquid droplet freezes to become solid.

6.1.2 Hexagonal particles

In this subsection we examine the 2D forward scattering intensity patterns of regular hexagonal particles. Figure 6.3 displays a small hexagonal star plate with x=13 which can be distinguished from the most common hexagonal plate of Figure 6.4b. The 6-fold symmetry of the star-like plate is recognizable and can be distinguished from the other 6-fold symmetry of the hexagonal plate.

For a columnar hexagonal particle a bright intensity straight line is present in the forward pattern and tends to be more continuous and thinner as the size parameter is increased (the result shown is for x=16). Some resonance peaks are also present parallel to the main bright line and are not detected in the measured pattern due to low intensity. Then, for the hexagonal plate we show an example for x=25 while the measurement corresponds to a much bigger particle. We observe that the hexagonal plate shape is evident in the central part of the pattern while resonances are present along the hexagonal directions.
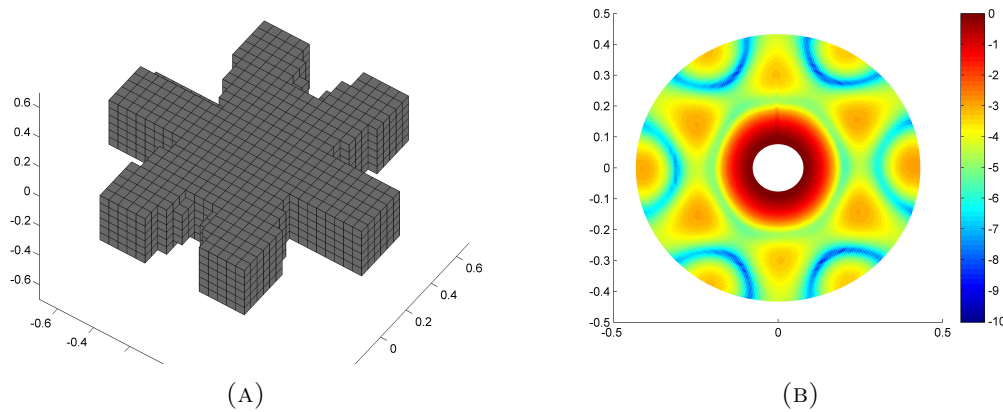
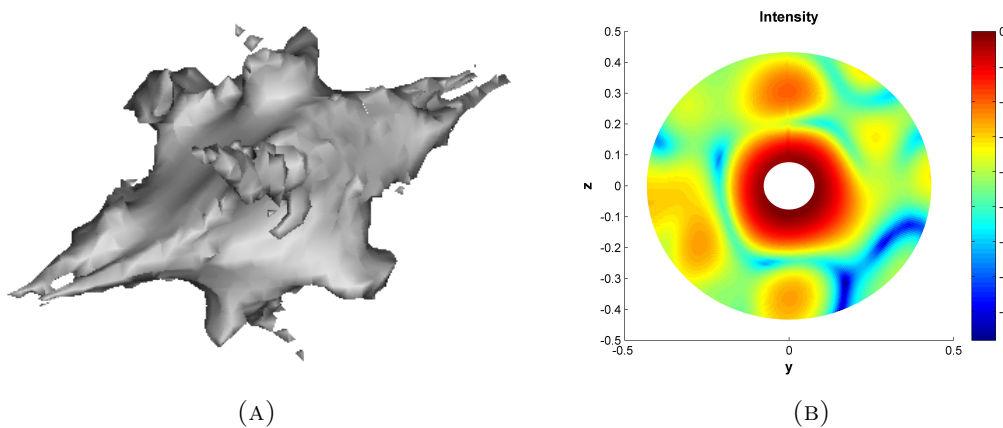FIGURE 6.3: Hexagonal star plate particle voxelization (A) and the GDT-matrix simulation (B) of the 2D forward scattering intensity patterns (logarithmic scale normalized to the maximum). The axes indicate Cartesian coordinates on the z-y plane assuming a plane wave traveling along the x-axis perpendicularly to the star plate face.

The direction of the incident field is perpendicular to the hexagonal faces of the plates and perpendicular to the main axis of the column. We note here that these regular hexagonal particles, responsible for halos, are not frequently encountered with so regular shapes thus potentially explaining the rarity of halos themselves. In the next subsection we model the effect induced by the presence of smaller particles attached to the surface of the main hexagonal bulk thus inducing perturbations to the regular shapes.

FIGURE 6.4: First row: particle voxelizations. Second row: GDT-matrix simulations of the 2D forward scattering intensity patterns (logarithmic scale normalized to the maximum). The axes indicate Cartesian coordinates on the z-y plane assuming a plane wave traveling along the x-axis. Third row: SID measurements of 2D forward scattering intensity patterns.

6.1.3 Deformed particles: Fractals and rimed particles on the surface

Small ice particles can attach themselves to the surface of regularly shaped bigger particles. This can happen when small water droplets turn into rime and stick to the surface of hexagonal columns or plates. An example of this kind of particles is presented in Figure 6.5.

FIGURE 6.5: First row: particle renderings. Second row: GDT-matrix simulations of the 2D forward scattering intensity patterns (logarithmic scale normalized to the maximum). The axes indicate Cartesian coordinates on the z-y plane assuming a plane wave traveling along the x-axis. Third row: SID measurements of 2D forward scattering intensity patterns.

Figures 6.5c and 6.5e show the forward scattering patterns of an irregular hexagonal column (Figure 6.5a) with x=12 in the simulation (bigger one in the measured data). The presence of smaller particles attached to the surface of the hexagonal column can tilt the main bright straight line expected for columnar particles. This effect grows as the particles on the surface tend to accumulate in some particular points destroying the bulk symmetry of the underlying particle. A similar effect is predicted by the model

for a hexagonal plate, Figures 6.5b, 6.5d and 6.5f. In this case the smaller particles on the surface can distort or sometimes erase the resonance peaks along the hexagonal directions. It is also interesting that the central part of the pattern shows an irregular hexagon. These cases are really common in real clouds and they can be detected as in 6.5e and 6.5f typically showing no halo features destroyed by impurities. However, in Figure 6.5e the halo peak at 22° survives the impurities which are just generating a speckle that overlaps with the regular structures connected to the regular bulk shape.

Further, we examine the patterns connected to some very irregular fractal particles created with a Julia-fractal generator (iterating self-consistently complex numbers sum).

(A)   (B)

FIGURE 6.6: Julia-fractal particle rendering (A) and the GDT-matrix simulation (B) of the 2D forward scattering intensity patterns (logarithmic scale normalized to the maximum). The axes indicate Cartesian coordinates on the z-y plane assuming a plane wave traveling along the x-axis perpendicularly to the particle longer dimension.

In Figure 6.6b the pattern has an intensity distribution that reminds the one for a columnar particle since the fractal particle has an elongated shape. However, due to the many irregularities, the pattern shows some speckle interference structures. These speckle spots are manifested when the size parameter approach x=10. This behaviour is demonstrated in Figure 6.7 where we explore the influence of the size of the particle on the related pattern for another fractal particle. Starting with a size x=6 no speckle behaviour appears and a prolate-like pattern is simulated. Then, for x=11 we note the appearance of speckle spots with the center of the pattern still producing a prolate-like structure. When the size parameter is increased further to reach x=25, a predominant speckle pattern is visible. In addition, the size of the speckle spots tend to decrease with an increasing size parameter of the particle, reproducing well observations during field campaigns [4].

Up to this point only qualitative results are presented in order to retrieve the shape of the particles in the presence of irregularities on the surface. A more quantitative study is presented in the next subsections.
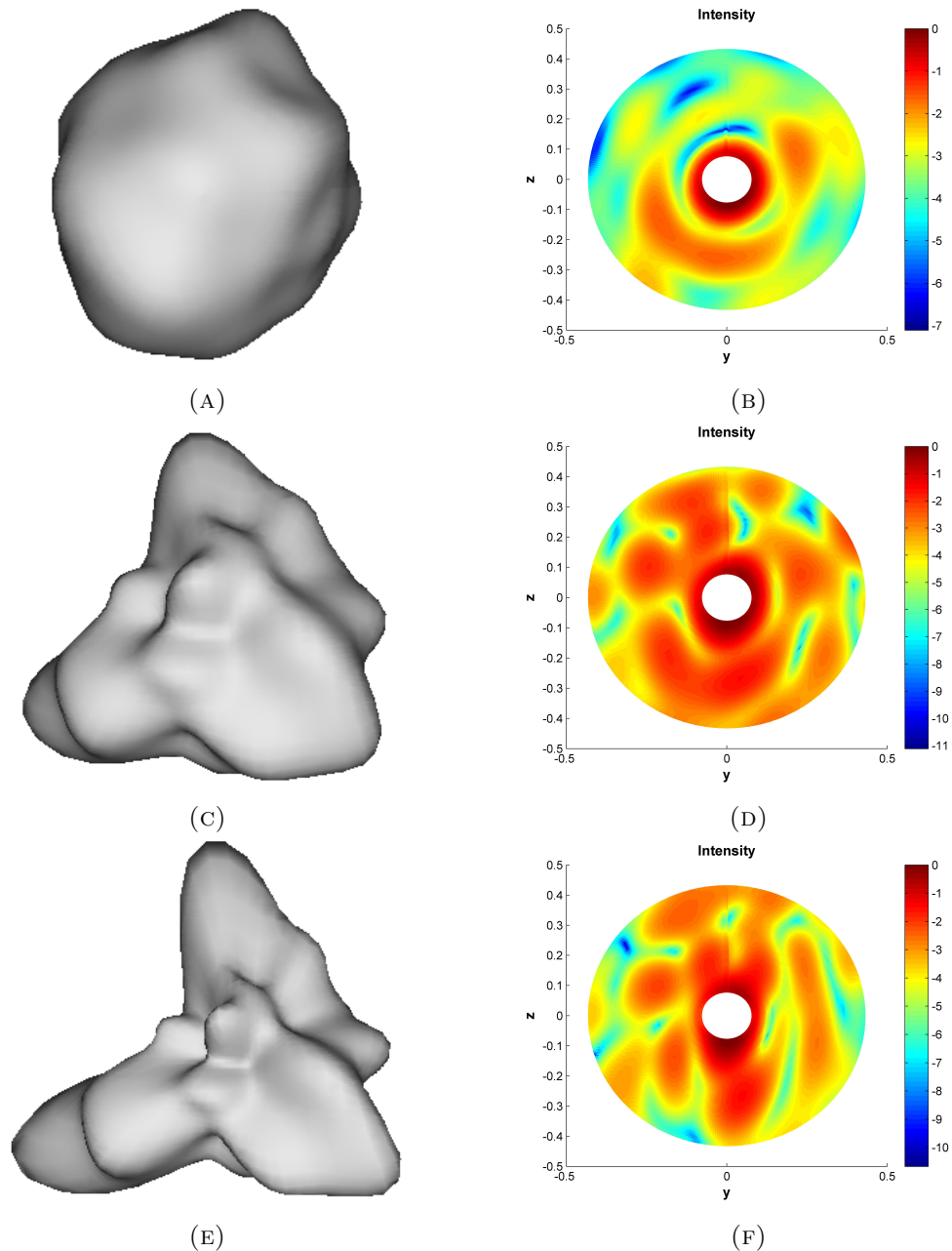
(A)

(B)

(C)

(D)

(E)

(F)
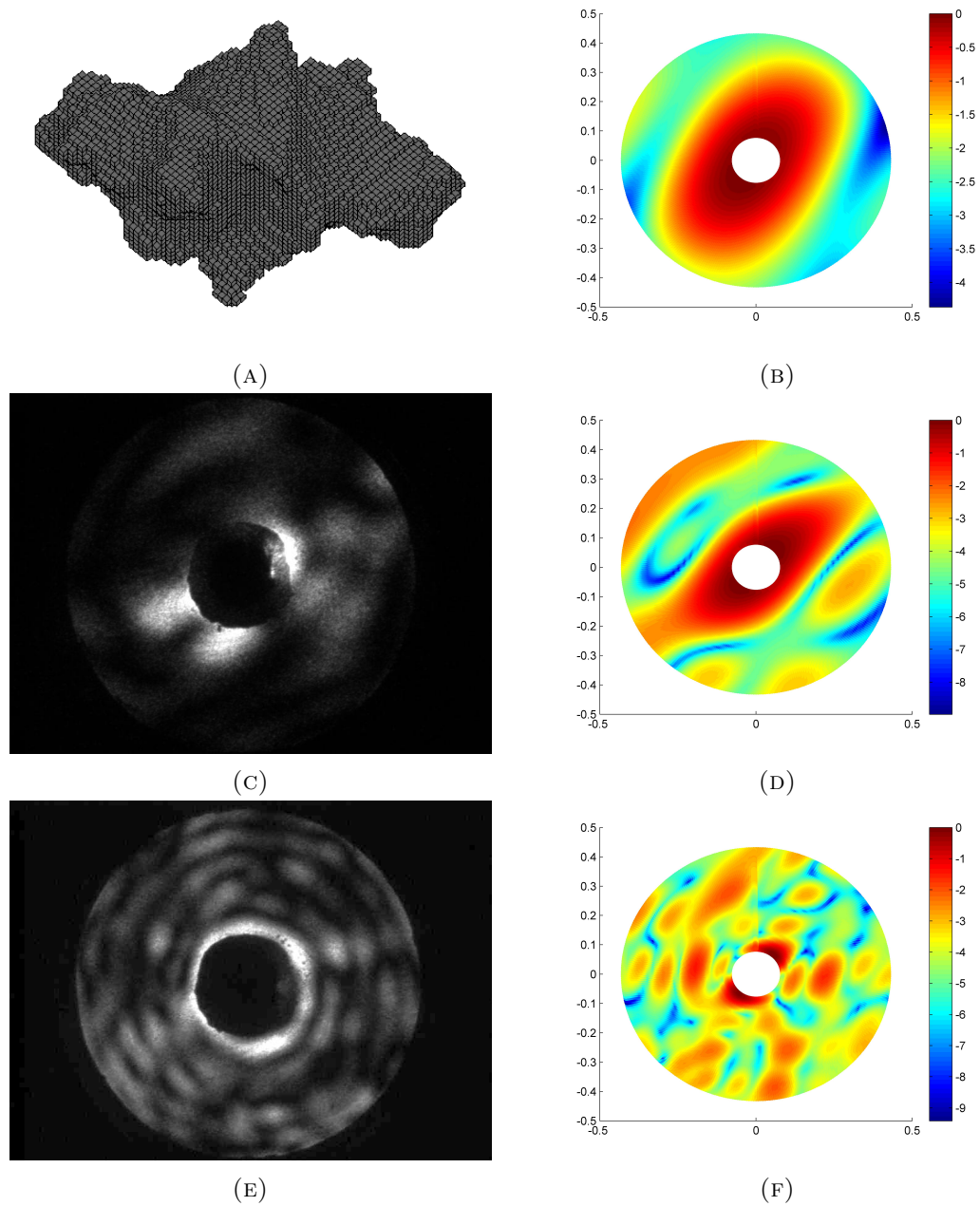
FIGURE 6.7: Study on the influence of the size parameter on the appearance of speckle interference patterns. First column: (A) Julia-fractal particle voxelization, (C) and (E) SID measurements of 2D forward scattering intensity patterns with speckles. Second column: GDT-matrix simulations of the 2D forward scattering intensity patterns (logarithmic scale normalized to the maximum) for a size parameter: (B) x=6 (D) x=11 (F) x=25. The axes indicate Cartesian coordinates on the z-y plane assuming a plane wave traveling along the x-axis.

6.1.4 Deformed spheres: Gaussian random spheres

The Gaussian random sphere model developed by Muinonen *et al.* [16] (see chapter 4 for details) is applied in order to characterize the degree of the deformation applicable

to a spherical particle. The Gaussian random sphere model allows the parametrization of the deformations with a single variable.

(A)

(B)

(C)

(D)

(E)

(F)
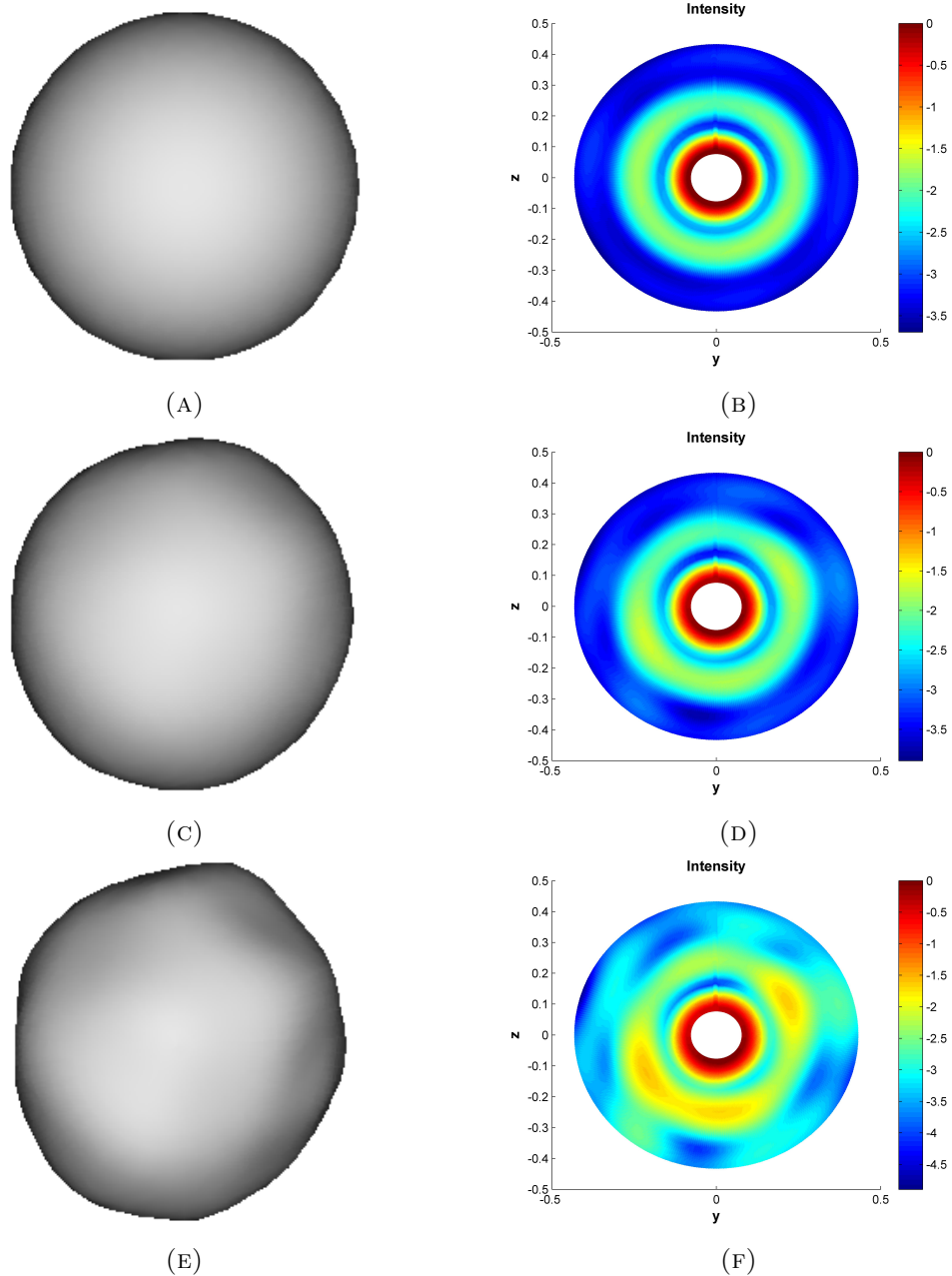
FIGURE 6.8: Study on the influence of the deformation parameter σ on the appearance of speckle interference patterns. First column: Gaussian random spheres rendering for $\sigma = 0.0001, 0.02, 0.05$. Second column: GDT-matrix simulations of the 2D forward scattering intensity patterns (logarithmic scale normalized to the maximum) for a size parameter x=15. The axes indicate Cartesian coordinates on the z-y plane assuming a plane wave traveling along the x-axis.

If we fix the correlation coefficient (among the points on the unit sphere) for the power law correlation to 3 (see chapter 4), the only free parameter left is the standard deviation of the radial distance σ (of a Gaussian distribution). The σ parameter describes the amplitude of the deformations applied to the surface of the unit sphere.

(A)

(B)

(C)

(D)

(E)

(F)

FIGURE 6.9: Study on the influence of the deformation parameter σ on the appearance of speckle interference patterns. First column: Gaussian random spheres rendering for $\sigma = 0.1, 0.3, 0.5$. Second column: GDT-matrix simulations of the 2D forward scattering intensity patterns (logarithmic scale normalized to the maximum) for a size parameter x=15. The axes indicate Cartesian coordinates on the z-y plane assuming a plane wave traveling along the x-axis.

Hence, small σ values correspond to very small deformations while, big values correspond to very irregular shapes ($0 < \sigma < 1$). The effects of small deformations are presented in Figure 6.8. We note that the model is really sensitive to small changes on the boundary of the scatterer. Thus, with very small deformations $\sigma = 0.0001$, the pattern is basically the one for a sphere except some small intensity variations on the second bright ring. Increasing σ, the intensity ring breaks, thus indicating a non-spherical particle.
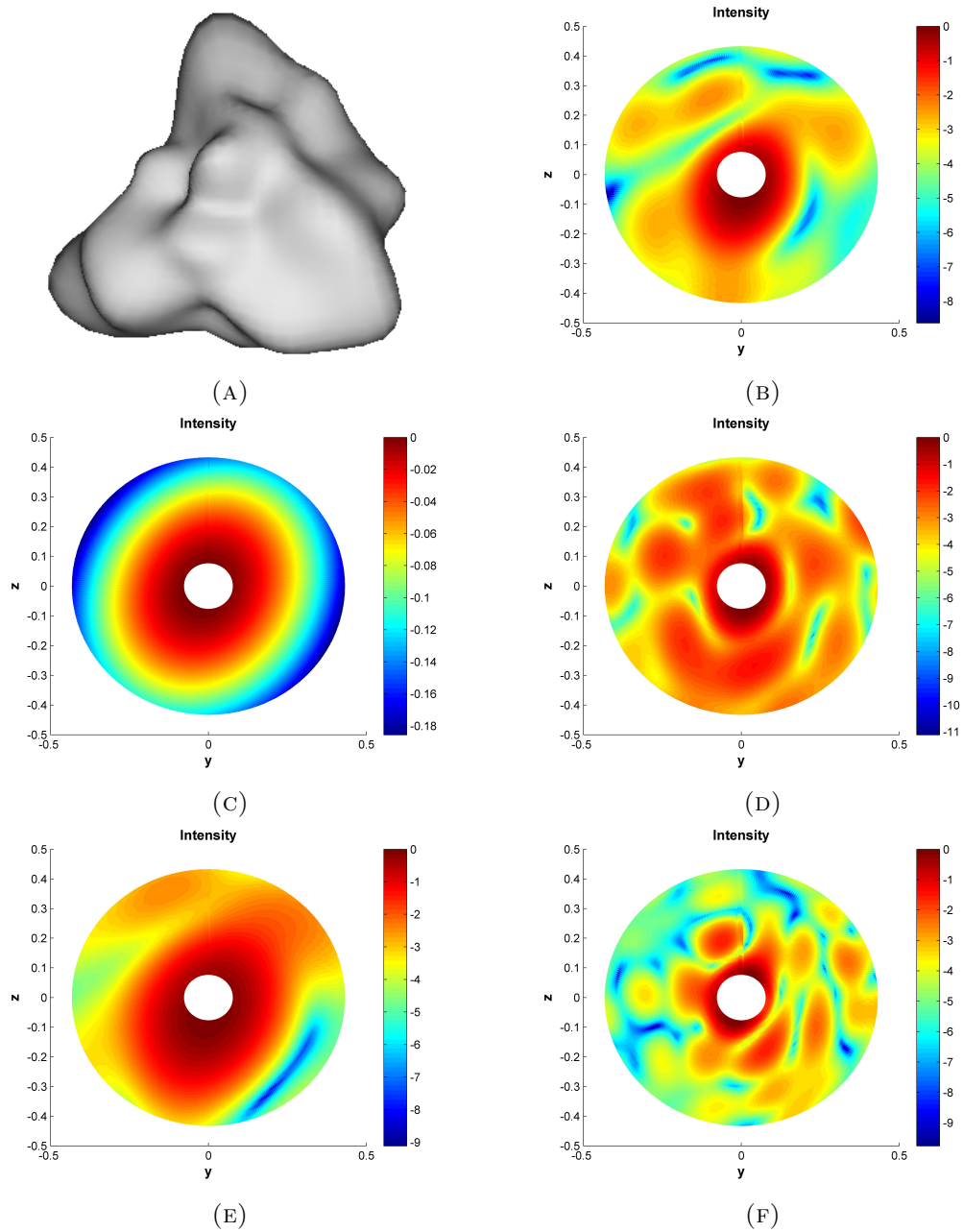
FIGURE 6.10: Study on the influence of the size parameter on the appearance of speckle interference patterns for a Gaussian random sphere with $\sigma = 0.3$. The panels show (A) the particle rendering and GDT-matrix simulations of the 2D forward scattering intensity patterns (logarithmic scale normalized to the maximum) for a size parameter: (C) x=1 (E) x=8 (B) x=11 (D) x=15 (F) x=20. The axes indicate Cartesian coordinates on the z-y plane assuming a plane wave traveling along the x-axis.

Figure 6.9 shows the result when σ is further increased. We see that for $\sigma = 0.1$ the pattern starts to show some speckle behaviour while for larger σ the speckle pattern is clearly established. Thus, we can conclude that when the dimension of the deformations starts to be comparable to the wavelength, the various structures on the surface start to interfere between each other generating a speckle pattern. This is also confirmed by the size parameter dependence of the speckle patterns. In Figure 6.10 we show the

development of the speckle pattern when the size parameter is varied and $\sigma = 0.3$ is kept constant. In particular, an increase in the size parameter induces a reduction of the dimension of the speckle spot. This is true also in the case of a varying σ at a fixed size parameter, as already demonstrated. Hence, it is in principle possible to retrieve the standard deviation of the deformations of a Gaussian random sphere, once the size parameter is fixed, varying the σ up to the point where the mean size of the speckle spots in the model fits the one measured. The information about the size parameter can be obtained with the SID instrument by measuring the intensity scattered in the forward direction (after a proper calibration of the SID instrument, see [12]). In particular, the Gaussian random sphere model seems appropriate to describe the objects of Figure 5.6 (last two rows) where no clear sign of the bulk symmetry of the particle (no straight bright line or hexagonal shape) is visible in the scattering intensity patterns, suggesting a deformed spherical scatterer as it is also confirmed by the complete knowledge of the particle brought by the use of particle analogues [10].

6.1.5 Rough particles

In order to consider the effects of small scale surface roughness, we perturb the smooth surface of a hexagonal plate by eliminating a certain percentage of the dipoles lying on the surface. This is done in a sparse-octree discretization scheme by selecting the last two levels of the voxel hierarchy. Then, the dipoles to be eliminated are selected with a random number generator. In Figure 6.11 two cases are studied and compared to the smooth case for a size parameter x=15. In the first case, 33% of the surface dipoles are removed. It is possible to see that the main hexagonal shape in the scattering intensity pattern becomes discontinuous and eventually is broken for the second case with surface roughness of 50%. Notably no speckle structure appears, indicating that the size of the perturbations is much smaller than the wavelength. Thus, overall the symmetry of the bulk is preserved and the geometry of the scattering intensity pattern is just distorted, rendering still possible a retrieval of the shape.
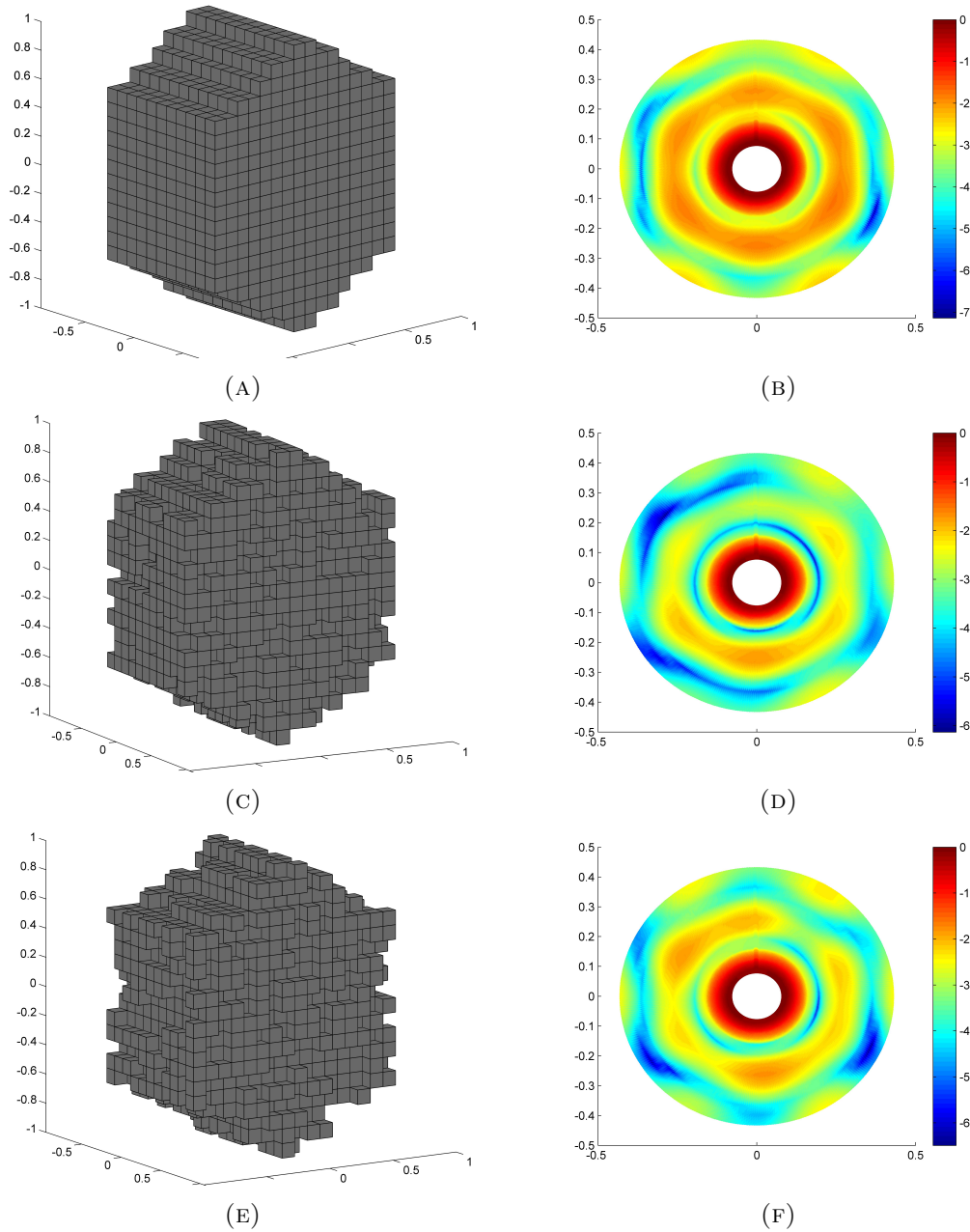
FIGURE 6.11: Study on the influence of the surface roughness on 2D forward scattering intensity patterns. First column: (A) smooth hexagonal plate (C) rough hexagonal plate (33% surface dipoles removed) (E) rough hexagonal plate (50% surface dipoles removed). Second column: GDT-matrix simulations of the 2D forward scattering intensity patterns (logarithmic scale normalized to the maximum) for a size parameter x=15. The axes indicate Cartesian coordinates on the z-y plane assuming a plane wave traveling along the x-axis.

6.1.6 Influence of the deformations on the optical properties

The effect of deformations or surface roughness is visible also on the optical properties (see the chapter 4 for definitions). We observe no significant change in the extinction coefficient with respect to the corresponding smooth particle. Some changes are observed

for the single scattering albedo although the behaviour is complex and does not relate in a simple way to the shape, size parameter or the amplitude of the deformations of the particle. On the contrary, the asymmetry parameter g, shows a clear decreasing trend when the amplitude of the deformation is increased. This is demonstrated for small particles x=3 and x=5 in Table 6.1. Within the GDT-matrix scheme, the value of g for irregular particles is reduced with respect to the smooth particles. The increase of g for $\sigma = 0.3$ and $\sigma = 0.5$ with respect to g for $\sigma = 0.1$, is due to the fact that the particle with larger values of σ departs heavily from a sphere thus giving a less isotropic scattered radiation i.e. a larger value for g. Hence, a small deformation of the spherical particle can lead to a consistent decrease of the asymmetry parameter. This is caused by the fact that the backscattering part of the phase function is enlarged when the particle has an irregular shape as shown in Figure 6.12. This behaviour is relevant for radiance simulations studied in the next section.

TABLE 6.1: Asymmetry parameter (g) dependence on σ

particle type	x	σ	g	g-reduction %
smooth	3	0	0.785	0
deformed	3	0.02	0.694	11.6
deformed	3	0.1	0.716	8.9
deformed	3	0.3	0.759	3.3
deformed	3	0.5	0.76	3.2
smooth	5	0	0.852	0
deformed	5	0.02	0.817	4.2
deformed	5	0.1	0.812	4.7
deformed	5	0.3	0.837	1.8
deformed	5	0.5	0.836	1.9

Then, repeating the same study for the rough particles considered in the previous subsection but for x=6 we obtain the results exposed in Table 6.2. Thus, the small scale surface roughness has little influence on small particles respect to surface deformation.

TABLE 6.2: Asymmetry parameter (g) dependence on surface roughness

particle type	x	roughness %	g	g-reduction %
smooth	6	0	0.915	0
rough	6	33	0.914	0.05
rough	6	50	0.913	0.24

In conclusion, the study on the influence of deformations and roughness on the optical properties is limited to small particles. Indeed, the GDT-matrix error for the calculated scattered field increases rapidly with the size parameter thus, only supporting simulations of particles up to x=10.
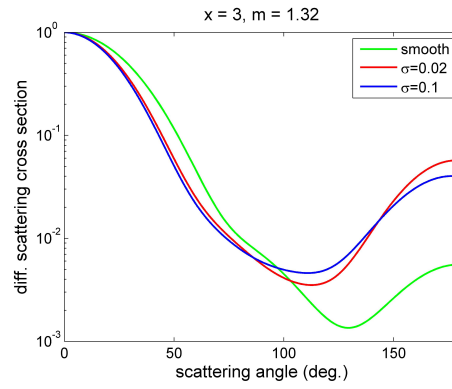
FIGURE 6.12: Phase functions for ice particles with x=3 and spherical shape (green), deformed spherical shape with $\sigma = 0.02$ (red), deformed spherical shape with $\sigma = 0.1$ (blue).

6.1.7 Inhomogeneous particles: Inclusion of air bubbles

Air bubbles are common inside the bulk of ice particles and their presence depends on the type and speed of the ice core nucleation [54].
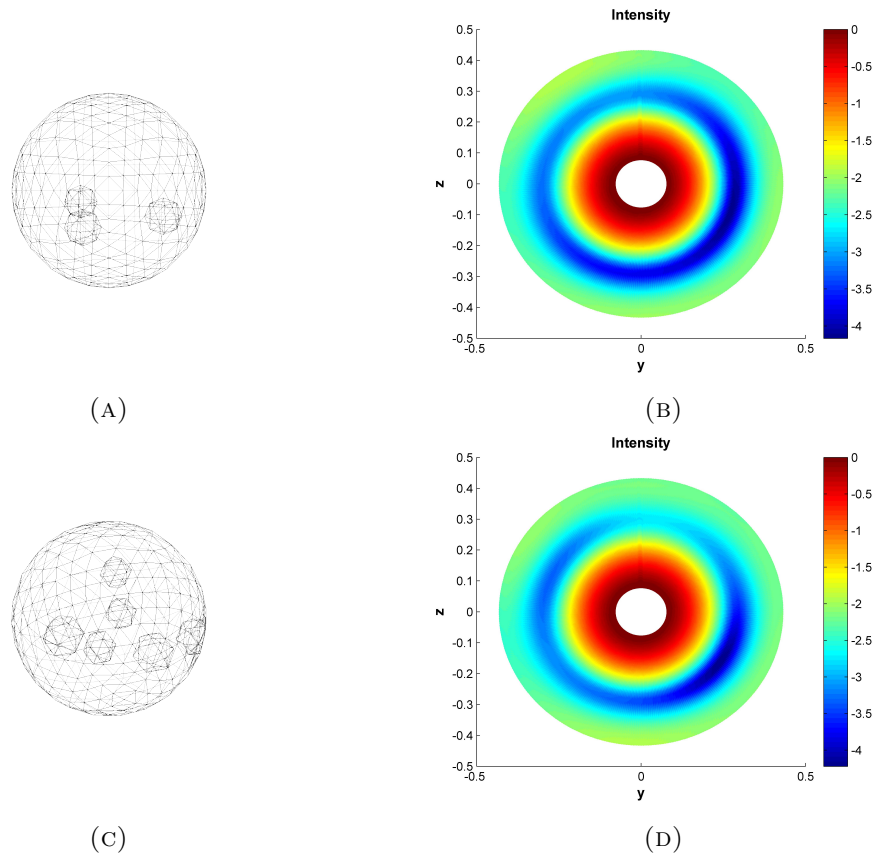
FIGURE 6.13: First column: rendering of a sphere with: (A) 3 spherical sub-volume inhomogeneities (C) 6 spherical sub-volume inhomogeneities. Second column: the 2D forward scattering intensity patterns (logarithmic scale normalized to the maximum). The axes indicate Cartesian coordinates on the z-y plane assuming a plane wave traveling along the x-axis.

Hence, we study the 2D forward scattering patterns for inhomogeneous particles. We consider only a spherical ice particle of size x=10 with some randomly located smaller spherical bubbles with x=1.5 inside, Figures 6.13a and 6.13c. We note that the patterns show a spherical central intense part justified by the spherical boundaries, while the outer intensity rings are modulated in intensity but preserving a circular shape. Notably, the first scattering intensity ring is not distorted as in the case of deformed spheres and no speckle is manifested.

6.2 Multiple scattering: NIR radiance simulation in the presence of clouds

In this section results from radiance simulations with the radiative transfer model McArtim are shown. In order to evaluate the influence of cirrus on the NIR spectra, comparisons with radiance measurements (already introduced in the last section of chapter 5) are presented. In particular, we use results of the previous section to evaluate the effect on the spectra caused by small deformed spherical ice particles. Small deformed spherical ice particles are characterized by a lower value of the asymmetry parameter, as indicated by the GDT-matrix model. On the contrary, the other optical properties are little influenced by the shape departure from a perfect sphere and can thus be calculated with the Mie code for spherical scatterers.

6.2.1 Gaseous atmosphere

In the simulations, only a gaseous atmosphere is first considered. McArtim necessitates as input the temperature and pressure profiles (read from the MTP instrument onboard the GH). Then, the absorption cross sections for the different gases are obtained from the publicly available database called HITRAN [45] already contained in McArtim (while the scattering is of Rayleigh type). To complete the description of the gases, their vertical distribution (profile) is needed and can be obtained from global models just giving the geo-location. For oxygen and carbon dioxide the distribution is well known while, for water vapour, an accurate profile can be extrapolated from NOAA measurements onboard the GH. The remaining ingredient is the incoming solar irradiance I_0 for which we use the Thuillier [55] measurement at the top of the atmosphere (that corresponds to a Planck distribution at 5800 K with some absorption structures due to the solar photosphere). Test results for an assumed flight altitude of 10 km with the telescope pointing nadir, are shown in Figure 6.14. The absorption contributions of the single gases relevant in NIR are first plotted to facilitate their identification in the cumulative plot, the last. Note that a CO_2 absorption line is present inside the large water vapour absorption band between 1350 nm and 1500nm. In order to simulate the spectra recorded by the DOAS instrument onboard the GH, the altitude and geo-location of the plane are needed and taken by the GH flight-track database.

6.2.2 Clouds and cirrus influence on the NIR spectrum

First, we calculate the NIR spectra in the presence of a cloud and discuss some of the implications for the measurements.

(A)

(B)

(C)

(D)
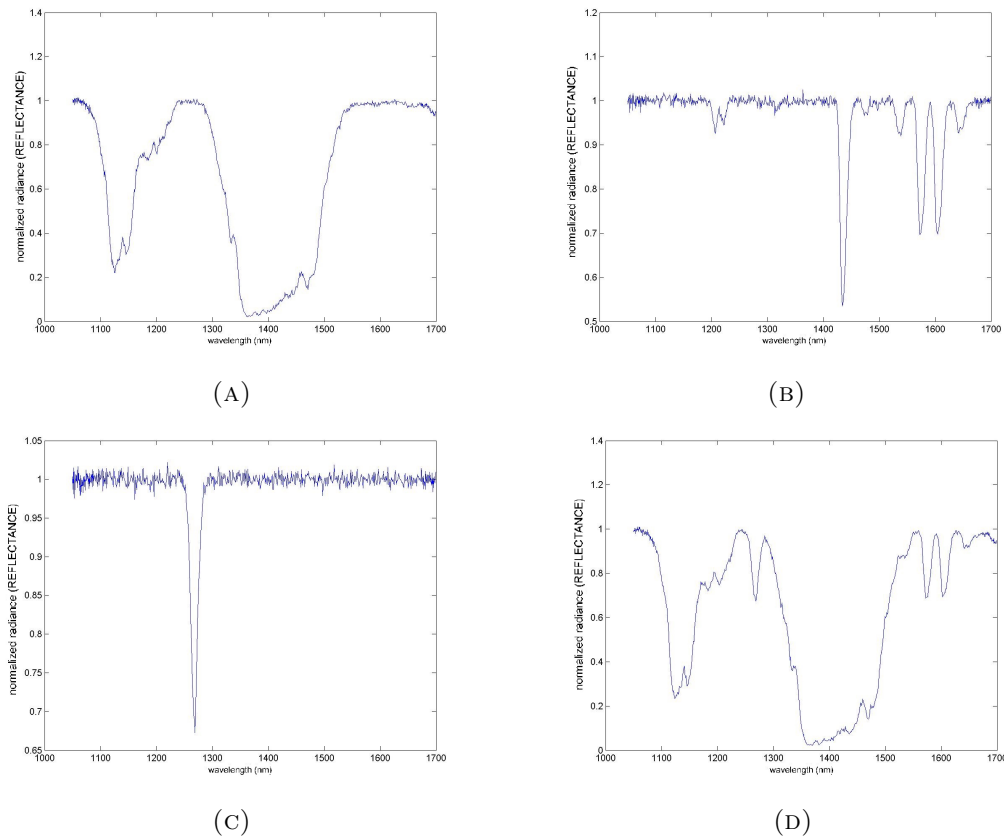
FIGURE 6.14: Normalized radiance simulation for an atmosphere containing: (A) only water vapour (B) only carbon dioxide (C) only oxygen (D) all the three gases.

The relevant parameter for cloud particles is the refractive index i.e. the optical property that controls the scattering (real part) and the absorption (imaginary part) of the incoming radiation. This is also important to distinguish the contribution from liquid and solid water particles. In particular, only the imaginary part of the refractive index of liquid water and ice differs in the NIR, showing a shift of 50 nm in the absorption of ice (1500 nm) with respect to liquid water (1450 nm), see Figure 6.15. However, both liquid and icy particles decrease the intensity of the spectra after 1500 nm due to the tales of the imaginary part of the refractive index. The gases absorption cross sections are also plotted in Figure 6.15 for those species contributing more in the NIR i.e. water vapour, oxygen and carbon dioxide (already considered in Figure 6.14).

In addition, the altitude and geometrical thickness of the cloud are required in the simulation. A multiplication of the geometrical thickness of the cloud with its bulk extinction coefficient gives the optical thickness of the cloud τ (see chapter 4). These informations are read from the CPL data (see Figure 6.18) and allow to define the vertical structure of the cloud optical properties as a profile. After a grid is defined, a table is generated with the lines corresponding to the altitude level and the columns to the bulk extinction coefficient, the asymmetry parameter and the single scattering albedo respectively. Due
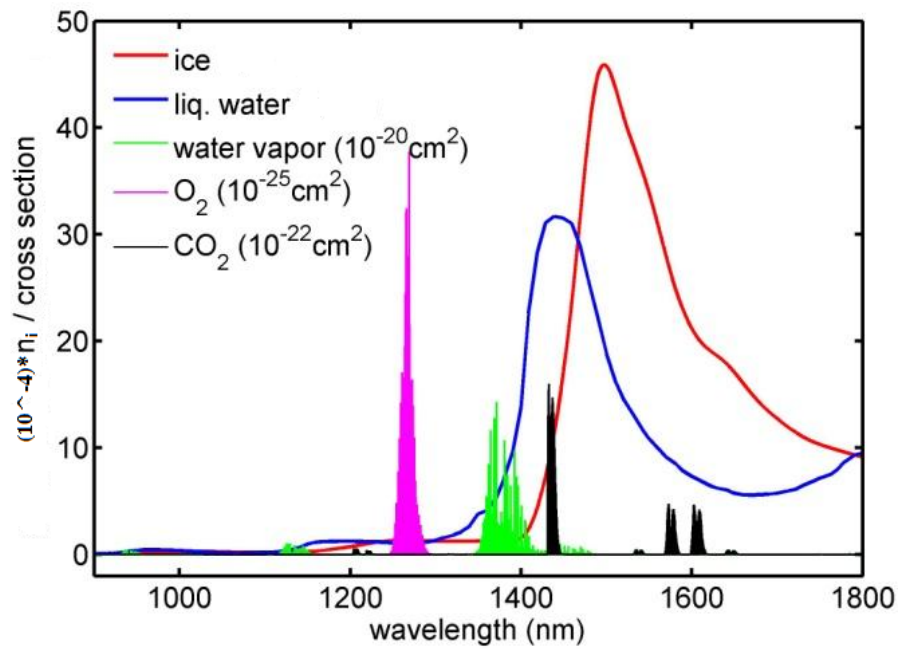
FIGURE 6.15: Imaginary part of the refractive index of ice and liquid water and absorption cross sections of water vapour, oxygen, carbon dioxide molecular gases as a function of wavelength. The data for gases are taken from the HITRAN database [45] while for water from [56] and for ice from [53].

to the lack of particle measurements characterizing the optical properties over the entire NIR wavelength range, it is necessary to calculate with a model the optical properties of a distribution of particles as a function of the wavelength. The Mie code introduced in chapter 4 is used with the refractive index as a function of the wavelength as input (Figure 6.15). This choice is dictated by the necessity of fast computation because then the calculation needs to be repeated for around a thousand wavelengths. In addition,
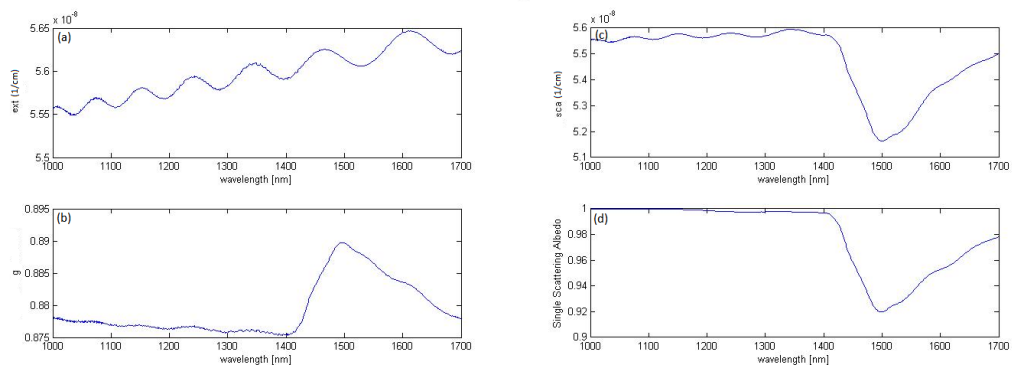
FIGURE 6.16: Optical properties (as a function of wavelength) of ice particles calculated with Mie theory averaged over a log-normal size distribution with median value $R_m = 57$ μm, logarithmic of the standard deviation equal to 2 and number density $N_0 = 0.02$ cm^{-3}; (a) the bulk extinction coefficient (b) the asymmetry parameter g (c) the scattering coefficient (d) the single scattering albedo.

in the Mie code there is no need for particle orientation averaging and the integration over the size-distribution can be done very efficiently. The same is not true for the GDT-matrix code. For ice particles we select a log-normal size distribution with a median radius of $57\mu m$ as recorded by the Hawkeye instrument (for liquid water optical properties see chapter 4). Then, we calculate the optical properties averaged over the size distribution i.e. the bulk extinction coefficient, the single-scattering albedo and the asymmetry parameter (Figure 6.16). The optical properties are then read by the radiative transfer solver McArtim as a function of the wavelength. The main approximation is thus that we consider ice particles as spheres. This is a brute approximation when the crystals tend to be very large (median radius of the order of hundreds of micron) and so the relative humidity. However, for all the flights the Hawkeye *in-situ* instrument recorded the shape of the particles showing that the majority of the particles are nearly spherical in the bulk even if with some deformations and irregularities on the surface (see Figure 6.17). We show at the end of this section how it is possible to treat "effectively" the real irregular particles using results from the previous section obtained with the GDT-matrix.
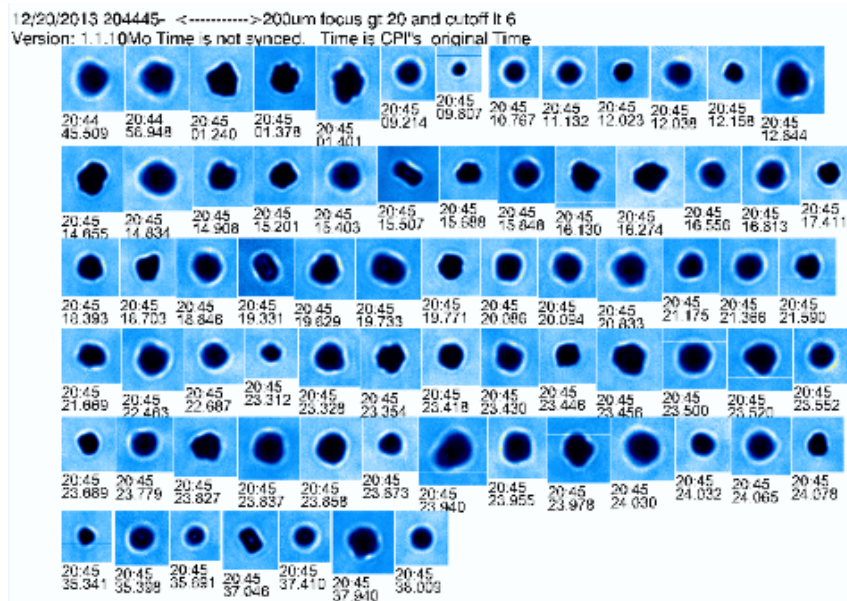
FIGURE 6.17: Images of ice particles as recorded by the Cloud Particle Imager (CPI) on board the GH. Adapted from [9].

All simulations consider the aircraft at 17 km altitude (with the telescope pointing down with an elevation angle of $-4°$) and a water vapour concentration of 60% (except one case where it is explicitly mentioned). The first simulation, Figure 6.19a, considers only the effect of a liquid water cloud at 7-9 km altitude (with different values of the optical thickness) and of water vapour. The optical thickness is increased (also to extreme values as $\tau = 1200$) in order to see the effect of the liquid cloud on the NIR spectrum.
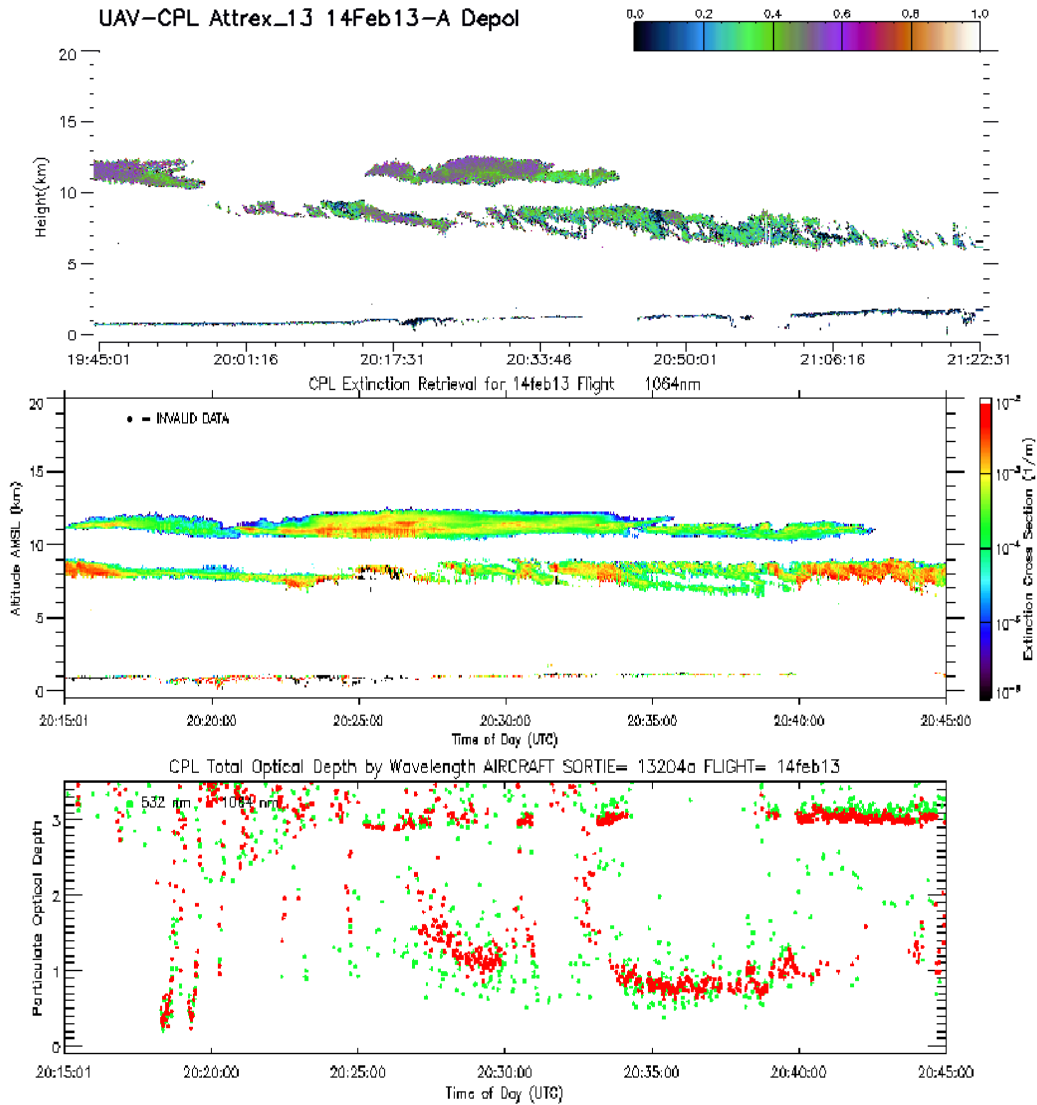
FIGURE 6.18: Cloud Physics Lidar (CPL) output data showing the location of the cloud as a function of the altitude, vertical axis, and time, horizontal axis. First panel: the depolarization (colours). Middle panel: the extinction coeffient (colours). Last panel: the optical thickness at 532 nm (green) and at 1064 nm (red). Adapted from [51].

It is possible to observe that at the right side of the water vapour band the slope of the normalized intensity line is modified by the presence of the cloud. It is also important that no reflectance peak is present inside the water vapour band for wavelengths greater than 1400 nm. In addition, increasing the optical thickness (increasing the number density), the longer wavelength part of the spectrum is reduced (as expected from the distribution over the wavelengths of the imaginary part of the refractive index of liquid water). The spectrum of Figure 6.19a should be compared directly with the one of Figure 6.19b that is calculated for a ice cloud at different altitudes with $\tau = 50$. The main effect of the ice cloud is that the absorption is concentrated at $\lambda = 1500$ nm and notably the
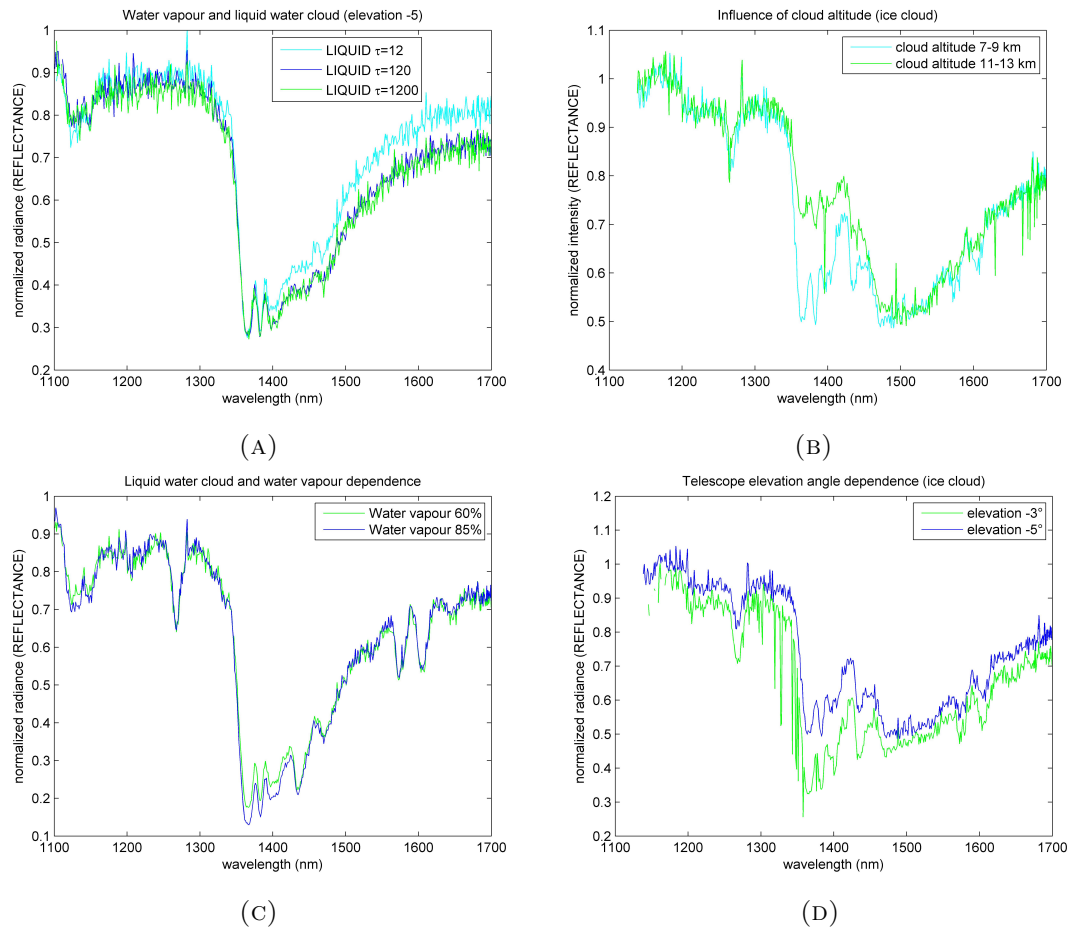
FIGURE 6.19: Normalized radiance (reflectance) simulation for an atmosphere composed of (A) only water vapour and liquid water cloud at 7-9 km with different τ (B) a ice cloud at different altitude with $\tau = 50$ (C) a liquid water cloud at 7-9 km with $\tau = 50$ and different water vapour concentrations (D) a ice cloud at 7-9 km with $\tau = 50$ with the measurements performed at two telescope elevation angles.

reflection peaks between 1400-1450 nm are really evident. These two reflection peaks are separated by the strong absorption band of CO_2 at around 1440 nm. It is worth noting that when the cloud is closer to the aircraft, less carbon dioxide is detected with the cloud having a screening effect. Then, in Figure 6.19c the influence of water vapour concentration is analyzed. It is seen that smaller water vapour mixing ratios lead to a less deep water vapour absorption band with no change in its shape as expected. The last plot shows the influence of the telescope elevation angle. For small angles, the light can travel longer in the atmosphere before hitting the cloud, thus more absorption from water vapour molecules is possible and consequently the reflection from the cloud top is weaker.

We consider very thick clouds ($\tau = 50$) in order to separate the contributions from liquid water and ice particles. Thus, the results should only be considered as qualitative. In real situations the clouds have lower optical thickness hence, making harder the distinction

of the phase of the particles forming the cloud. Nevertheless, this approach gives a good insight into the contribution of a cloud in the NIR spectrum and can be used to retrieve the thermodynamic phase of the constituent particles. In addition, the study should be considered as a sensitivity test to isolate the contribution of a cloud in the NIR spectra.
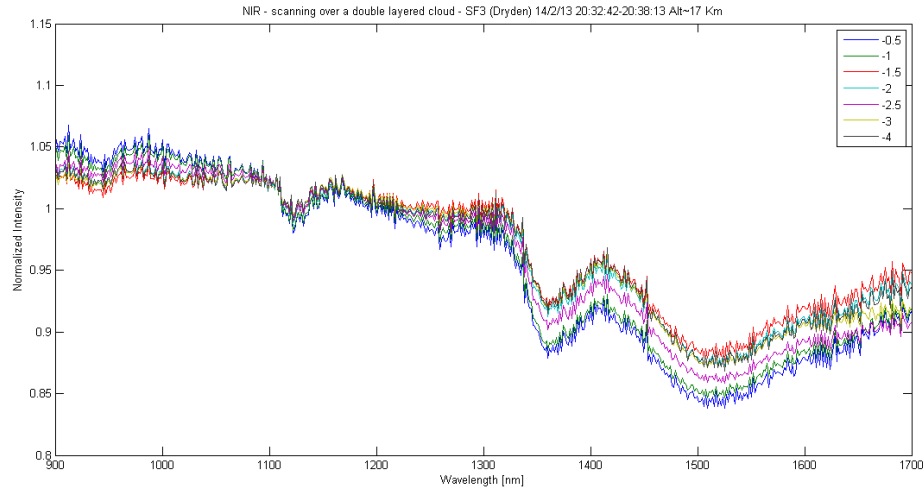
FIGURE 6.20: Measured NIR normalized intensity during SF3 at universal time 20:32:42 for different elevation angles when a first cirrus is located between 7-9 km and a second one between 11-13 km.

Further, we consider the influence of cirrus (ice clouds) on the NIR spectrum. As a case study we consider a small part of science flight 3 operated on the 14th of February 2013 from the Dryden Flight Research Center. For this flight at around universal time UT 20:30 a cirrus was present and the CPL recorded the depolarization map depicted in Figure 6.18. It is interesting that the depolarization is quite low (less than 0.4) after UT 20:30:00, indicating that the particles there are moderately non-spherical thus justifying again the use of the Mie code as a good approximation for slightly irregular spheres. Hence, it is possible to simulate the presence of a double layered cirrus with an optical thickness (or depth) between 1 and 3 as the one depicted in Figure 6.18. In order to compare directly to the measured spectrum of Figure 6.20, a simulation of a double layered cloud is shown in Figure 6.21. The agreement is good for a cloud with optical thickness $\tau = 1$ between 11 and 13 km and a lower cloud with $\tau = 3$ between 7 and 9 km as indicated by the CPL observation (Figure 6.18). The agreement is only qualitative due to differences in the longer wavelength part of the spectrum. However, from the comparison of Figure 6.20 and Figure 6.21 it is possible to conclude that the sampled double layered cirrus is completely made of ice particles (even the lower layer).

Further, in Figure 6.22 we analyze the effect on the NIR spectrum caused by a mixed phase cloud in the sense that the constituent particles are half made of ice and half made
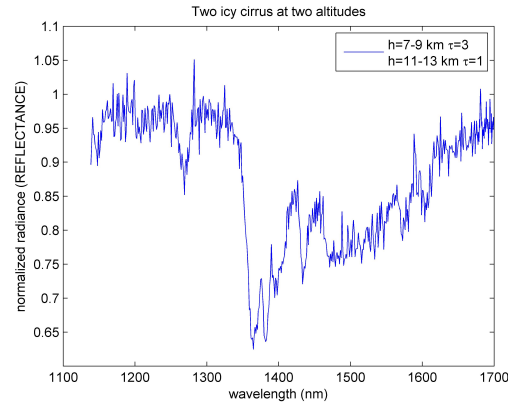
FIGURE 6.21: Normalized radiance (reflectance) simulation for an atmosphere with two different cirrus at two altitudes. The cirrus at 11-13 km has $\tau = 1$ and the cirrus at 7-9 km has $\tau = 3$. The smulation is done for an elevation angle of $-3°$.

of liquid water. The important part of the spectrum is, as before, the one between 1400-1500 nm. In the mixed phase cloud case, we see that the ice reflection peak splits in two halves due to carbon dioxide which is still detectable but, its absorption is reduced due to the absorption of light performed by the liquid particles at 1450 nm. In addition, the thermodynamic phase of the constituent cloud particles can be retrieved by examining the spectral structures in the 1400-1500 nm wavelength range and the slope of the normalized intensity at wavelengths larger than 1500 nm. This is summarized in Figure 6.22 where the three kinds of clouds are simulated with the same optical thickness i.e. $\tau = 50$. It is possible to appreciate that, depending on the type of the particles forming the clouds, different slopes of the spectra are present at wavelengths larger than 1500 nm. Then, in the case of an ice cloud also an intense reflectance peak comes in between 1400-1500 nm due to reflection from the cloud top.
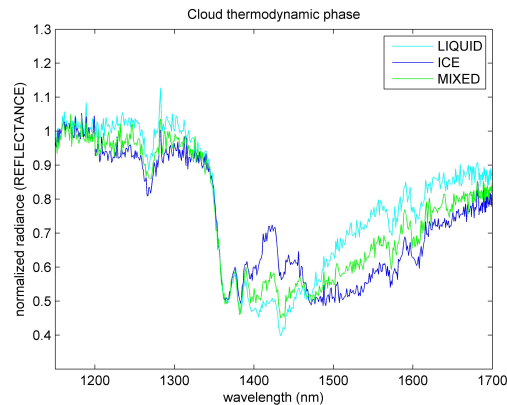
FIGURE 6.22: Normalized radiance (reflectance) simulation for an atmosphere with three different clouds with $\tau = 50$ at 7-9 km: an ice cloud, a mixed phase cloud and a liquid water cloud.
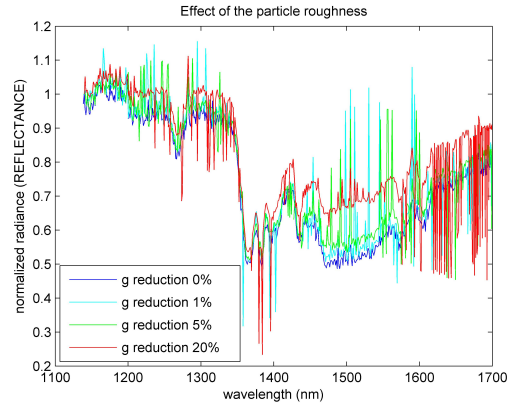
FIGURE 6.23: Normalized radiance (reflectance) simulation for an atmosphere with an ice cloud (at 7-9 km) composed of particles with different levels of roughness parametrized through a reduction of the asymmetry parameter g.

To conclude, in Figure 6.23 we propose the simulation of a cirrus composed of irregular spherical ice particles considering the results of the previous section. As investigated in the previous section, the effect on the optical properties of surface deformations and roughness is mainly visible on the asymmetry parameter g. The effect consists in a reduction of the value of g when irregularities are added to the surface of the scatterer. This behaviour is evident for small particles ($x < 10$) and very big ones ($x > 50$ [14]) while it is complex in the intermediate cases even if in most of these cases the value of g is unaltered by the presence of surface deformations. In particular, it is possible to distinguish small scale roughness (small reduction of g) from large scale deformations (larger reduction of g). In order to introduce that in the radiative transfer model we reduce the asymmetry parameter by some percentage with respect to the one given as output by the Mie code for smooth spheres. This g reduction is applied only for the relevant range of the size parameter mentioned above (when calculating the average of the asymmetry parameter over size). Thus, the effect of particle surface irregularities can be seen as a general increase of the reflected radiation over all the spectrum and it is more pronounced around 1500 nm where the ice absorption is located. The g reduction leads to more isotropic scattering events resulting in an attenuation of ice absorption. The effect is clearly recognizable even if the statistical error of the Monte Carlo sampling is larger for an atmosphere that scatters more light. For some wavelengths the radiance calculation fails causing large irregularities in the simulated spectrum. This problem can be solved increasing the number of photons at the price of a much longer computation time.

Chapter 7

Conclusions

We introduce a novel numerical model for electromagnetic scattering of single arbitrary shaped particles. The model is named the GDT-matrix (the Green's Dyadic technique for the Transition matrix) and evaluates the transition operator for the particle considered. This model is validated against the analytical Mie code for spheres, and against numerical exact technique as the DDA (through its implementation, i.e. the ADDA code) for non-spherical scatterers. First, the GDT-matrix model is contextualized as a DDA model solving the volume integral equation rewritten on the transition operator. Then, the strengths and weaknesses of the approach are described. Once assessed the limits concerning the calculation of the optical properties, we use the model to characterize ice particles as measured by the SID instrument for forward scattering. The GDT-matrix can predict the SID measurements for regular particles as well as for very irregularly shaped particles. In particular, generating the shapes of the scatterer with the Gaussian random sphere model and using these as input for the GDT-matrix code, it is possible to give an interpretation of the measured speckle patterns. The interference speckle are generated by deformed spheres and the degree of the deformations can be parametrized through the standard deviation of the deformations following a Gaussian distribution. In addition, the effect of the deformations is propagated to the optical properties, especially to the asymmetry parameter that is lowered. A clear decrease of the asymmetry parameter is observed in the simulations (for deformed ice particles with respect to the smooth ones) for small particles $x < 6$, while for bigger particles the accuracy of the GDT-matrix is not enough to evaluate the asymmetry parameter with a reasonably small error.

Further, we use these results in the context of multiple scattering i.e. considering the radiative effect of cirrus clouds on the NIR spectrum. In the last chapter, simulations of a high cirrus are displayed, demonstrating that the presence of the cloud can shield the

water vapour absorption leading to an increased reflected radiation (when the measurement is performed from an aircraft flying above the cloud with the telescope pointing down towards the cloud). Then, it is shown how the thermodynamic phase of the particles forming the cloud can be retrieved considering the entity of the reflected radiation. To conclude, deformed spherical scatterers are introduced in the main radiative transfer solver (effectively by reducing the asymmetry parameter), thus demonstrating the sensitivity of radiance measurements with respect to the quality of the surface of the single scatterer.

Future work is needed to increase the efficiency of the GDT-matrix code in order to reach a larger size parameter. This can be achieved for example, implementing an iterative solver to invert the many Green's function dyads. A Fast Fourier Transform can also be applied in order to speed up the many matrix multiplications. A final optimization can also be considered i.e. an implementation of the scheme on the GPU (graphics processing unit), thus parallelizing the algorithm.

Bibliography

[1] AJ Baran. From the single-scattering properties of ice crystals to climate prediction: A way forward. *Atmospheric Research*, 112:45–69, 2012. doi: 10.1016/j.atmosres. 2012.04.010.

[2] AO Langford et al. Retrieval of ice crystal effective diameters from ground-based near-infrared spectra of optically thin cirrus. *J. Geophys. Res.*, 110:D22201, 2005. doi: 10.1029/2005JD005761.

[3] P Foster et al. *Climate Change 2007: The Physical Science Basis. Contribution of Working Group I to the Fourth Assessment Report of the Intergovernmental Panel on Climate Change.* Cambridge University Press, Cambridge, 2007.

[4] Z Ulanowski, PH Kaye, E Hirst, RS Greenaway, RJ Cotton, E Hesse, and CT Collier. Incidence of rough and irregular atmospheric ice particles from small ice detector 3 measurements. *Atmospheric Chemistry and Physics*, 14:1649–1662, 2014. doi: 10.5194/acp-14-1649-2014.

[5] KN Liou. *An Introduction to Atmospheric Radiation.* Academic Press, San Diego, 2002.

[6] AJ Baran. A review of the light scattering properties of cirrus. *J Quant Spectrosc Radiat Transfer*, 110:1239–1260, 2009. doi: 10.1016/j.jqsrt.2009.02.026.

[7] S Fueglistaler, AE Dessler, TJ Dunkerton, I Folkins, Q Fu, and PW Mote. Tropical tropopause layer. *Rev. Geophys.*, 47:RG1004, 2009. doi: 10.1029/2008RG000267.

[8] EJ Jensen. Attrex (airborne tropical tropopause experiment) a venture class mission to understand the role of the tropical tropopause layer in earth's climate. *NASA Ames Research Center*, 2009.

[9] NASA. Espo database, 2015. URL https://espo.nasa.gov/.

[10] Z Ulanowski, E Hesse, PH Kaye, and AJ Baran. Light scattering by complex ice-analogue crystals. *J Quant Spectrosc Radiat Transfer*, 100:382–392, 2006. doi: 10.1016/j.jqsrt.2005.11.052.

[11] AJ Heymsfield et al. Observations and parameterizations of particle size distributions in deep tropical cirrus and stratiform precipitating clouds: Results from in situ observations in trmm field campaigns. *J. Atmos. Sci.*, 59:3457–3491, 2002. doi: 10.1175/1520-0469(2002)059⟨3457:OAPOPS⟩2.0.CO;2.

[12] E Hirst, RS Greenaway, P Field, and DW Johnson. Discrimination of micrometre-sized ice and super-cooled droplets in mixed-phase cloud. *Atmospheric Environment*, 35:33–47, 2001. doi: 10.1016/S1352-2310(00)00377-0.

[13] PH Kaye, E Hirst, RS Greenaway, Z Ulanowski, E Hesse, PJ DeMott, C Saunders, and P Connolly. Classifying atmospheric ice crystals by spatial light scattering. *Opt. Lett.*, 33:1545–1547, 2008. doi: 10.1364/OL.33.001545.

[14] P Yang, G Hong, GW Kattawar, and P Minnis. Uncertainties associated with the surface texture of ice particles in satellite-based retrieval of cirrus clouds: Part ii—effect of particle surface roughness on retrieved cloud optical thickness and effective particle size. *Geoscience and Remote Sensing, IEEE Transactions on*, 46: 1948–1957, 2001. doi: 10.1109/TGRS.2008.916472.

[15] BA Baum et al. Ice cloud single-scattering property models with the full phase matrix at wavelengths from 0.2 to 100 μm. *J Quant Spectrosc Radiat Transfer*, 146: 123–139, 2014. doi: 10.1016/j.jqsrt.2014.02.029.

[16] K Muinonen, T Nousianien, P Fast, K Lumme, and JI Peltoniemi. Light scattering by gaussian random particles: Ray optics approximation. *J Quant Spectrosc Radiat Transfer*, 55:577–601, 1996. doi: 10.1016/0022-4073(96)00003-9.

[17] T Nousianien, K Muinonen, and P Raeisaenen. Scattering of light by large saharan dust particles in a modified ray optics approximation. *Journal of Geophysical Research*, 108:4025, 2003. doi: 10.1029/2001JD001277.

[18] M Kahnert, T Nousianen, MA Thomas, and J Tyynelae. Light scattering by particles with small-scale surface roughness: Comparison of four classes of model geometries. *J Quant Spectrosc Radiat Transfer*, 113:2356–2367, 2012. doi: 10.1016/j.jqsrt.2012.03.017.

[19] E Hesse, CT Collier, A Penttilae, T Nousianen, Z Ulanowski, and PH Kaye. Modelling light scattering by absorbing smooth and slightly rough facetted particles. *J Quant Spectrosc Radiat Transfer*, 157:71–80, 2015. doi: 10.1016/j.jqsrt.2015.02.004.

[20] MI Mishchenko, LD Travis, and AA Lacis. *Scattering, absorption, and emission of light by small particles.* Cambridge University Press, Cambridge, 2004.

[21] EN Economou. *Green's Functions in Quantum Physics*. Springer-Verlag, Berlin, 1990.

[22] U Tricoli and K Pfeilsticker. Scattering of electromagnetic radiation based on numerical calculation of the t-matrix through its integral representation. *SPIE Proceedings*, 9232:923208, 2014. doi: 10.1117/12.2063545.

[23] C Bohren and D Huffman. *Absorption and Scattering of Light by Small Particles*. Wiley, New York, 1983.

[24] U Tricoli, P Vochezer, and K Pfeilsticker. Transition operator calculation with green's dyadic technique for electromagnetic scattering: A numerical approach using the dyson equation. *J Quant Spectrosc Radiat Transfer*, 2015. doi: 10.1016/j.jqsrt. 2015.04.006.

[25] E Akkermans and G Montambaux. *Mesoscopic Physics of Electrons and Photons*. EDP Sciences-CNRS, Paris, 2004.

[26] MI Mishchenko. Multiple scattering, radiative transfer, and weak localization in discrete random media: unified microphysical approach. *Rev Geophys*, 46, 2008. doi: 10.1029/2007RG000230.

[27] BT Draine and PJ Flatau. Discrete-dipole approximation for scattering calculations. *J. Opt. Soc. Am. A*, 11:1491–1499, 1994. doi: 10.1364/JOSAA.11.001491.

[28] MA Yurkin and AG Hoekstra. The discrete dipole approximation: An overview and recent developments. *J. Quant. Spectrosc. Radiat. Transfer*, 106:558–589, 2007. doi: 10.1016/j.jqsrt.2007.01.034.

[29] OJF Martin, C Girard, and A Dereux. Generalized field propagator for electromagnetic scattering and light confinement. *Phys. Rev. Lett.*, 74:526, 1995. doi: 10.1103/PhysRevLett.74.526.

[30] OJF Martin, A Dereux, and C Girard. Iterative scheme for computing exactly the total field propagating in dielectric structures of arbitrary shape. *J. Opt. Soc. Am. A*, 11:1073–1080, 1994. doi: 10.1364/JOSAA.11.001073.

[31] AD Yaghjian. Electric dyadic green's functions in the source region. *Proc. IEEE*, 68:248–263, 1980. doi: 10.1109/PROC.1980.11620.

[32] C Martinez-Ortiz. Matlab voxelizer, 2009. URL http://www.mathworks.com/matlabcentral/fileexchange/21044-3d-voxelizer.

[33] OJF Martin and NB Piller. Electromagnetic scattering in polarizable backgrounds. *Physical Review E*, 58:3909, 1998. doi: 10.1103/PhysRevE.58.3909.

[34] JI Peltoniemi. Variational volume integral equation method for electromagnetic scattering by irregular grains. *J. Quant. Spectrosc. Radiat. Transfer*, 55:637–647, 1996. doi: 10.1016/0022-4073(96)00007-6.

[35] PJ Flatau, GL Stephens, and BT Draine. Light scattering by rectangular solids in the discrete-dipole approximation: a new algorithm exploiting the block-toeplitz structure. *J. Opt. Soc. Am. A*, 7:593–600, 1990. doi: 10.1364/JOSAA.7.000593.

[36] RG Grainger, J Lucas, GE Thomas, and GBL Ewen. Calculation of mie derivatives. *Applied Optics*, 43:5386–93, 2004. doi: 10.1364/AO.43.005386.

[37] MA Yurkin and AG Hoekstra. User manual for the discrete dipole approximation code adda 1.1, 2012. URL http://a-dda.googlecode.com/svn/tags/rel_1.1/doc/manual.pdf.

[38] W Lou and TT Charalampopoulos. On the electromagnetic scattering and absorption of agglomerated small spherical particles. *J. Phys. D: Appl. Phys.*, 27: 2258–2270, 1994. doi: 10.1088/0022-3727/27/11/004.

[39] MK Singham, SB Singham, and GC Salzman. The scattering matrix for randomly oriented particles. *J. Chem. Phys.*, 85:3807–3815, 1986. doi: 10.1063/1.450901.

[40] WM McClain and WA Ghoul. Elastic light scattering by randomly oriented macromolecules: Computation of the complete set of observables. *J. Chem. Phys.*, 84: 6609–6622, 1986. doi: 10.1063/1.450714.

[41] VLY Loke, TA Nieminen, NR Heckenberg, and H Rubinsztein-Dunlop. T-matrix calculation via discrete dipole approximation, point matching and exploiting symmetry. *J. Quant. Spectrosc. Radiat. Transfer*, 110:1460–1471, 2009. doi: 10.1016/j.jqsrt.2009.01.013.

[42] G Mie. Beiträge zur optik trüber medien, speziell kolloidaler metallösungen. *Ann. Phys.*, 25:377–445, 1908. doi: 10.1002/andp.19083300302.

[43] WJ Wiscombe. Improved mie scattering algorithms. *Applied Optics*, 19:1505–1509, 1980. doi: 10.1364/AO.19.001505.

[44] T Deutschmann et al. The monte carlo atmospheric radiative transfer model mcartim: Introduction and validation of jacobians and 3d features. *J Quant Spectrosc Radiat Transfer*, 112:1119–1137, 2011. doi: 10.1016/j.jqsrt.2010.12.009.

[45] L Rothman, D Jacquemart, A Barbe, D Benner, M Birk, and L Brown et al. The hitran 2004 molecular spectroscopic database. *J Quant Spectrosc Radiat Transfer*, 96:139–204, 2005. doi: 10.1016/j.jqsrt.2004.10.008.

[46] RP Lawson, AV Korolev, SG Cober, T Huang, JW Strapp, and GA Isaac. Improved measurements of the drop size distribution of a freezing drizzle event. *Atmospheric Research*, 47-48:181–191, 1998. doi: 10.1016/S0169-8095(98)00062-3.

[47] O Möhler, S Büttner, C Linke, M Schnaiter, H Saathoff, O Stetzer, R Wagner, M Krämer, A Mangold, V Ebert, and U Schurath. Effect of sulfuric acid coating on heterogeneous ice nucleation by soot aerosol particles. *Journal of Geophysical Research: Atmospheres*, 110:2156–2202, 2005. doi: 10.1029/2004JD005169.

[48] E Hesse, A Macke, S Havemann, AJ Baran, Z Ulanowski, and PH Kaye. Modelling diffraction by facetted particles. *J Quant Spectrosc Radiat Transfer*, 113:342–347, 2012. doi: 10.1016/j.jqsrt.2011.11.017.

[49] B Werner at al. Measurements of o_3, no_2 and bro within the subtropical, and tropical upper troposphere and lowermost stratosphere from the global hawk during nasa attrex: Implications for ozone and total inorganic bromine. *(to be submitted)*, 2015.

[50] U Platt and J Stutz. *Differential Optical Absorption Spectroscopy.*

[51] NASA. Cloud physics lidar, 2015. URL http://cpl.gsfc.nasa.gov/.

[52] JR Raecke. Atmospheric spectroscopy of trace gases and water vapor in the tropical tropopause layer from the nasa global hawk. *Master thesis*, 2013.

[53] SG Warren. Optical constants of ice from the ultraviolet to the microwave. *Applied Optics*, 23:1206–1225, 1984. doi: 10.1364/AO.23.001206.

[54] LC Labonnote, G Brogniez, JC Buriez, M Doutriaux-Boucher, JF Gayet, and A Macke. Polarized light scattering by inhomogeneous hexagonal monocrystals: Validation with adeos-polder measurements. *J. Geophys. Res.*, 106:12139–12153, 2001. doi: 10.1029/2000JD900642.

[55] G Thuillier. The solar spectral irradiance from 200 to 2400 nm as measured by the solspec spectrometer from the atlas and eureca missions. *Solar Physics*, 214:1–22, 2003.

[56] P Schiebener, J Straub, JMHL Sengers, and JS Gallagher. Refractive index of water and steam as function of wavelength, temperature and density. *J. Phys. Chem. Ref. Data*, 19:677, 1990. doi: 10.1063/1.555859.

U. Tricoli and K. Pfeilsticker. Scattering of electromagnetic radiation based on numerical calculation of the T-matrix through its integral representation. SPIE proceedings, 9232, 923208, 2014. [22]

U. Tricoli, P. Vochezer and K. Pfeilsticker. Transition operator calculation with Green's dyadic technique for electromagnetic scattering: A numerical approach using the Dyson equation. J. Quant. Spectrosc. Radiat. Transfer, 2015. [24]

List of Figures

List of Tables

Acknowledgements